Theses and Dissertations

December 2012

DC and Microwave Analysis of Gallium Arsenide Field-Effect Transistor-Based Nucleic Acid Biosensors

John K. Kimani
University of Wisconsin-Milwaukee

DC and Microwave Analysis of Gallium Arsenide Field-Effect Transistor-Based Nucleic Acid Biosensors

by

John K. Kimani

A Dissertation Submitted in

Partial Fulfillment of the

Requirements for the Degree of

Doctor of Philosophy

in Engineering

at

The University of Wisconsin–Milwaukee

December 2012

Abstract

DC and Microwave Analysis of Gallium Arsenide
Field-Effect Transistor-Based Nucleic Acid Biosensors

by

John K. Kimani

The University of Wisconsin–Milwaukee, 2012
Under the Supervision of Professor David P. Klemer

Sensitive high-frequency microwave devices hold great promise for biosensor design. These devices include GaAs field effect transistors (FETs), which can serve as transducers for biochemical reactions, providing a platform for label-free biosensing. In this study, a two-dimensional numerical model of a GaAs FET-based nucleic acid biosensor is proposed and simulated. The electronic band structure, space charge density, and current-voltage relationships of the biosensor device are calculated. The intrinsic small signal parameters for the device are derived from simulated DC characteristics and used to predict AC behavior at high frequencies.

The biosensor model is based on GaAs field-effect device physics, semiconductor transport equations, and a DNA charge model. Immobilization of DNA molecules onto the GaAs sensor surface results in an increase in charge density at the gate region, resulting from negatively-charged DNA molecules. In modeling this charge effect on device electrical characteristics, we take into account the pre-existing surface charge, the orientation of DNA molecules on the sensor surface, and the distance of the negative molecular charges from the sensor surface. Hybridization with complementary molecules results in a further increase in charge density, which further impacts the electrical behavior of the device. This behavior is studied through simulation of the device current transport equations. In the simulations, numerical methods are used to calculate the band structure and self-consistent solutions

for the coupled Schrödinger, Poisson, and current equations. The results suggest that immobilization and hybridization of DNA biomolecules at the biosensor device can lead to measurable changes in electronic band structure and current-voltage relationships.

The high-frequency response of the biosensor device shows that GaAs FET devices can be fabricated as sensitive detectors of oligonucleotide binding, facilitating the development of inexpensive semiconductor-based molecular diagnostics suitable for rapid diagnosis of various disease states.

Table of Contents

LIST OF FIGURES

LIST OF TABLES

LIST OF SYMBOLS

L_{dna}	Length of DNA molecule in base pairs
L_g	Transistor gate length
W_g	Transistor gate width
A	Transistor device thickness
D_n	Diffusion constant
E	Electric field
E^{pk}	Peak velocity field
v	Electron drift velocity
v_s	Electron saturation velocity
$\epsilon_0 \epsilon$	Permittivity
C_{gs}	Gate-to-source capacitance
C_{gd}	Gate-to-drain capacitance
C_{ds}	Drain-to-source capacitance
g_{ds}	Output conductance
R_{ds}	Output resistance
R_C	Ohmic contact resistance
R_i	Charging resistance
S_{11}	Impedance reflection coefficient
g_m	Transconductance
f_T	Transition frequency
f_{max}	Maximum frequency of oscillation
I_{ch}	Channel current
I_{sat}	Saturation current
N_D	Doping density
L_D	Debye length
a	Lattice constant
μ	Low field mobility
Q_g	Electric charge under the gate
q	Electronic charge
τ	Switching time
τ_{dr}	Dielectric relaxation time
V_{bi}	Built-in voltage
V_{sbi}	Surface built-in voltage
V_D	Drain voltage
V_G	Gate voltage
V_S	Source voltage
V_{po}	Pinch-off voltage
n	Electron concentration
p	Hole concentration
n_i	Intrinsic carrier concentration
G_n	Carrier generation rate
R_n	Carrier recombination rate
m_e	Free electron mass

m^*	Effective mass
ρ	charge density
ϕ	Electrostatic potential
ϕ_s	Surface potential
ϕ_B	Barrier potential
ψ	Wave function
H	Hamiltonian of the Schrödinger equation
T	Lattice temperature
E_C	Conduction band energy
E_V	Valence band energy
E_g	Band gap energy
E_f	Fermi level energy
N_C	Conduction band density of states
N_V	Valence band density of states

ACKNOWLEDGEMENTS

Chapter 1

Introduction

Medical diagnostics have experienced tremendous advances over the last century and continue to enjoy state-of-the-art cutting edge technology today. To meet the need for diagnostics at the molecular level, FETs and semiconductor integrated circuit technology have provided a base to achieve miniaturized biosensor devices for *in vitro* and *in vivo* biomolecular sensing. A biosensor then, can be defined as an analytical device that uses an immobilized biospecific derived recognition system integrated within a transducer to detect and convert direct biochemical reactions into quantifiable energy signals. The energy signals may take the form of an electrical, optical, thermal, or magnetic response. The biochemical reactions detected by the biosensor include the action of enzymes, antibody, antigen, organelles, DNA, cells, tissue, or organic molecules.

The interaction of biological molecules results in changes to either chemical or physical properties. The parameters involved could include a change in mass, absorbance, heat, conductance or electron transfer. The transducing system converts this change into an appropriate signal and relays it for further processing. Figure 1.1 shows a generalized biosensor with a transducer that converts the biochemical reaction of analytes A and B into an electrical signal. The signal is then amplified and processed by appropriate data processing unit. In the biosensor, a sensing molecule B is a biologically sensitive material immobilized onto the transducer. A solution containing analyte A is then brought into the system for recognition.

Depending on the kind of chemical or physical change involved, and the transducer used, biosensors can be of various kinds. Examples of biosensors range from
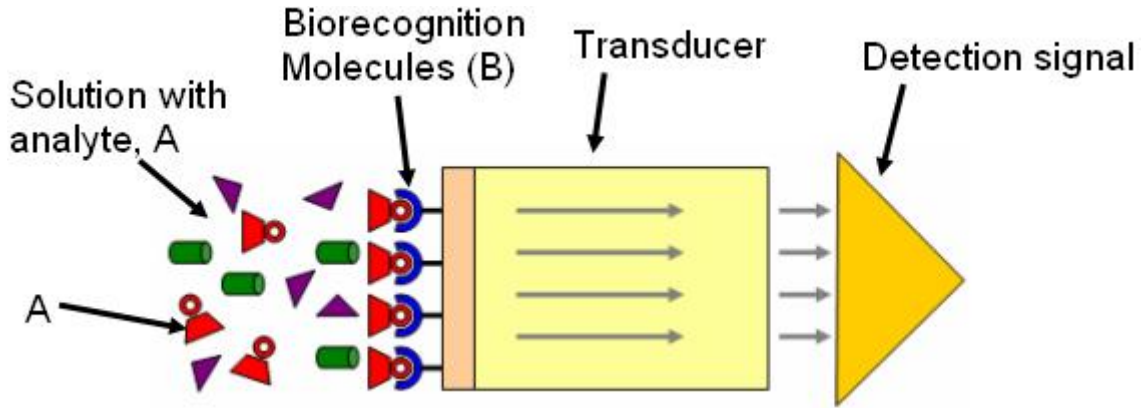
Figure 1.1: A general biosensor device.

optical biosensors such as those based on surface plasmon resonance [8, 9], electrochemical biosensors which are potentiometric or amperometric [10, 11], quartz crystal microbalance sensors based on the piezoelectric effect [12, 13], and cantilever based biosensors [14–16]. All of these biosensors have been widely used to detect the presence of specific substances and biomolecules in sample solutions including oxygen [17, 18], pH variations [19, 20], enzymes [21, 22], proteins [23, 24], and nucleic acids [25–27].

Devices operating on a biosensor's basic principles were first observed in the 1920s [28, 29]. In the 1950s, L. C. Clark described the first biosensor and its principles of operation in a paper he published in the ASAIO journal, in which he described the operation of an electrode to detect oxygen tensions in blood and tissue [17]. Clark, henceforth referred to as the father of biosensors, published a more definitive paper in 1962 which outlined the principles of operation of the first glucose biosensor. This sensor introduced enzyme transducers based on the enzyme glucose oxidase. The device revealed that oxygen and glucose concentrations were proportional. This transducer served as a platform for electrochemical sensors [21]. Following Clark's research, Updike and Hicks [30] built a functionalized enzyme electrode for measuring glucose, and Guibault and Montalvo developed the first urea sensor based on a potentiometric approach using the enzyme urease immobilized

on an ammonia electrode [31]. The first ion-selective field effect transitor (ISFET) was introduced in 1970 by Bergveld [32]. In 1975, Lubbers, et al., developed the first fiber-optic biosensor that measured O_2 or CO_2 [33], and a fiber optic glucose biosensor based on surface plasmon resonance appeared in 1980. The first DNA biosensor based on a quartz crystal microbalance (QCM) was described by Fawcett et al., in 1988 [34].

Commercialization of biosensor technology began in 1975 when the Ohio-based Yellow Springs Instrument Company marketed its glucose analyzer [35]. In 1992, the first hand-held biosensor was released by i-SAT [36]. The great promise held by these biosensors led to numerous research projects on diverse biosensors beginning in the 1980s and 1990s [37–39].

The merger between the biochemically selective recognition and solid state integration circuits has resulted in the miniaturization of biosensor devices, making it possible to obtain results using only a small sample of specimen. This miniaturization is possible because of the micro level fabrication technology employed in the semiconductor industry [16, 40, 41]. Micro level fabrication enables multisensor realization on a single chip where different substances can be detected simultaneously. The ease of fabricating many devices on one chip makes cost effective large scale production possible. Due to the minute size of the sensors, implantation has also become possible, enabling *in vivo* measurements. Reliable bio/chemical FETs have been applied effectively in various arenas including medical diagnostics [42, 43], environmental monitoring [44, 45], and food quality control [46, 47].

Field-effect transistors have played an essential role in pH and molecular detections, forming a novel platform for biosensor devices. The operation of these biosensors work on the same principles used in MOSFET devices: they have an active channel through which electrons or holes travel from source to drain (or vice versa in the case of holes). The channel however, is modulated by a potential applied

to an isolated gate metal electrode. For MESFETs, the gate metal is effectively replaced by a biorecognition molecule immobilized on the device. Interaction of the target biomolecules in solution with the immobilized biorecognition molecule leads to electron or charge transfer and the creation of a potential difference which modulates the conducting channel within the semiconductor. Other label-free field-effect transistors such as those based on silicon have been used in DNA sensing [48–50]. Microchips and silicon nanowires have been favored because of their miniaturization and sensitivity [16,41,51,52], but the fabrication of nanowires makes this technology unsuitable for mass production. Surface plasmon resonance (SPR) DNA sensors have also been proposed for their high sensitivity [53–55]. SPR sensors however, require complex equipment setup [56,57], are affected by optical interference fringes [55], and require modified probes. Their sensitivity also decreases with short DNA sequences and small packing density [58]. The performance of these devices depends on various parameters including the selectivity of the bioreceptor, magnitude of charge transfer, sensitivity of the transducer and more. This dissertation focuses on DNA-based biosensors fabricated on GaAs FETs. GaAs transistors offer a platform with great promise especially when the need exists for faster, smaller, and cheaper sensing devices for molecular diagnostics. The technology provides label-free devices which are easy to use and minimize any modifications of biomolecules that could result in the long detection times and complicated protocols required by traditional methods.

In this research, GaAs field-effect devices are simulated and analyzed as platforms for DNA biosensors. The DC characteristics are established for the GaAs device incorporating a DNA charge model for single strands immobilized on the gate region, and after hybridization by complimentary target strands. The potential for microwave frequency applications is also discussed with the extraction of small signal parameters. This study is also motivated by the fact that DNA hybridiza-

tion leads to rapid diagnosis of infectious diseases using short DNA sequences which serve as genetic markers for these diseases. Biomolecular binding activity can be directly transduced into an electrical signal using microwave field-effect devices that have high speed and sensitivity with readily available and mature semiconductor fabrication techniques.

Chapter 2 summarizes GaAs characteristics together with field-effect devices that form the biosensor platform. Device operation and important electrical parameters are also discussed. The detection of DNA biomolecules involves the understanding of the DNA structure, immobilization onto the GaAs surface, hybridization, and charge transfer model studied in Chapter 3. Chapter 4 deals extensively with the field-effect device physical model which details the theory behind the charge carriers and current equations. Chapter 5 explains the numerical methods used to calculate the band structure and the self-consistent solutions for the coupled Schrödinger, Poisson, and current equations in the simulations. The simulations and results, which include the device setup, calculations, and device modeling are discussed in Chapter 6, and conclusions presented in Chapter 7.

Chapter 2

GaAs Characteristics and Devices

Gallium arsenide is a "III-V" compound semiconductor composed of the elements gallium in group III and arsenic in group V of the periodic table. Created and reported by Goldschmidt in 1929 [59], the electronic properties of GaAs and other III-V compounds as semiconductors were reported 1952 when the first published article on the subject appeared [1]. The two elements form a crystal lattice that gives the compound semiconductor properties similar to those in group IV, such as silicon and germanium. GaAs is based on crystalline material having two sublattices, gallium and arsenic; each face centered cubic (fcc) structure. The two sublattices are offset by half the diagonal of the fcc cube from each other. Figure 2.1 shows the unit cube crystal structure of GaAs.
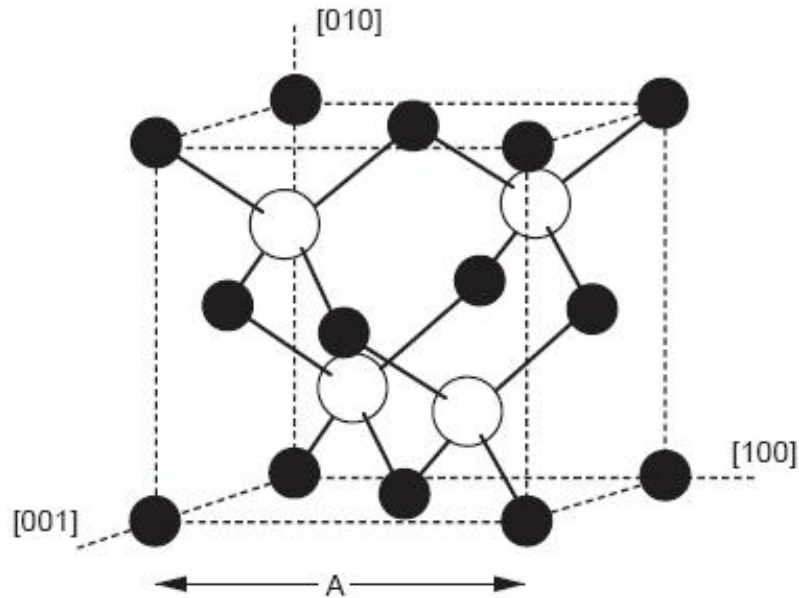
Figure 2.1: GaAs crystal structure.

Each Ga atom in the lattice is surrounded by four equidistant As atoms and vice

versa, forming a crystal structure configuration called a cubic zincblende. The bond between each pair of nearest neighbors is formed by electrons with opposite spin. The band structure of semiconductors is dictated by the laws of quantum mechanics. In particular, electrons in isolated atoms can only exist at specific energy levels. Therefore, these atoms possess specific energy values. The bands of interest where these electrons can be found in semiconductor materials are termed conduction and valence bands, having energies E_c and E_v respectively. Between these bands exists a forbidden region with non-existent states called the band gap, E_g, an important parameter in the material properties of semiconductors. At room temperature and normal atmospheric conditions, GaAs has an energy band gap value of 1.42eV compared to the silicon value of 1.2eV. GaAs is also a *direct band gap* material since the minimum of the conduction band is directly above the maximum of the valence band. GaAs electron mobility at 300 K ($\approx$8500 cm^2/V-s) is about six times that of Si ($\approx$1400cm^2/V-s) with a higher drift velocity desired for optimum device performance. The carrier velocity is impacted by electric field which subjects it to an accelerating force ($F = -qE$). Carrier velocity is also affected by opposition forces from electron scattering and collisions with the crystal lattice. At low field strengths, the velocity is defined as the drift velocity, v, and is linearly related to the electric field strength through a constant of proportionality μ, expressed as

$$v = \mu E \tag{2.1}$$

where the electron velocity v is in cm/s, E is the electric field strength (V/cm) and μ (in cm^2/V-s) depends on the mean free time between collisions (τ_c) and the electron effective mass (m^*). This can be expressed as

$$\mu = -\frac{q\tau_c}{m^*} \tag{2.2}$$

with the velocity v in (2.1) written as

$$v = -\frac{q\tau_c}{m^*}E \tag{2.3}$$

This relationship is graphed in Figure 2.2 for GaAs and silicon. Although the
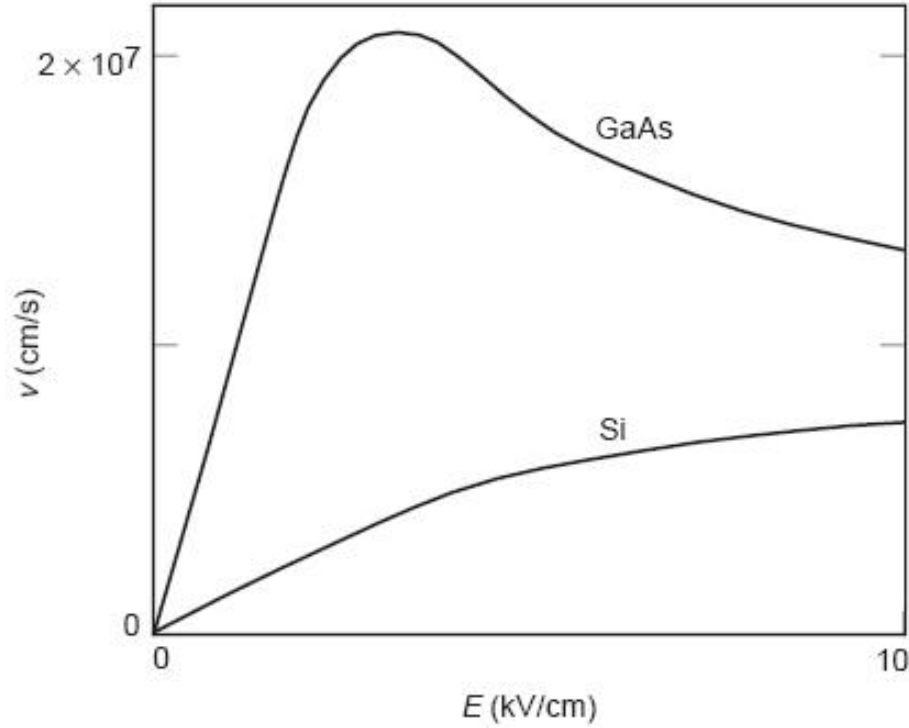
Figure 2.2: Drift velocity-electric field characteristics of GaAs and Si [1].

peak mobility of GaAs at the linear region can be up to six times greater than that of silicon, the maximum drift velocity is always at least two times that of Si. Mobility is a function of temperature and impurity concentration, and at equilibrium conditions, the saturation, or peak, velocity of GaAs is about 2.1 x 10^7 cm/s [1]. Appendix B lists important GaAs properties and material characteristics, and a complete physical model of GaAs and field-effect devices used in this research are discussed in detail in Chapter 4.

The superior transport properties of GaAs over those of silicon make it desirable for use at microwave frequencies. Another major advantage of GaAs in microwave

applications is the higher resistivity substrates available with GaAs. Whereas un-doped Si materials have resistivities of approximately 100 Ω-cm, GaAs materials can be made with resistivities greater than 10^8 Ω-cm, providing a better semi-insulating substrate in which device isolation can be easily achieved for GaAs FET applications.

2.1 The Shockley FET Model

The main concept of the field effect transistor dates back to the 1930s when two patents were filed on methods for controlling an electric current [28,29]. However, it wasn't until the 1950s when Stuetzer in 1950 [60], and Shockley in 1952 [61] analyzed and described the modern FET device. Since their actual demonstration in the late 1960s and early 1970s [62–64], they have played an important part in microwave industry in the design of amplifiers, mixers, oscillators, switches, attenuators, modulators, and high speed integrated circuits [40].

Figure 2.3 shows a simple GaAs MESFET cross-section whose main features are the metal-semiconductor junctions. In the device, an n-doped (around 10^{17} cm^{-3}) GaAs region forms an active channel and is grown epitaxially on a low-conductivity semi-insulating substrate. Source and drain contacts (comprised of Au/Ge alloys) form ohmic contacts on the active channel, while the gate is a Schottky barrier. Popular gate contacts are Al, Ti-Pt-Au layered structure, and Pt. The gate also can be formed by a p^+ region. A gate potential (also called gate bias) modulates
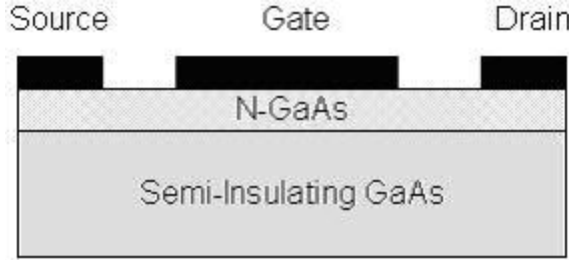
Figure 2.3: Simple cross-section of a GaAs MESFET.

the width of the depletion region under the gate, varying the cross section area of the active channel. In this way, the source-drain current I_{DS} can be controlled. As the gate bias increases, the drain region of the channel becomes increasingly reverse-biased, finally saturating and limiting further carrier flow. At this point the channel is referred to as being "pinched off", and current in the channel remains unchanged. In modern devices, the conducting channel has sub-micron nominal printed gates that can control the flow of current in the channel, making the device behave as a high speed voltage controlled switch.

Figure 2.4 shows a schematic of the Shockley model of a MESFET proposed by William Shockley [61]. This model uses a gradual channel approximation which assumes that the channel dimensions are a gradually varying function of position. The region under the gate is totally depleted with a sharp boundary between this region and the neutral undepleted channel. At each point, the depletion width $A_d(x)$
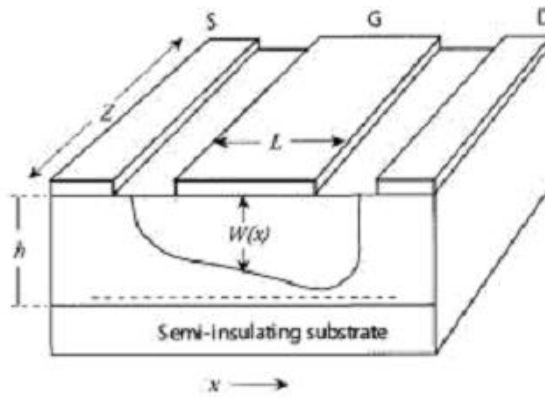
Figure 2.4: MESFET showing the depletion region and the channel for current flow (dotted line).

under the gate is a solution of the Poisson equation for a one dimensional junction and is a factor of the built-in voltage V_{bi}, the gate voltage V_{GS}, and the channel voltage $V(x)$, given by

$$A_d(x) = \left[\frac{2\epsilon_r \epsilon_0}{q N_d} \left(V(x) + V_{bi} - V_{GS} \right) \right]^{\frac{1}{2}},$$

(2.4)

which leads to the incremental change of the channel potential, dV

$$dV = I_{ch}dR = \frac{I_{ch}dx}{qN_d\mu_nW[A - A_d(x)]}, \tag{2.5}$$

where I_{ch} is the channel current, qN_d is the charge density, μ_n is the electron mobility, and $W[A - A_d(x)]$ is the channel area. The current equation I_{ch} can thus be obtained by substituting equation (2.4) into (2.5) and integrating from $x = 0$ to L giving

$$I_{ch} = I_D = g_0\left[V_{DS} - \frac{2}{3}\frac{\left[(V_{DS} + V_{bi} - V_{GS})^{\frac{3}{2}} - (V_{bi} - V_{GS})^{\frac{3}{2}}\right]}{V_{po}^{\frac{1}{2}}}\right] \tag{2.6}$$

for MESFET linear operation where the drain voltage V_{DS} is less than the saturation drain voltage $V_{D(sat)}$, $(V_{DS} < V_{D(sat)})$. The dashed line is the current path in the undepleted region on Figure 2.4. Here, V_{po} is the pinched-off voltage at the onset of saturation, defined by

$$V_{po} = \frac{qN_dA^2}{2\epsilon}, \tag{2.7}$$

where A is the thickness of the active layer, $\epsilon = \epsilon_r\epsilon_0$ is the permittivity of GaAs, and g_0 is the channel conductance when the channel is fully open $(A_d(x) = 0)$, given by

$$g_0 = \frac{q\mu_nN_dWA}{L}, \tag{2.8}$$

where W is the gate width and L is the gate length.

At saturation, $(V_{DS} > V_{DS}(sat))$ where

$$V_{DS}(sat) = V_{po} - V_{bi} + V_{GS}, \tag{2.9}$$

the drain current becomes saturated and remains unchanged with further changes

in V_{DS}. This current is given by

$$I_D(sat) = g_0 \left[\frac{V_{po}}{3} + \frac{2\left(V_{bi} - V_{GS}\right)^{\frac{3}{2}}}{3V_{po}^{\frac{1}{2}}} - V_{bi} + V_{GS} \right]. \tag{2.10}$$

Typical current-voltage characteristics curves for the active and saturation regions at different gate voltages for the Shockley model are shown in Figure 2.5. Similar current-voltage relationships have also been obtained in models described by Curtice [65, 66], Statz et al. [67], and Chang et al. [68].
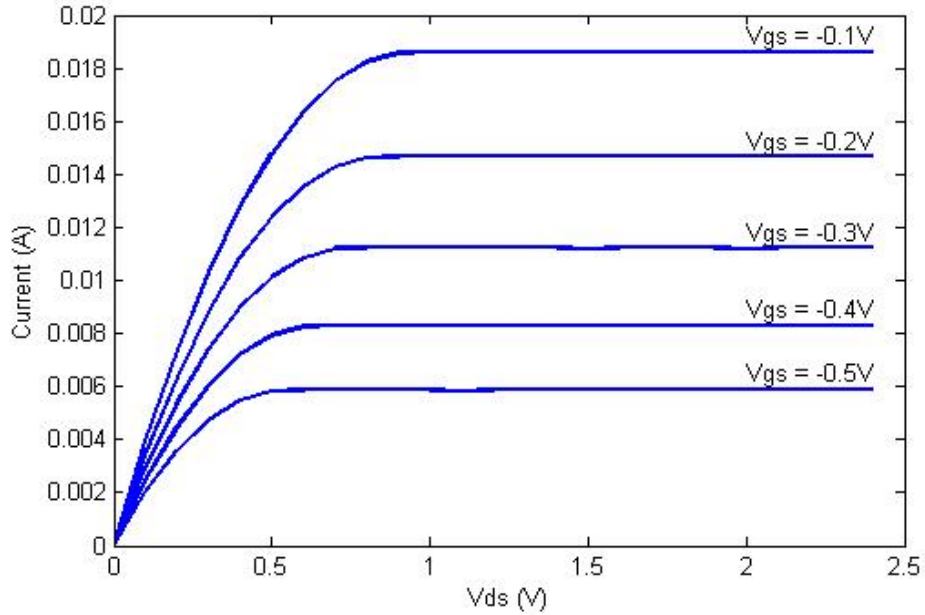
Figure 2.5: Current voltage characteristics of a MESFET.

2.2   Small Signal Equivalent Circuit

Equivalent circuits for the MESFET can be modeled as either small signal or large signal models. Large signal models can be described by increased changes in terminal voltages that result in a nonlinear response of the drain-source current characteristics. Information from multiple bias points is thus extracted and circuit elements like capacitances, inductances, and resistances are described by empirical or phys-

ical expressions that are functions of device and terminal voltages. In small signal equivalent models, however, small gate-to-source voltages produce linear changes in drain-source currents. This model is expressed by a simple lumped-element circuit; at a given bias point in the saturation region the circuit elements can be determined by either DC current-voltage characteristics or scattering parameters (s-parameters) over a certain frequency range. In this work, we consider only the small signal model since it is sufficient to model the FET device where the applied signal is much smaller than the bias voltage.

Small signal equivalent circuit models have been determined [2, 69–73], and one commonly-used model is shown in Figure 2.6. The model shown is for an extrinsic device operating in common-source configuration in the saturation region. This
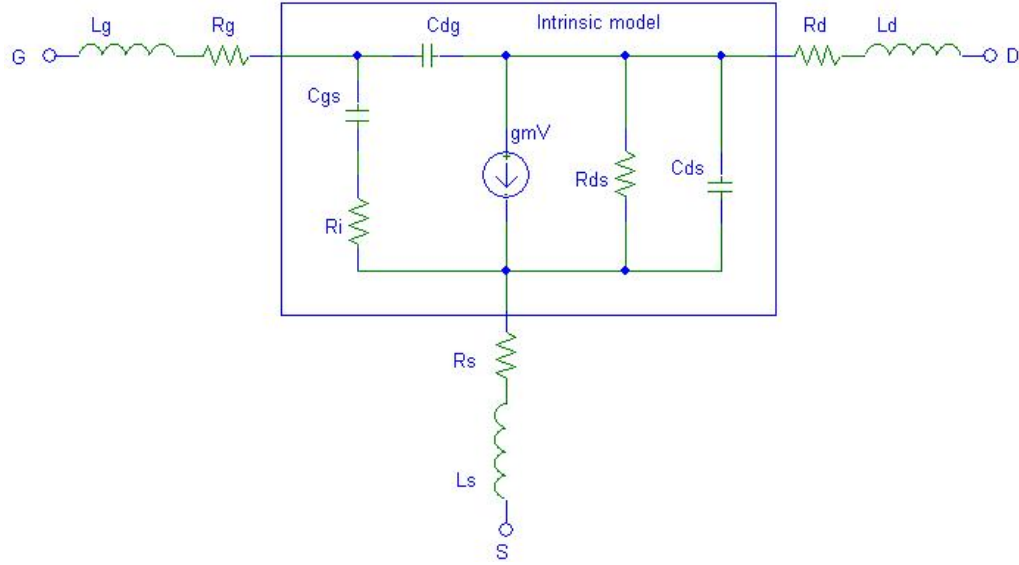
Figure 2.6: Basic equivalent circuit for GaAs MESFET.

extrinsic model includes the intrinsic device, shown in the box and in Figure 2.7, together with the extrinsic (parasitic) elements. In the intrinsic FET model, C_{gs} and C_{gd} represent the geometric capacitances due to the space charge region between the gate and source electrodes, and between the gate and drain electrodes respectively. C_{ds} models the substrate capacitance between the drain and the source, g_m is the frequency-independent transconductance, R_{ds} is the output resistance, and R_i is a
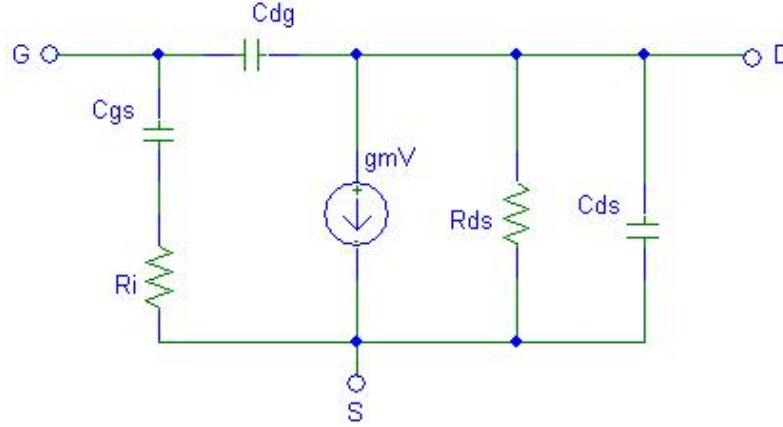
Figure 2.7: Intrinsic equivalent circuit for GaAs MESFET.

charging resitance for the distributed nature of RC networks. Other small signal figures of merit include the delay time, τ, which is the response time of the drain to changes in charge at the gate, the transition frequency f_t at which the current gain is unity, and the maximum frequency of operation f_{max}. The extrinsic elements include the source, drain, and gate-metal resistance R_s, R_d, and R_g that are associated with device contacts, on the order of 1Ω for microwave FETs [74]. Parasitic inductances represented by L_g, L_s, and L_d also arise from metal contacts with the device surface, with values typically ranging from $5-10$pH for L_g and L_d, and 1pH for the L_s [74].

The physical origin of these components is shown in Figure 2.8 where the equivalent circuit is superimposed on a MESFET cross-section. The figure shows both the parameters responsible for the active characteristics as well as some parasitic elements. These circuit elements are derived from small-signal s-parameter measurements or from DC characteristics as described next.

2.2.1 Transconductance, g_m

The MESFET can be modeled as a voltage-controlled current source, since the drain current can be altered by small variations of the gate electrode potential. The transconductance that defines the intrinsic small signal current gain is obtained
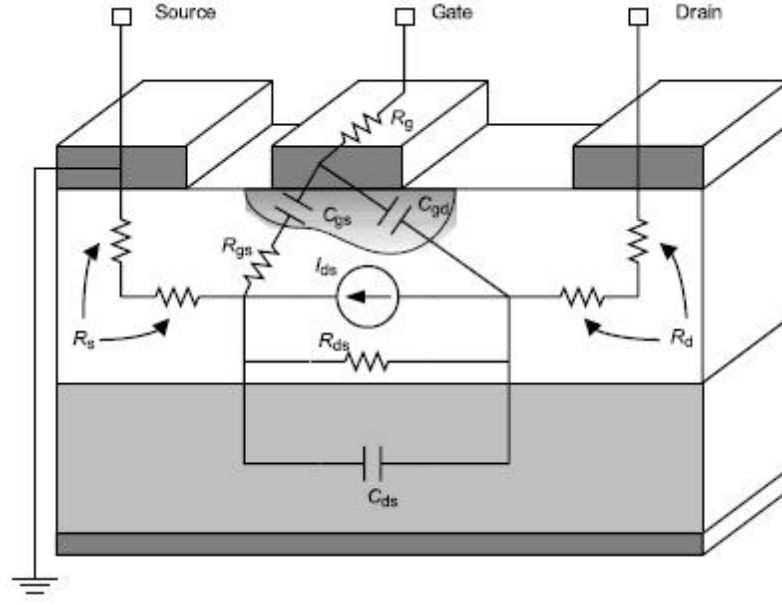
Figure 2.8: Physical origins of the equivalent circuit components of a MESFET [2].

from the differentiation of the drain current expression with respect to gate-source voltage with constant drain-source voltage. That is

$$g_m = \frac{\partial I_D}{\partial V_{GS}}|_{V_{DS}=constant} \tag{2.11}$$

which for the Shockley model evaluates to

$$g_m = g_0 \frac{(V_{DS} + V_{bi} - V_{GS})^{\frac{1}{2}} - (V_{bi} - V_{GS})^{\frac{1}{2}}}{V_{po}^{\frac{1}{2}}} \tag{2.12}$$

for the linear region and

$$g_m(sat) = g_0 \left[1 - \left(\frac{V_{bi} - V_{GS}}{V_{po}} \right)^{\frac{1}{2}} \right] \tag{2.13}$$

for the saturation region.

2.2.2 Output Resistance, R_{ds}

Output resistance is the channel resistance that is often given by its inverse, the output conductance, g_{ds}. This conductance is derived from the change in drain current expression with respect to drain-to-source voltage, determined by

$$g_{ds} = \frac{1}{R_{ds}} = \frac{\partial I_D}{\partial V_{DS}}. \tag{2.14}$$

The output resistance is low at low bias levels and increases as the device reaches saturation.

2.2.3 Gate-to-Source Capacitance, C_{gs}

The gate-to-source capacitance, C_{gs}, for a given constant drain potential represents the rate of change of free charge on the gate electrode as a function of small variations in gate bias voltage, given by

$$C_{gs} = \frac{\partial Q_g}{\partial V_{GS}}\big|_{V_{GD}=constant}, \tag{2.15}$$

where Q_g is the gate charge determined by integrating the normal component under the gate over the gate area, using the Poisson equation. Knowledge of this capacitance is useful for input impedance and high frequency performance and typically on the order of 1pF/mm gate width.

2.2.4 Gate-to-Drain Capacitance, C_{gd}

The gate-to-drain capacitance, C_{gd}, is found from the derivative of the depletion charge below the gate as a function of gate-drain voltage at a constant gate-to-

source voltage as follows,

$$C_{gd} = \frac{\partial Q_g}{\partial V_{GD}}\Big|_{V_{GS}=constant}. \tag{2.16}$$

C_{gd} is typically in the order of 1pF/mm gate width and smaller values are essential for greater reverse isolation of the device at high frequencies.

2.2.5   Drain-to-Source Capacitance, C_{ds}

C_{ds} is the substrate capacitance that accounts for geometric capacitance effects between the source and drain electrodes and given by

$$C_{ds} = \frac{\partial Q_g}{\partial V_{DS}}\Big|_{V_{GS}=constant} \tag{2.17}$$

This capacitance is typically considered parasitic and is an order of magnitude less than C_{gs}, and C_{gd}.

2.2.6   Transition Frequency, f_T

For use in microwave applications, important transistor figures of merit are the gain bandwidth product f_T, and the maximum frequency of oscillation, f_{max}. For short gate lengths, f_T is related to the transit time of electrons across the channel and is given by

$$f_T = \frac{g_m}{2\pi(C_{gs} + C_{gd})}. \tag{2.18}$$

The parameter f_{max}, is also defined as the frequency which the unilateral power gain reduces to one. It is given approximately by

$$f_{max} = \frac{f_T}{2}\sqrt{\frac{R_{ds}}{R_g}}, \tag{2.19}$$

where R_g is the gate resistance. This is the maximum frequency at which power can be extracted from the device, and for high frequency performance, short gate length and high semiconductor carrier velocities are essential. This also reduces the transit time τ required for carriers to travel from the source to the drain, given by

$$\tau = \frac{L}{\mu E_x} \approx \frac{L^2}{\mu V_D} \tag{2.20}$$

for low fields and

$$\tau = L/v_s \tag{2.21}$$

for high fields. The saturation velocity is denoted as v_s.

2.2.7 Charging Resistance, R_i

This resistor accommodates gate charging current paths and models finite charging times proportional to the carrier transit delay with a constant $K = 0.1747$ [75], given by

$$R_i = \frac{K\tau}{C_{gs}}. \tag{2.22}$$

For the overall equivalent circuit shown in Figure 2.7, the parameter values have been determined for various device geometries [74–81] and Table 2.1 shows some typical circuit values for a small-signal GaA MESFET with a gate length in the range 0.25μm to 1μm.

R_{ds}: 250 - 500Ω	C_{gs}: 0.15 - 0.4 pF
R_i: 1.0 - 10Ω	C_{gd}: 0.01 - 0.03 pF
R_g: 0.5 - 3Ω	C_{ds}: 0.05 - 0.1 pF
R_s: 1.0 - 5Ω	g_m: 20 - 40 mS
R_d: 1.0 - 5Ω	τ: 0 - 5 ps

Table 2.1: Typical equivalent circuit values for a small-signal GaAs FET.

2.3   The Ungated GaAs FET

The structure of an ungated GaAs FET can be compared with that of a MESFET with a missing gate Schottky contact, leaving a free GaAs surface between the source and the drain ohmic contacts. This surface has a pinned Fermi level by a high density of surface states, leaving a depletion layer whose shape and thickness determine the low field resistance and the saturation current. The effect of the surface states is described in section 4.4.3. Provided that the source-to-gate separation region is higher than the depletion depth, the ungated FET acts as a saturated resistor with an electric field almost perpendicular to the surface. The channel (and hence the resistivity of this device) is modulated by both the channel and the surface potentials.

Figure 2.9 shows a schematic of an ungated FET. Baek et. al. [5] used this simple model to deduce the electron saturation velocity, v_s, and the surface built-in voltage V_{sbi} as factors of device length and measured current-voltage characteristics. For a
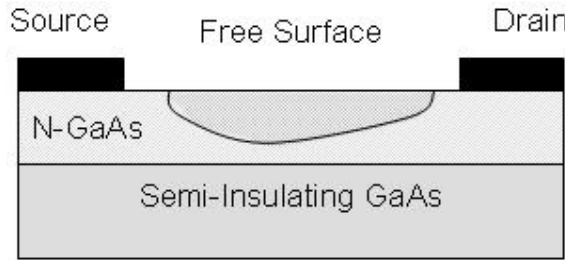
Figure 2.9: Simple Cross-section of an ungated GaAs FET.

uniform doping profile with an applied drain voltage, the surface depletion depth is a factor of the uniform doping density, N_d, the surface built-in voltage, V_{sbi}, the channel potential $V(x)$, and the surface potential, $\phi_s(x)$, given by

$$\frac{qN_d}{2\epsilon}h^2(x) = V_{sbi} + V(x) - \phi_s(x). \tag{2.23}$$

The surface potential, $\phi_s(x)$, varies linearly along the surface according to

$$\phi_s(x) = \frac{V_D}{L}x, \tag{2.24}$$

where V_D is the applied drain voltage and L is the contacts separation distance. The current-voltage characteristics of this device can be modeled as a two-piece lineal approximation where we first consider the low electric field (electron velocity $<$ saturation velocity) with a constant electron mobility, followed by the onset of saturation, illustrated in Figure 2.10.
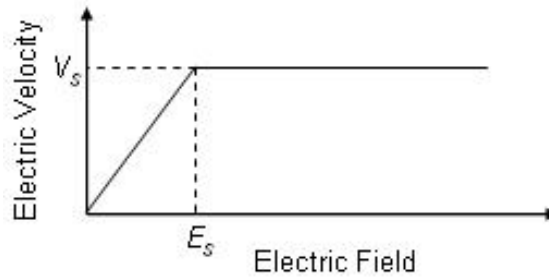
Figure 2.10: Two-piece linear approximation for electron velocity.

As the drain-source potential is increased, a current flows and the current-voltage behavior for the region below saturation velocity is linear, directly following the velocity-field characteristics of the GaAs semiconductor. The channel current, I_D, in this region is given by

$$I_D = qN_d\mu_n W[A - h(x)]\frac{\partial V(x)}{\partial x}, \tag{2.25}$$

where qN_d is the charge density, μ_n is the low field mobility, $W[A - h(x)]$ is the channel area, and $\frac{\partial V(x)}{\partial x}$ is the electric field. Integrating equation (2.25) from $x = 0$ to L with the boundary conditions for $V(x)$ expressed as

$$V(0) = R_c I_D$$

$$V(L) = V_D - R_c I_D \tag{2.26}$$

leads to an expression for I_D defined as

$$G = \frac{1}{2} \left[h^2(0) - h^2(L) \right] - d\left[h(0) - h(L) \right] + d(d - A) \ln \left(\frac{h(0) + d - A}{h(L) + d - A} \right) \tag{2.27}$$

where

$$G = \frac{\epsilon V_D}{q N_d} \tag{2.28}$$

$$h(0) = \left[\frac{2\epsilon}{q N_d} (V_{sbi} + R_c I_D) \right]^{\frac{1}{2}} \tag{2.29}$$

$$h(L) = \left[\frac{2\epsilon}{q N_d} (V_{sbi} - R_c I_D) \right]^{\frac{1}{2}} \tag{2.30}$$

and

$$d = \frac{L I_D}{W q \mu_n N_d V_D}. \tag{2.31}$$

Here, R_c is the ohmic contact resistance under the source and drain contacts and ϵ is the dielectric permittivity. For GaAs $\epsilon = \epsilon_r \epsilon_0 \approx 1.14 \text{x} 10^{-10} F/m$ [6]. In cases where $R_c \to 0$, the depletion layer becomes uniform with current, I_D given by

$$I_D = W q \mu_n N_d \frac{V_D}{L} A \left[1 - \left(\frac{V_{sbi}}{V_{po}} \right)^{\frac{1}{2}} \right], \tag{2.32}$$

where V_{po} is defined in equation (2.7). Hence the resistance of the channel can be approximated as

$$R = R_{ch} = \frac{L}{W q \mu_n N_d A \left[1 - \left(\frac{V_{sbi}}{V_{po}} \right)^{\frac{1}{2}} \right]}. \tag{2.33}$$

For electron velocities below the saturation velocity (where the electric field is below the saturation electric field E_s in Figure 2.10), the device behaves as a resistor with the slope of the $I_D - V_D$ characteristic curve defining the sum of the channel and contact resistances. The saturation current, I_{Dsat}, in the saturation region can be

expressed as

$$I_{Dsat} = WqN_d \left[A - \left\{ \frac{2\epsilon}{qN_d}(V_{sbi} + R_c I_{Dsat}) \right\}^{\frac{1}{2}} \right] v_s, \tag{2.34}$$

where v_s is the electron saturation velocity. This equation can be solved for I_{Dsat} obtaining

$$I_{Dsat} = WAqN_d v_s \left[1 + \frac{\chi}{2} - \left(\frac{\chi^2}{4} + \chi + \frac{V_{sbi}}{V_{po}} \right)^{\frac{1}{2}} \right], \tag{2.35}$$

where

$$\chi = \frac{WAqN_d v_s R_c}{V_{po}}. \tag{2.36}$$

In the limiting case where $R_c = 0$, I_{Dsat} reduces to

$$I_{Dsat} = WqN_d A \left[1 - \left(\frac{V_{sbi}}{V_{po}} \right)^{\frac{1}{2}} \right] v_s. \tag{2.37}$$

A typical current-voltage characteristics curve for the ungated FET is shown in Figure 2.11.
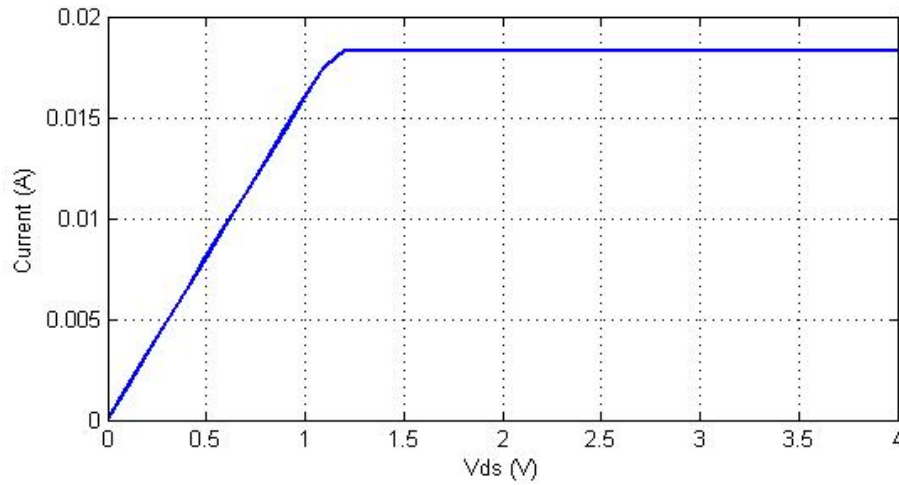
Figure 2.11: Current voltage characteristics of ungated FET.

Chapter 3

DNA Properties and Sensor Model

3.1 The DNA Structure

Deoxyribonucleic acid (DNA) is a biological polymer molecule typically made up of thousands of nucleotide monomers serially arranged in a double-helix consisting of nitrogenous bases, and phosphate group linkages, attached to a backbone of deoxyribose, a pentose sugar. Genetic information is defined over the entire length of the molecule, encoded within the nucleotide sequence. Figure 3.1(a) shows the double helix DNA structure which was first proposed by J. Watson and Crick in 1953 [82] based on x-ray crystallography images by Rosalind Franklin [83]. Figure 3.1(b) shows the "ball-and-stick" molecular appearance of the double helix structure. The structure is made up of two single strands twisted and linked to one another by hydrogen bonding which follows base-pairing rules. The nitrogenous bases, adenine (A), thymine (T), guanine (G), and cytosine (C), are classified as either pyrimidines or purines. Pyrimidines are derived from the heterocyclic compound pyrimidine, and purines are derived from the fused-ring compound purine, with structures shown in Figure 3.2 and Figure 3.3 respectively.

The bases are linked to the deoxyribose sugar through a β-glycosidic linkage from the N-9 position of the purine, or the N-1 position of the pyrimidine to the 1'C position of the sugar to form a nucleoside molecule. (The notation (X-1), denotes the nitrogen or carbon molecule position in the base, and (1'X), denotes the carbon position on the sugar molecule.) The nucleoside molecule is in turn linked to a phosphate group on the 5'C position of the sugar to form a nucleotide molecule
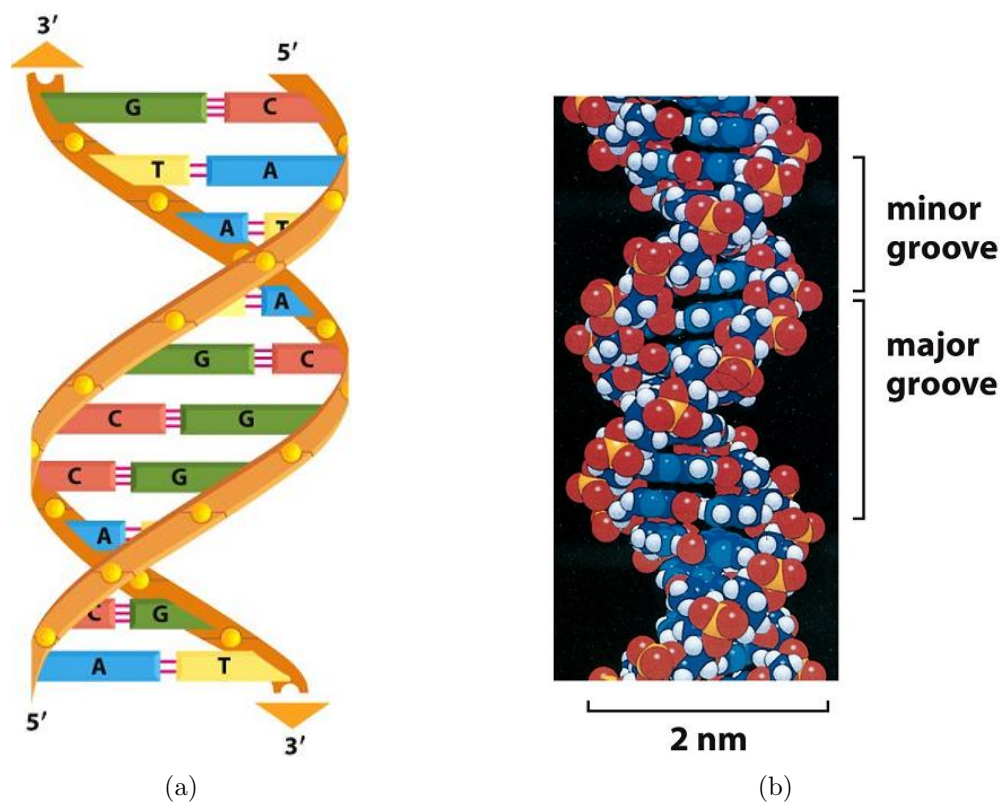
Figure 3.1: DNA molecule [3].
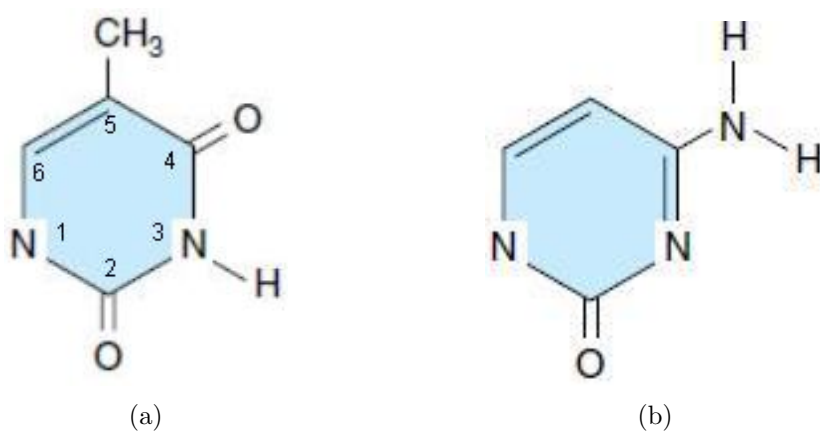
Figure 3.2: Pyrimidine bases (a) Thymine and (b) Cytosine.

called deoxyribonucleotide. Repeated units of various types of nucleotides joined together form polynucleotide polymers that define the nucleic acid DNA. The nucleotides are linked to each other through phosphodiester linkages between the 3'C of a nucleotide and the 5'C of an adjacent one. Figure 3.4 shows a single strand
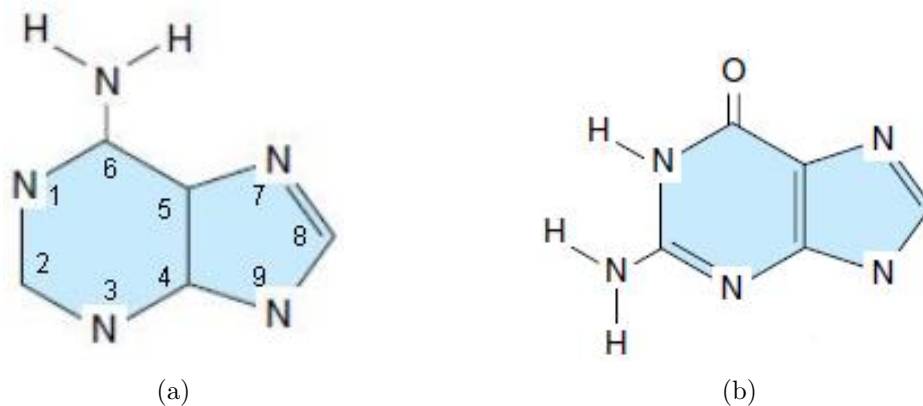
Figure 3.3: Purine bases (a) Adenine and (b) Guanine.

of a DNA polynucleotide formed by four nucleotides with bases guanine, cytosine, thymine, and adenine. The sequence can be defined by the abbreviations of the bases GCTA in the 5'→3' direction, where 5' and 3' designate the carbon on the sugar at each end of the strand.
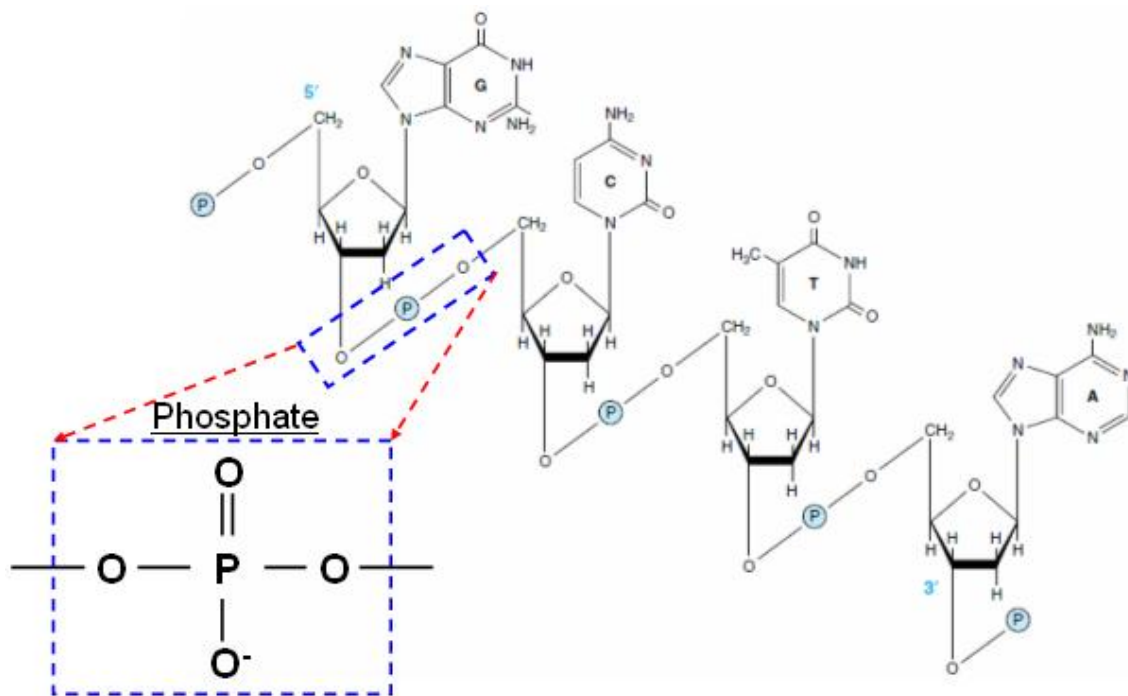
Figure 3.4: Sequence GCTA of a DNA single strand from [3] showing the phosphate group.

Through base pairing, two complementary single strands oriented in opposite

directions ("polarities") join to form the double helix of Figure 3.1. This DNA molecule is completely twisted every 10 base pairs, or 3.4 nm, referred to as the pitch. The base pairs are 0.34 nm apart on the same strand, forming a hydrophobic core with the sugar molecule. The phosphate groups are on the surface, and each group carries a negative charge. The nucleotides are thus negatively charged at neutral pH.

3.2   DNA Bonding and Hybridization

The base pairing behind the duplex molecule is formed by a pyrimidine and purine. The pyrimidine adenine pairs with the purine thymine (A-T) through two H bonds and guanine pairs with cytosine (G-C) through three H bonds. This pairing results in complementary chains that agree with the Watson and Crick's model shown in Figure 3.5.
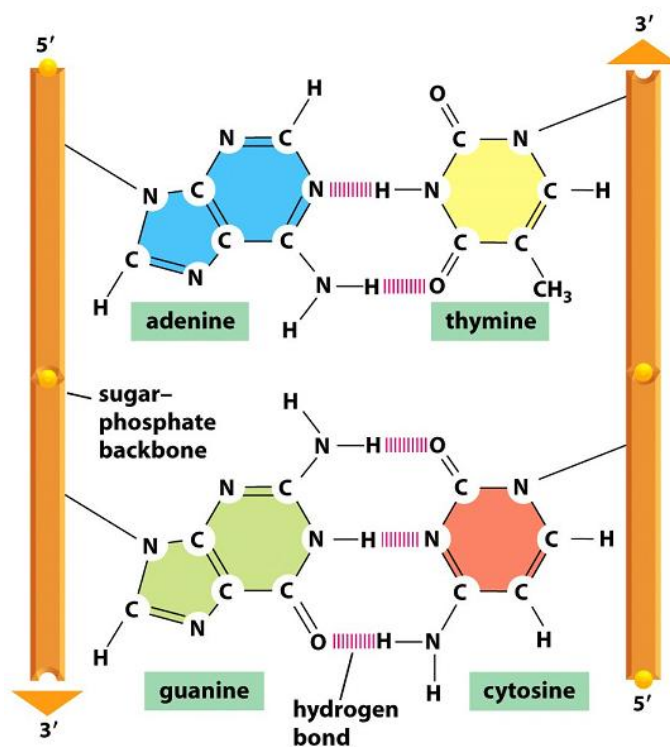
Figure 3.5: Planar view of the double helix showing the H Bonds [3].

The H bonds can be broken at high temperatures in a process called denaturization. In this process, the double helix separates into its single strands. Denaturization can be determined by UV absorption measurements as shown in Figure 3.6.
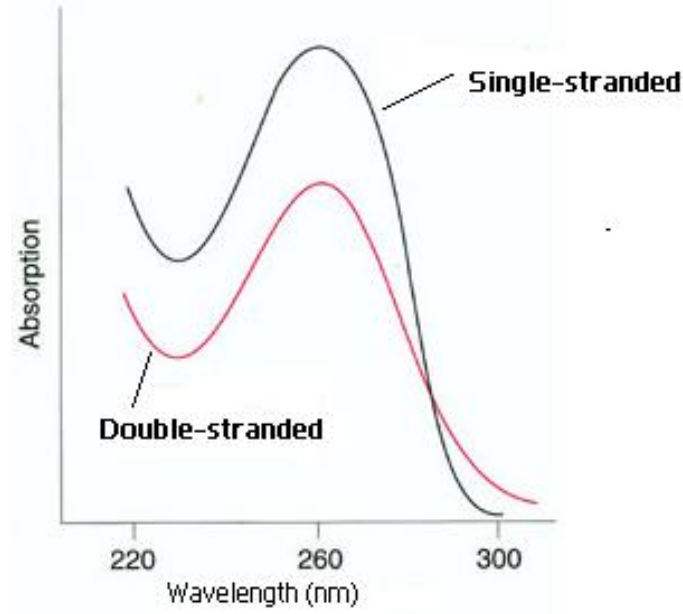
Figure 3.6: DNA absorption spectrum.

At the wavelength of maximum absorption, 260 nm, the denatured single stranded DNA has 40 percent more absorbance than the double stranded native DNA. The low absorbance in double stranded DNA results from the fact that it is a stiff and highly elongated molecule with high viscosity. An increase in temperature reduces the viscosity, leading to the collapse of the DNA molecule in a process called melting. The melting temperature, T_m, is the temperature at which 50 percent melting has occurred. This temperature is affected by the ionic strength in the medium at neutral pH, and the ratio of the G-C base pair content to A-T base pair content of the given strand. The presence of three H bonds per G-C base pair compared to two H bonds per A-T base pair affects the temperature according to

$$T_m = 81.5 + 16.6 \log M + 41(nG + nC) - 500/L_{dna} \ ^{\circ}C \qquad (3.1)$$

where L_{dna} is the length of the DNA duplex in base pairs, M is the salt concentration, and nG and nC are the fractions of G and C in the DNA. For DNA with less than 20 base pairs, a simple formula for calculation of T_m is

$$T_m = 4(G + C) + 2(A + T)\,°\text{C} \tag{3.2}$$

At temperatures below T_m, complementary single strands of DNA begin to re-associate in a process called renaturation. This process is also called hybridization, or annealing, and occurs naturally at room temperature for strands with melting temperature greater than room temperature.

3.3 Genetic Markers and Diseases

Thousands of information-containing elements are encoded in the DNA structure. These elements are called genes, and are contained in a short or a long DNA sequence. When expressed in certain organisms, genetic disorders and some diseases can be identified by specific gene marker sequences, or "alleles". Such diseases include sickle cell disease [84], lyme disease [85], salmonella infection [86], hepatitis C [87] Huntington's disease [88], color blindness [89], and many more. The gene marker alleles are abnormalities associated with specific oligonucleotides, small sequences of DNA up to 30 base pairs long. The abnormalities are caused by small mutations or deletions of bases in the DNA sequence, and can be detected by complementary oligonucleotide primers.

Sickel cell anemia, for example, is a gene defect from a known mutation of a single nucleotide (A to T) in the sequence 5'-CACCTGACTCCTGA**A**-3', to the mutant sequence 5'-CACCTGACTCCTG**T**-3' of the β-globin gene. An allele-specific primer will hybridize only with the mutant (sickle cell) DNA. Table 3.1 shows gene marker alleles for other genetic disorders that could be detected by the biosensor, and their

complimentary allele specific primers that are immobilized on the surface of the field effect biosensor device.

Genetic disorder	Allele DNA Sequence	References
Sickle cell	5'-CACCTGACTCCTGT-3'	[84, 90]
complimentary	5'-ACAGGAGTCAGGTG-3'	
Lyme Disease	5'-ATGCACACTTGGTGTTAACTA-3'	[85, 91]
complimentary	5'-TAGTTAACACCAAGTGTGCAT-3'	
Cystic Fibrosis	5'-TAGTAACCACAA-3'	[92, 93]
complimentary	5'-TTGTGGTTACTA-3'	
Tangier	5'-CCTTGCCTCCTAGTGTAGGATTT-3'	[94]
complimentary	5'-AAATCCTACACTAGGAGGCAAGG-3'	
Salmonella	5'-TATGCCGCTACATATGATGAG-3'	[86, 95]
complimentary	5'-CTCATCATATGTAGCGGCATA-3'	
Hepatitis C	5'-ACCCTCGTTTCCGTACAGAG-3'	[87, 96]
complimentary	5'-CTCTGTACGGAAACGAGGGT-3'	

Table 3.1: Allele specific gene marker sequences for various diseases.

3.4   Immobilization onto GaAs Surfaces

To detect these disease markers, the transducer (GaAs) surface is functionalized with immobilized complimentary ssDNA strands on the gate region of the field-effect device. The immobilization of the probes to the sensor occurs by means of a robust covalent bond between the oligonucleotide probes and the sensor surface. The surface is typically the (100) crystal plane family, produced by epitaxial growth or decapping methods, resulting in evenly spaced crystal planes with square lattice symmetry. These crystal planes are polar with either Ga or As atoms on the surface. The atoms on the surface have two back bonds with other atoms in the bulk material and two unsaturated dangling bonds.

Research on biosensors based on GaAs devices started with the attachment of biomolecules on solid surfaces of metals and semiconductors [97–101]. Parton, et

al., studied the material properties of GaAs, semiconducting polymers, and acoustic waves as platforms for biosensor applications [102]. The first attachment of biomolecules on GaAs was reported by Sheen, et al., in 1992 [103] who attached self-assembled monolayers (SAMs) on the GaAs surface. Sheen concluded that active As sites reacted with molecules, enabling passivation and attachment of other biomolecules on GaAs surface. Other studies on the attachment mechanism, orientation, strength, and composition of biomolecules on bare GaAs surfaces were conducted and reported in [104–113].

The attachment of DNA on GaAs started when Liu, et al., immobilized DNA on gold-covered glass and proposed a solid-support chemistry for DNA reactions [114]. Later, Goede Karste, et al., showed that peptide clusters could self-assemble on semiconductor surfaces [115, 116]. In 1994, Ratner and co-workers [97] studied the orientation of purine and pyrimidine bases, and concluded that the bases self-assemble on gold surfaces in an ordered 2-D lattice, similar to that of a bulk crystal. Steel, et al., of Columbia University investigated the effect of oligonucleotide probe length on assembly onto solid surfaces. Steel concluded that the surface density of thiolated oligonucleotides shorter than 24 bases is mostly independent of probe length, and they conform to an end-attached configuration where each ssDNA strand is bound to the substrate solely through a 5'-end thiol [117]. Ladan, et al., attached and studied the orientation of DNA oligonucleotide probes on a GaAs surface [118, 119]. In his dissertation, Yang performed an extensive study of attachment and characterization of DNA probes on GaAs-based semiconducting surfaces [120]. Yang's investigation showed that non-modified DNA and thiol-modified DNA can attach to the As terminated surface. The bonds involved utilize a strong covalent bond on the 5'-end of the thiol-modified or non-modified DNA. Weak bonds, also reported by Ladan, et al., [118], were also found to exist between the nitrogen, or oxygen of the bases with the As atoms, or between the nitrogen in the bases that could lead

to $\pi - \pi$ interactions between neighboring DNA molecules. The weak bonds allow the DNA molecules to remain on the surface, but they can be removed by ultrasonic cleaning after immobilization [120, 121], or by the inclusion of a mercaptohexanol (MCH) spacer molecule that displaces nitrogen bonds [118, 119].

The specific sequences of oligonucleotides attached could be of the form shown in Table 3.1, such as 5'-AGTCAGTCCTA-3' for the sickle cell gene marker, or a thiol-modified oligonucleotide of the form HS-$(CH_2)_6$-5'-AGTCAGTCCTA-3' for the same gene marker. The DNA oligonucleotides immobilized onto the GaAs surface were found to orient at an angle of about 54° with respect to the GaAs surface [112, 113, 119, 120]. Figure 3.7 shows the orientation of DNA molecules on the biosensor device.
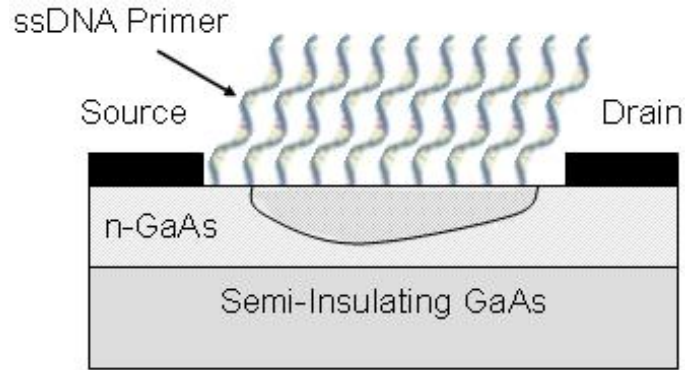
Figure 3.7: Side view appearance of DNA oligonucleotides attached on GaAs surface.

In the proposed DNA sensor device, an immobilized oligonucleotide probe hybridizes with the complementary gene marker ssDNA sequence. This hybridization event is transduced into an electrical signal following charge transfer and accumulation on the sensor surface.

3.5 Charge Transfer Model

The negatively charged DNA strands make it possible to measure both immobilization onto the field-effect transistor surface and specific target DNA binding to

the oligonucleotide probes. DNA sensors based on Bergveld Ion-selective field-effect transistor principles [32] have been developed. The sensors employ an electrolyte-insulator-silicon structure where the DNA oligonucleotides attach to the insulator, (SiO$_2$-electrolyte interface) [48, 49, 122–124], and require an electrode to establish a voltage bias in the solution. On the sensor surface, detection of charge variation is by field-effect current-voltage measurements [122], capacitive measurements [125–127], or electrochemical impedance measurements [128]. The surface charge and surface potential for such Si/SiO$_2$/electrolyte sensors have been modeled by various groups [52, 129–131], and represented by the Graham equation [132]. The equation states that

$$\sigma_0 = \sqrt{8\epsilon_{el}\epsilon_0 kT c_0}\sinh\left(\frac{q\phi_0}{2kT}\right),\tag{3.3}$$

where ϵ_{el} is the permitivity of the electrolyte, ϵ_0 is the permitivity of free space, c_0 is the buffer ionic strength, and ϕ_0 is the surface potential. However, these sensors are also sensitive to pH changes and could be affected by the ionic strength of the electrolyte.

The charge model for our biosensor device is based on the ungated GaAs FET discussed in section 2.3, and shown in Figure 2.9. The underlying model for the current equations are based on the Poisson equation of the form

$$\nabla \cdot [\epsilon\nabla\phi(\mathbf{x})] = -q(n_{FET} + n_s),\tag{3.4}$$

where $\phi(\mathbf{x})$ is the electrostatic potential, and qn_{FET} represents the charge carrier density associated with the doping concentration in the semiconductor. qn_s is the net surface charge density from the unbound surface charge groups. After the immobilization of single-stranded DNA molecules, shown in Figure 3.7, and hybridization

with the complimentary allele molecules, the Poisson equation (3.4) becomes

$$\nabla \cdot [\epsilon \nabla \phi(\mathbf{x})] = -q(n_{FET} + n_{dna}). \tag{3.5}$$

The charge density, qn_{dna}, represents charges from the attachment or hybridization of ssDNA, and from any unbound surface charges. Charges from the attachment of DNA oligomers are affected by the packing density of attached DNA oligomers, oligomer length, and the orientation of the DNA strands described next.

Since the diameter of the DNA molecule is 2.0 nm [3]. The maximum packing density d_{max} possible on 2.0 nm centers is approximately 2.5×10^{13} DNA oligomers/cm^2 immobilized on the surface. The DNA molecule contains negative charges concentrated on the DNA phosphate-sugar backbone. Each nucleotide, hence each base, carries one negative charge. An oligonucleotide of length L_{dna} bases long will have L_{dna} negative charges. For instance, an oligonucleotide that is 20 bases long will have 20 negative charges. The oligonucleotide could take the form of the complimentary allele of any of the specific gene markers in Table 3.1. The charge density ρ_{bound} due to the bound DNA molecules L_{dna} bases long is thus given by

$$\rho_{bound} = d_{max}L_{dna} \qquad \text{charges/cm}^2 \tag{3.6}$$

In an ideal situation, the small lattice constant (0.565 nm) of GaAs results in a surface concentration of atoms (number of atoms/unit area) on the GaAs(100) surface of about 6.257×10^{14} atoms/cm^2 [133]. This concentration results in 1.251×10^{15} potential binding sites/cm^2 since each surface molecule carries two unbound charges. The high number of potential binding sites, compared to the maximum packing density of immobilized DNA, means that unbound surface charges are likely to exist after oligomer immobilization. These unbound charges, with density $\rho_{unbound}$, con-

tribute to the total charge density on the surface, given by

$$qn_{dna} = \rho_{total} = \rho_{bound} + \rho_{unbound} \qquad \text{charges/cm}^2, \tag{3.7}$$

where n_{dna} are the charges in the Poisson equation (3.5). After the hybridization event, the bound charges, ρ_{bound}, are expected to increase, potentially doubling in the event that all immobilized ssDNA oligomers hybridize with complimentary oligomers.

In a non-ideal situation, where the semiconductor is doped, a net surface charge n_s is developed when dopant electrons in the conduction band drop in energy, filling the empty surface band states. This surface charge is given by $n_s = z_{dep}N_D$, where N_D is the doping density, and z_{dep} is the depletion region formed by positive charges of equal magnitude (maintaining charge neutrality). The potential $V(z)$ within the depletion region is given by

$$V(z) = -\frac{q^2 N_D}{2\epsilon\epsilon_0}(z - z_{dep})^2, \tag{3.8}$$

where $z = 0$ is defined at the surface. $V(0)$, the potential of the depletion region, is also referred to as the surface built-in potential, (V_{sbi}). The resulting surface charge, on the order of 10^{12}cm^{-2}, is much smaller than the total surface density of states $\sim 1.25\text{x}10^{15}\text{cm}^{-2}$. The effect of this net surface charge is to reduce the population of dangling bonds, in turn reducing the probability of DNA adsorption.

The tilting nature of the attached DNA molecules shown in Figure 3.7 results in various modifications of this charge model. The tethering of the molecules in this tilted manner could lead to loosely packed molecules, potentially as low as 50% attachment [113]. This results in a decrease in the number of bound charges ρ_{bound}, in (3.7), and an increase in the number of unbound charges $\rho_{unbound}$. Another factor that might affect the distribution of the total charge is the distance of the charges on

the DNA molecule from the sensor surface [132]. DNA oligomers with many bases (large L_{dna}) may have charges substantially far from the surface that can result in a small electric field E_s on the surface. The field due to a charge q_1 along the DNA molecule, at a distance R from the surface can be expressed as

$$E_s = \frac{q_1}{4\pi\epsilon_0\epsilon_r R^2} \qquad \text{V/m} \tag{3.9}$$

Figure 3.8 illustrates the effect of charge distance from the sensor surface on the
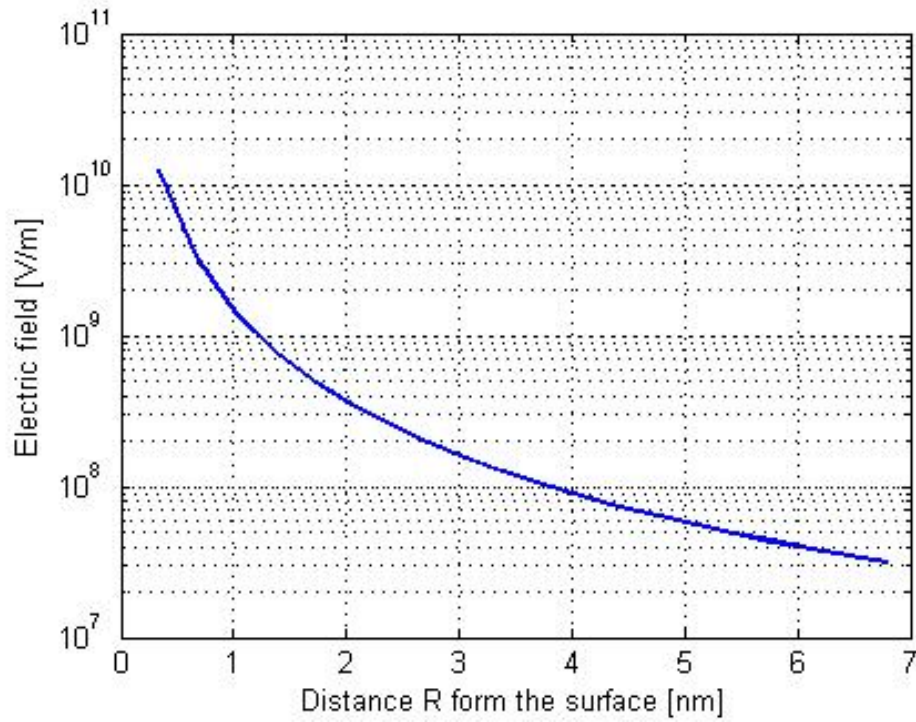
Figure 3.8: The decreasing electric field created by a charge at a distance R from the surface.

electric field it creates at the surface. The equivalent charge density ρ_{bound}, in (3.6), of charges along the DNA strand is thus inversely proportional to $1/R^2$.

The changes in the distribution of charges on the surface and in the DNA layer modulates the conductance of the active channel in the GaAs transistor. The current equations are obtained from the Poisson equation solved self-consistently from the solutions of the Boltzmann transport equation and drift-diffusion equations, the

subject of the next chapter.

Chapter 4

FET Transistor Physical Model

4.1 Electronic Band Structure

The band theory of semiconductors allows us to understand the band structure, electron motion, and electron energies within the allowed energy bands. This theory is important in order to understand the electron energy dependence and quantum mechanical considerations of a periodic crystal potential used in the semi-classical transport model.

4.1.1 Band Structure Parameters

Crystalline semiconductors like GaAs have a repeated structure of the corresponding Bravais lattice. The crystal potential $V(r)$ is thus periodic with

$$V(r + R) = V(r), \tag{4.1}$$

where R is a vector on the bravais lattice. The electronic band structure and the wave function can be obtained from the Hamiltonian, which observes the crystal symmetry of semiconductors. The motion of each electron in the crystal can be described by the Schrödinger equation given by

$$H\psi_n(r) = E_n\psi_n(r) \tag{4.2}$$

with the one-electron Hamiltonian H given by

$$H = -\frac{\hbar^2}{2m}\nabla^2 + V(r), \tag{4.3}$$

where $\psi_n(r)$ is the wave function, and eigenvalues E_n represent the electron energy in an eigenstate n. Each eigenstate can only accommodate a maximum of two electrons of opposite spin according to the Pauli exclusion principle. The Hamiltonian is an energy operator with the first and the second terms in equation (4.3) defining the kinetic energy and potential energy of the particle respectively. Combining equation (4.2) and (4.3) gives the one-body Schrödinger equation of the form

$$\left(-\frac{\hbar^2}{2m}\nabla^2 + V(\mathbf{r})\right)\psi_{n\mathbf{k}}(\mathbf{r}) = E_n\psi_{n\mathbf{k}}(\mathbf{r}). \tag{4.4}$$

The general solution of the above equation, also referred to as the eigenfunction of the equation, takes the form

$$\psi_{n\mathbf{k}}(\mathbf{r}) = exp(i\mathbf{k}\cdot\mathbf{r})u_{n\mathbf{k}}(\mathbf{r}) \tag{4.5}$$

where the function

$$u_{n\mathbf{k}}(\mathbf{r}+\mathbf{R}) = u_{n\mathbf{k}}(\mathbf{r}) \tag{4.6}$$

has the same periodicity as the crystal, and the term $exp(i\mathbf{k}\cdot\mathbf{r})$ describes the variations at large scales. $\psi_{n\mathbf{k}}(\mathbf{r})$ is the Bloch function, and the above solution method is referred to as the Bloch Theorem.

Applying the Hamiltonian one-body Schrödinger equation (4.4) to the Bloch function (4.5) yields equation (4.7) below, satisfied by $u_{n\mathbf{k}}(\mathbf{r})$:

$$\left(\frac{\hbar^2}{2m}(-i\nabla+\mathbf{k})^2 + V(\mathbf{r})\right)u_{n\mathbf{k}}(\mathbf{r}) = E_n(\mathbf{k})u_{n\mathbf{k}}(\mathbf{r}), \tag{4.7}$$

where we note that the factor $exp(i\mathbf{k} \cdot \mathbf{r})$ cancels out. When the wave vector, $\mathbf{k}$, is varied, an energy band for each integer n is defined by the energy eigenvalues. The Bloch function requires $\mathbf{k}$ to be quantized to

$$\mathbf{k} = (k_x, k_y, k_z) \tag{4.8}$$

in the space reciprocal to the crystal generated by the basis vector $\mathbf{a}_i$. This vector is derived from the basis vector $\mathbf{a}_j$ of the bravais lattice by

$$\mathbf{a}_i \cdot \mathbf{a}_j = 2\pi \delta_{ij} \tag{4.9}$$

Any translation vector $\mathbf{G}$ of the reciprocal lattice takes the form

$$\mathbf{G} = l_1 \mathbf{a}_1 + l_2 \mathbf{a}_2 + l_3 \mathbf{a}_3 \tag{4.10}$$

where the l_i are integers. For GaAs with a face-centered cubic lattice and side length a, the reciprocal lattice is a body-centered cubic lattice with sides $4\pi/a$ as shown in Figure 4.1.
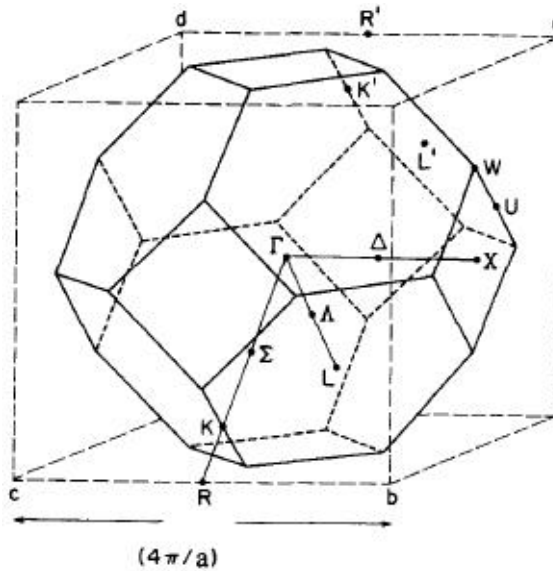
Figure 4.1: Reciprocal lattice of an fcc crystal [4].

The periodicity of the crystals allows **k** to assume all possible values resulting in an extended zone scheme for the band structure. This extended zone scheme may lead to the reciprocal space being too large to classify the Bloch function. However, **k** can be limited according to $\mathbf{k} - 2d\pi/a$ [134], where d is an integer chosen to limit **k** to $[-\pi/a, \pi/a]$. This results in the reduced zone scheme, a volume of the reciprocal space close to the original node $\mathbf{k} = 0$ known as the "first Brillouin zone". For a free particle, a plot of the extended zone scheme and reduced zone scheme are shown in Figure 4.2.
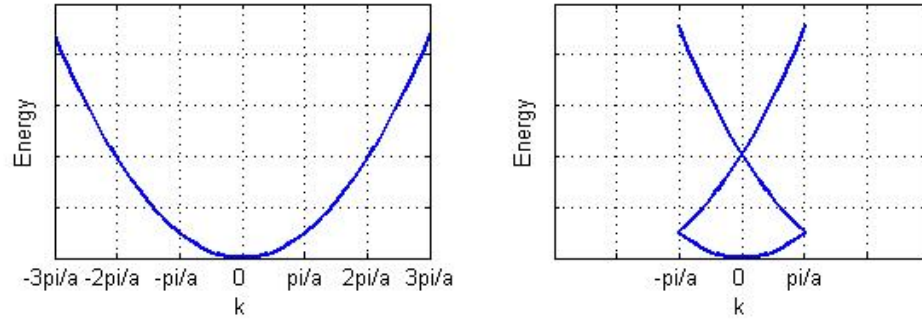
Figure 4.2: Extended zone scheme and reduced zone scheme of a free particle.

In a bulk crystal however, many electrons are interacting with the crystal lattice and other electrons. This interaction makes the calculation of the band structure a many-body problem. The pseudopotential method described by Phillips [135, 136] was developed to solve the Schrödinger equation for bulk crystals where the potential experienced by each individual electron is unknown. The GaAs band structure calculated by Cohen, et al., using the pseudopotential method at room temperature is shown in Figure 4.3(a) [137, 138]. Figure 4.3(b) shows the reduced wave vector for energies close to the top of the valence band and bottom of the conduction band. The spin-orbit splitting results in a split-off valence band $0.34eV$ lower than the degenerate heavy holes and light holes valence bands. The minima of the conduction band located at points $\Gamma(0, 0, 0)$,$L(1/2, 1/2, 1/2)$, and along $X(1, 0, 0)$ have energies that can be obtained as functions of the wave vector. The minima directly above
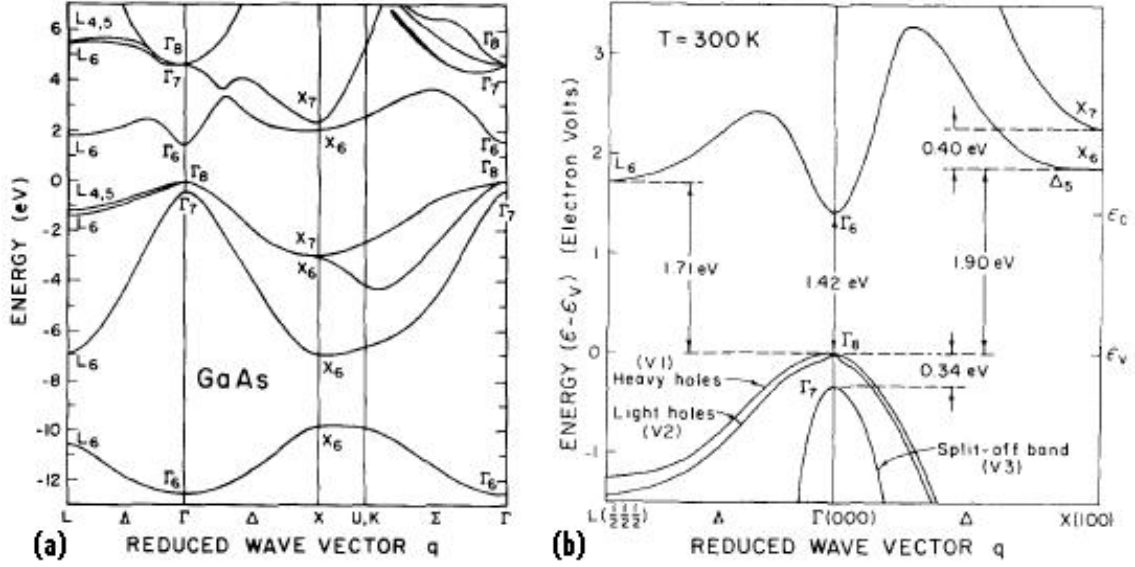
Figure 4.3: Electronic band structure of GaAs calculated by pseudopotential method [4].

the maximum of the valence band is known as the Γ minima and its energy can be defined as

$$E(1 + \alpha E) = \frac{\hbar^2 k^2}{2m} \qquad \text{(spherical for } \Gamma \text{ minima)}, \qquad (4.11)$$

where

$$\alpha = \frac{1}{E_g}\left(1 - \frac{m^*}{m_e}\right)^2 \qquad (4.12)$$

and

$$E(k) = \left(\frac{\hbar^2 k^2}{2}\right)\left(\frac{k_x^2}{m_x} + \frac{k_y^2}{m_y} + \frac{k_z^2}{m_z}\right) \qquad \text{(ellipsoidal for } L \text{ and } X \text{ minima)}, \quad (4.13)$$

where E_g is the energy gap, m^* is the effective mass, and m_e is the free electron mass [6, 139]. The band gap energy, E_g, in GaAs is the energy difference between the conduction band and valence band at the Γ minima point in the middle of the Brillouin zone. This energy is temperature-dependent and can be modeled according

to the Varshni equation [140] of the form

$$E_g(T) = E_{g,T_0} - \frac{\alpha_{E_g} T^2}{\beta_{E_g} + T} \tag{4.14}$$

where E_{g,T_0} is the band gap at $T = 0$ K, and α_{E_g} and β_{E_g} are adjustable Varshni parameters. Table 4.1 shows the temperature dependent energy gap parameters at Γ, L, and X band energies for a temperature range $0 < T < 1000$ K and Figure 4.4 shows the temperate dependence of the band gap in this temperature range. At 300 K the band gap is $1.42eV$ for GaAs as shown on the Figures 4.3 and 4.4.

Band	E_{g,T_0} [eV]	α_{E_g} [eV/K]	β_{E_g} [K]	references
Γ	1.519	5.405x10^{-4}	204	[6, 141, 142]
L	1.815	6.05x10^{-4}	204	[6, 141, 142]
X	1.981	4.60x10^{-4}	204	[6, 141, 142]

Table 4.1: Parameter values for band gap dependence in temperature
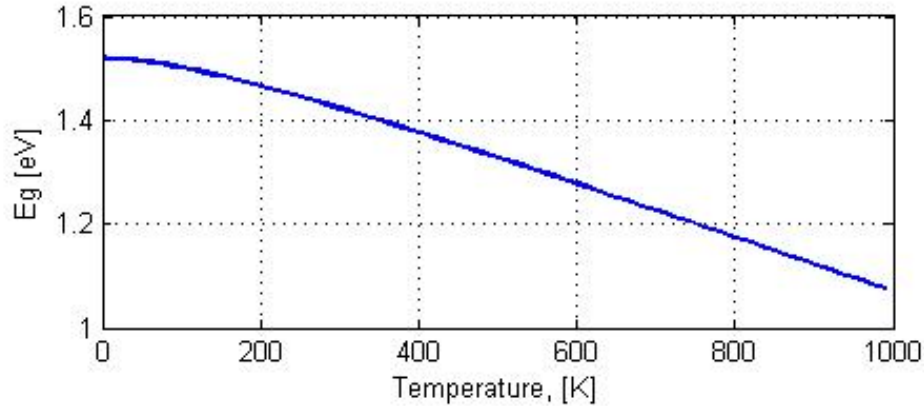
Figure 4.4: Temperature dependence of band gap energy in GaAs.

4.1.2 The k·p Method

In direct band gap semiconductors the local minimum and maximum occur at the zone center ($\mathbf{k}_0 = 0$), and the wave vector $\mathbf{k}$ varies only by a small amount. Many properties of the semiconductor depend on the position and shape of the minima and

maxima at $\mathbf{k}_0$. The $\mathbf{k}\cdot\mathbf{p}$ method is a semi-empirical method particularly convenient for analyzing the band structure near point $\mathbf{k}_0$. The $\mathbf{k}\cdot\mathbf{p}$ method based on the Kane's Model, [139, 143] can be derived from the one-electron Schrödinger equation (4.4). The method can also be written in the form of equation (4.15) below

$$\left(\frac{p^2}{2m} + V(\mathbf{r})\right)\psi_{n\mathbf{k}}(\mathbf{r}) = E_n\psi_{n\mathbf{k}}(\mathbf{r}) \tag{4.15}$$

where $p^2 = -\hbar^2\nabla^2$.

Using the Bloch Theorem, and replacing $\psi_{n\mathbf{k}}(\mathbf{r})$ with the Bloch function equation (4.5), we obtain an equation in $u_{n\mathbf{k}}(\mathbf{r})$ in the form

$$\left(\frac{(\mathbf{p} + \hbar\mathbf{k})^2}{2m} + V(\mathbf{r})\right)u_{n\mathbf{k}}(\mathbf{r}) = E_n(\mathbf{k})u_{n\mathbf{k}}(\mathbf{r}) \tag{4.16}$$

which can be expanded to equation (4.17) below.

$$\left(\frac{p^2}{2m} + \frac{\hbar}{m}\mathbf{k}\cdot\mathbf{p} + \frac{\hbar^2 k^2}{2m} + V(\mathbf{r})\right)u_{n\mathbf{k}}(\mathbf{r}) = E_n(\mathbf{k})u_{n\mathbf{k}}(\mathbf{r}) \tag{4.17}$$

The $\mathbf{k}\cdot\mathbf{p}$ Hamiltonian matrix, from (4.17), is expressed as

$$H^{k\cdot p}(\mathbf{k}) = E_n(\mathbf{k}_0) + \frac{\hbar}{m}\mathbf{k}\cdot\mathbf{p} + \frac{\hbar^2 k^2}{2m} \tag{4.18}$$

where $E_n(\mathbf{k}_0)$ is the simple form of (4.17) at $\mathbf{k}_0$, and given by

$$\left(\frac{p^2}{2m} + V(\mathbf{r})\right)u_{n\mathbf{k}_0}(\mathbf{r}) = E_n(\mathbf{k}_0)u_{n\mathbf{k}_0}(\mathbf{r}) \qquad (n = 1, 2, 3, ...) \tag{4.19}$$

In the term $\mathbf{k}\cdot\mathbf{p}$, $\mathbf{p}$ is the momentum, and the operator $(\hbar/m)\mathbf{k}\cdot\mathbf{p}$ in (4.17) is considered as a perturbation in the Hamiltonian. This method assumes that the values of $E_n(\mathbf{0})$ are known from theory or experiment.

4.1.3 The Effective Mass

In the presence of an applied electric or magnetic field, an electron in a periodic potential is accelerated relative to the lattice and can have a much larger or much smaller effective mass than the mass of a free electron. The **k·p** method can be used to derive the effective mass for nondegenerate and degenerate bands such as the heavy-hole, light-hole, and the spin-orbit split-off bands as described in [4,7,134,144]. In the first Brillouin zone, the $\partial E/\partial(k)$ relationship is parabolic as shown in Figure 4.2. With a known change in k (∂k), the effective mass can be calculated using the equation

$$\frac{1}{m^*} = \frac{1}{\hbar^2}\frac{\partial^2 E}{\partial k^2}. \tag{4.20}$$

For a three dimensional crystal, we can apply the *effective mass tensor* given by

$$\left(\frac{1}{m^*}\right)_{ij} = \frac{1}{\hbar^2}\frac{\partial^2 E}{\partial k_i \partial k_j} \tag{4.21}$$

where i and j are the Cartesian coordinates. Table 4.2 shows the effective mass values for electrons and holes in GaAs relative to the mass of a free electron m_0.

Band	m^* [T = 0 K]	m^* [T = 300 K]
Γ	0.067	0.063
L	0.56	0.56
X	0.85	0.85
Heavy-hole	0.51	0.50
Light-hole	0.082	0.076
Split-off	0.154	0.145

Table 4.2: Effective electron and holes masses (m^*/m_0) [4,6,7].

Effective mass calculations can lead to either effective mass for density of states or for conduction calculations. The isotropic effective mass in GaAs however makes these two values equal.

4.2 Current Equations

Transport equations in semiconductors and semiconductor devices are governed by drift-diffusion current equations derived from the semi-classical Boltzmann transport equation (BTE).

4.2.1 Boltzmann Transport Equation

The BTE is based on the principles of classical statistical mechanics described in the Liouville theorem [145]. It incorporates quantum effects due to the continual decrease in device dimensions of modern semiconductors, and the periodicity of the crystal. The solution of the equation will first be obtained for intrinsic carriers for an undoped semiconductor, and then extended to donors and acceptors for a doped device.

4.2.1.1 Intrinsic Carriers

In an intrinsic semiconductor, the allowed number of states per unit volume can be represented as a function of E according to

$$n_c(E) = 4\pi(2m_e^i)^{3/2}\frac{1}{h^3}(E - E_c)^{1/2} \tag{4.22}$$

for the conduction band and

$$n_v(E) = 4\pi(2m_h^i)^{3/2}\frac{1}{h^3}(E_v - E)^{1/2} \tag{4.23}$$

for the valence band. $n_c(E)$ and $n_v(E)$ are termed the density of states. m_e^i and m_h^i are the density-of-state masses for electrons and holes respectively, obtained from

$$m_v^i = M_c^{2/3}\sqrt[3]{m_l m_t m_t} \qquad v = e, h \tag{4.24}$$

where M_c is the number of equivalent band minima, m_l and m_t are the effective masses longitudinal and transverse to the principal axis of revolution [7]. For three dimensions, the density-of-state masses are obtained from the effective mass tensors m_e^{*i} and m_h^{*i} for electrons and holes respectively according to

$$m_v^i = (det\, m_v^{*i})^{1/3} \qquad v = e, h. \tag{4.25}$$

Electron occupation in each of these states is governed by the distribution function $f(\mathbf{k}, \mathbf{r}, t)$, the probability that a state with wave vector $\mathbf{k}$ is occupied by an electron at position $\mathbf{r}$ at a time t. The equation for this function f is the Boltzmann transport equation given by

$$\frac{\partial f}{\partial t} + \boldsymbol{v} \cdot \nabla_{\mathbf{r}} f + \dot{\mathbf{k}} \cdot \nabla_{\mathbf{k}} f = \left(\frac{\partial f}{\partial t}\right)_{coll}, \tag{4.26}$$

where the first term defines the change in distribution with time, the second and the third define the flow of electrons in real space and $\mathbf{k}$-space respectively. The term on the right is the collision integral over the first Brillouin zone where collisions are assumed instantaneous. This integral can be represented as

$$\left(\frac{\partial f}{\partial t}\right)_{coll} = \int [W(\mathbf{k}', \mathbf{k}) f_{\mathbf{k}'}(1 - f_{\mathbf{k}}) - W(\mathbf{k}, \mathbf{k}') f_{\mathbf{k}}(1 - f_{\mathbf{k}'})] dV_{\mathbf{k}'}, \tag{4.27}$$

where the two terms in the integral represent the increase or decrease of $f_{\mathbf{k}}(\mathbf{r}, t)$ by transition from all other states, and to other states respectively. For conservation of energy, $W(\mathbf{k}', \mathbf{k}) = W(\mathbf{k}, \mathbf{k}')$, and (4.27) simplifies to

$$\left(\frac{\partial f}{\partial t}\right)_{coll} = \int W(\mathbf{k}, \mathbf{k}')(f_{\mathbf{k}'} - f_{\mathbf{k}}) dV_{\mathbf{k}'}. \tag{4.28}$$

In an intrinsic device with uniform equilibrium, (4.28) reduces to

$$\left(\frac{\partial f}{\partial t}\right)_{coll} = 0 \tag{4.29}$$

and this solution is the well-known Fermi-Dirac distribution function:

$$f(E) = \frac{1}{1 + e^{(E-E_f)/kT}} \tag{4.30}$$

which gives the probability that a band state of energy E is occupied by an electron at temperature T, where k is the Boltzmann constant and E_f is the so-called Fermi level. The product of this equation (4.30) and the density of states equation (4.22) gives the electron density in an incremental energy range dE, from which we can obtain the density of electrons n given by

$$n = \int_{E_c}^{\infty} n_c(E)f(E)dE = 4\pi(2m_e)^{3/2}\frac{1}{h^3}\int_{E_c}^{\infty}\frac{(E-E_c)^{1/2}dE}{1 + e^{(E-E_f)/kT}}. \tag{4.31}$$

For conduction band energies that are greater than $3kT$ above the Fermi level, the Fermi-Dirac distribution can be approximated by the Maxwell-Boltzmann distribution. Suppose we introduce the dimensionless variable $x = (E - E_c)/kT$ and substitute it in equation (4.31). The equation becomes

$$n = 4\pi\left(\frac{2m_e kT}{h^2}\right)^{3/2}\int_0^{\infty}\frac{x^{1/2}}{1 + exp[x - (E_f - E_c)/kT]}dx$$

$$= 4\pi\left(\frac{2m_e^* kT}{h^2}\right)^{3/2} exp\left(\frac{E_f - E_c}{kT}\right)\int_0^{\infty} x^{1/2}e^{-x}dx \tag{4.32}$$

The integral is a standard form, evaluating to $\sqrt{\pi}/2$. Thus, (4.32) reduces to

$$n = 2\left(\frac{2\pi m_e^* kT}{h^2}\right)^{3/2} exp\left(\frac{E_f - E_c}{kT}\right)$$

$$= N_C \, exp\left(\frac{E_f - E_c}{kT}\right), \tag{4.33}$$

where

$$N_C = 2\left(\frac{2\pi m_e^* kT}{h^2}\right)^{3/2} \tag{4.34}$$

is called the conduction band effective density of states. The value of N_C is approximately $4.7 \times 10^{17} cm^{-3}$ for GaAs at room temperature (300 K) [6].

In a similar manner, we can obtain the hole density, p, in the valence band as

$$p = N_V \, exp\left(\frac{E_v - E_f}{kT}\right), \tag{4.35}$$

where

$$N_V = 2\left(\frac{2\pi m_h^* kT}{h^2}\right)^{3/2} \tag{4.36}$$

is the valence band effective density of states which is about $7.0 \times 10^{18} cm^{-3}$ for GaAs at room temperature.

For an intrinsic semiconductor, the *mass action law* defines that

$$np = n_i^2, \tag{4.37}$$

where n_i is the *intrinsic carrier density*, and the electron density in the conduction band is equal to the hole density in the valence band, $n = p = n_i$. The intrinsic carrier density n_i is obtained from equations (4.33) and (4.35) according to

$$n_i = \sqrt{np} = \sqrt{N_C N_V} \, exp\left(\frac{-(E_C - E_V)}{2kT}\right), \tag{4.38}$$

where $(E_C - E_V) = E_g$ is the band gap energy. Equating equation (4.33) and (4.35) where $n = p$, and evaluating the Fermi level E_f results in

$$E_f = E_c - \frac{1}{2}E_g + \frac{kT}{2}ln\frac{N_V}{N_C} \tag{4.39}$$

where the Fermi level lies close to the middle of the band gap at any given temperature.

4.2.1.2 Donors and Acceptors in Semiconductors

N-type semiconductors contain a concentration N_D of donors with an ionization energy E_D. Similarly, p-type semiconductors have an acceptor concentration N_A with ionization energy E_A. At high temperatures, some of these donors and acceptors may be ionized and others may not. To maintain charge neutrality, the negative charges (electrons and ionized acceptors) must be equal to the positive charges (holes and ionized donors), that is

$$n + N_A^- = p + N_D^+ \tag{4.40}$$

where N_D^+ and N_A^- are the ionized donors and acceptors respectively. The electron concentration n and hole concentration p are for an extrinsic device in this case, and obtained from the Boltzmann transport equation (4.26). In the presence of an external perturbation, the non-uniform equilibrium solution of the Boltzmann equation is given by

$$f(E) = \frac{1}{1 + e^{(E - E_f + q\phi)/kT}} \tag{4.41}$$

where ϕ is the electric potential. The electron density can now be obtained from equations (4.22) and (4.41) as follows:

$$n = \int_{E_c}^{\infty} n_c(E) f(E) dE = 4\pi (2m_e^*)^{3/2} \frac{1}{h^3} \int_{E_c}^{\infty} \frac{(E - E_c)^{1/2} dE}{1 + e^{(E - E_f + q\phi)/kT}}. \tag{4.42}$$

Suppose we introduce dimensionless variables $x = (E - E_c)/kT$ and $\eta = (E_f - E_c + q\phi)/kT$ and substitute them in equation (4.42). The equation becomes

$$n = 4\pi \left(\frac{2m_e^* kT}{h^2} \right)^{3/2} \int_0^{\infty} \frac{x^{1/2}}{1 + e^{(x - \eta)}} dx \tag{4.43}$$

which can be used to define the electron density in the conduction band minima according to

$$n = 2 \left(\frac{2\pi m_e^* kT}{h^2} \right)^{3/2} \frac{2}{\sqrt{\pi}} \int_0^\infty \frac{x^{1/2}}{1 + e^{(x-\eta)}} dx$$

$$n = N_C F_{1/2}(\eta), \tag{4.44}$$

where N_C denotes the effective density of states in the conduction band and

$$F_{1/2}(\eta) = \frac{2}{\sqrt{\pi}} \int_0^\infty \frac{x^{1/2}}{1 + e^{(x-\eta)}} dx \tag{4.45}$$

is the Fermi-Dirac integral of order $\frac{1}{2}$.

Using a similar approach we can calculate the hole density in the valence band with an analogous equation

$$p = N_V F_{1/2}(\eta) \tag{4.46}$$

where N_V is the effective density of states for the valence band and $\eta = (E_v - E_f - q\phi)/kT$. With donor or acceptor impurities, the semiconductor is said to be degenerate and the mass-action law $np = n_i^2$ does not apply. Instead, np is given by the product of (4.44) and (4.46):

$$np = N_C N_V F_{1/2} \left(\frac{E_f - E_c + q\phi}{kT} \right) F_{1/2} \left(\frac{E_v - E_f - q\phi}{kT} \right) \tag{4.47}$$

The concentration of ionized donors is given by

$$N_D^+ = \frac{N_D}{1 + g_d \, exp[(E_f - E_D^i)/kT]} \tag{4.48}$$

where $E_D^i = (E_c - q\phi - E_{D,ion})$, with an ionization energy $E_{D,ion}$, degeneracy g_d, and donor density N_D characterizing each type of donor. Similarly, ionized acceptor

concentration is given by

$$N_A^+ = \frac{N_A}{1 + g_a\, exp[(E_A^i - E_F)/kT]} \tag{4.49}$$

where $E_A^i = (E_v - q\phi - E_{A,ion})$, with an ionization energy $E_{A,ion}$, degeneracy g_a, and acceptor density N_A characterizes each type of acceptor. Impurity degeneracies for donors is normally, $g_d = 2$ and $g_a = 4$ for acceptors [146].

4.2.2 Drift-Diffusion Model

Drift-diffusion semiconductor equations are obtained from the solutions of the first two moments of the Boltzmann transport equation [6, 147–149] together with the self-consistent solution of the Poisson equation:

$$\nabla \cdot [\epsilon(\mathbf{x})\nabla\phi(\mathbf{x}, t)] = -q[N_D^+(\mathbf{x}) - N_A^-(\mathbf{x}) - n(\mathbf{x}, t) + p(\mathbf{x}, t)] + \rho_T. \tag{4.50}$$

In this equation, $\phi(\mathbf{x}, t)$ is the electrostatic potential, $n(\mathbf{x}, t)$, $p(\mathbf{x}, t)$, N_D^+, and N_A^-, are the charge carriers contributing to the charge density as discussed in section 4.2.1 above, and ρ_T is the charge density of the surface states, charged recombination centers, or traps. The current density for electrons and holes resulting from the first moments of the Boltzmann equation are given by

$$\mathbf{J}_n = qn\boldsymbol{v}_n + qD_n\nabla_n \tag{4.51}$$

and

$$\mathbf{J}_p = qn\boldsymbol{v}_p - qD_p\nabla_p \tag{4.52}$$

for low fields. The first term in the equation is the *drift* component of the current and the second term is the *diffusion* component that corresponds to the concentration gradient. The diffusion coefficients D_n and D_p can be defined by the Einstein

relationship

$$D_v = \frac{\mu_v kT}{q} \qquad v = n, p, \tag{4.53}$$

and the carrier mobilities μ_n and μ_p are discussed in section 4.3.

For high fields where the drift velocity is no longer proportional to the electric field, the current density equations (4.51) and (4.52) become

$$\mathbf{J}_n = q\left(-n\boldsymbol{v}_n(E) + D_n(E)\nabla_n\right) \tag{4.54}$$

and

$$\mathbf{J}_p = q\left(p\boldsymbol{v}_p(E) - D_p(E)\nabla_p\right) \tag{4.55}$$

respectively, where

$$\boldsymbol{v}_n(E) = \mu_n \mathbf{E} \tag{4.56}$$

and

$$\boldsymbol{v}_p(E) = \mu_p \mathbf{E}. \tag{4.57}$$

The electric field $\mathbf{E}$ is given by $\mathbf{E} = -\nabla\phi$. These equations are solved with the continuity equations for electrons and holes given by

$$\frac{\partial n}{\partial t} = \frac{1}{q}\nabla \cdot \mathbf{J}_n + G_n \tag{4.58}$$

and

$$\frac{\partial p}{\partial t} = \frac{1}{q}\nabla \cdot \mathbf{J}_p + G_p, \tag{4.59}$$

which impose the conservation laws for the carriers. G_n and G_p are the generation-recombination rates discussed in Section 4.5.

For this system of equations, the unique solution of the Poisson equation requires specifying the boundary conditions for the structure and contacts. For the GaAs field effect device, Ohmic contacts, Schottky contacts, and surface states are applied

as discussed in Section 4.4. The solution of the coupled drift-diffusion equations and quantum mechanical approach enable us to determine the charge self-consistent solution for the electrostatic potential, quasi Fermi levels, the built-in potential, current densities, and other properties. Numerical techniques used to determine these solutions are discussed in Chapter 5.

4.3 Carrier Mobility

The mobility parameter used in the drift-diffusion model has dependencies on doping density, temperature, and electric field. It is important to account for those dependencies in the analysis and design of semiconductor devices as they may affect the general performance of the device.

4.3.1 Doping concentration

The dependence of mobility on doping can be expressed as

$$\mu_v = \mu_{v,min} + \frac{\mu_{v,max} - \mu_{v,min}}{1 + \left(\frac{N_D}{N_{ref}^v}\right)^{\alpha^v}} \qquad v = n, p \tag{4.60}$$

where $\mu_{v,min}$ is the minimum mobility dominated by the impurity scattering of highly doped material, $\mu_{v,max}$ is the maximum mobility of the undoped material dominated by the lattice scattering, N_D is the concentration of ionized donors, N_{ref}^v is the reference doping density at $(\mu_{v,max} - \mu_{v,min})/2$, and α^v is the Caughey/Thomas model parameter discussed in [150]. Table 4.3 illustrates typical values for GaAs from [150–152] and Figure 4.5 illustrates the mobility as a funtion of doping density where the expression has a resemblance to the Fermi-Dirac function.

Parameter	Electrons	Holes
μ_{min}	1000.0 cm^2/V-s	32 cm^2/V-s
μ_{max}	8200.0 cm^2/V-s	432 cm^2/V-s
N_{ref}	6.0e16 cm^{-3}	1.88e17 cm^{-3}
α	0.55	0.5

Table 4.3: Parameters for doping dependence on mobility.
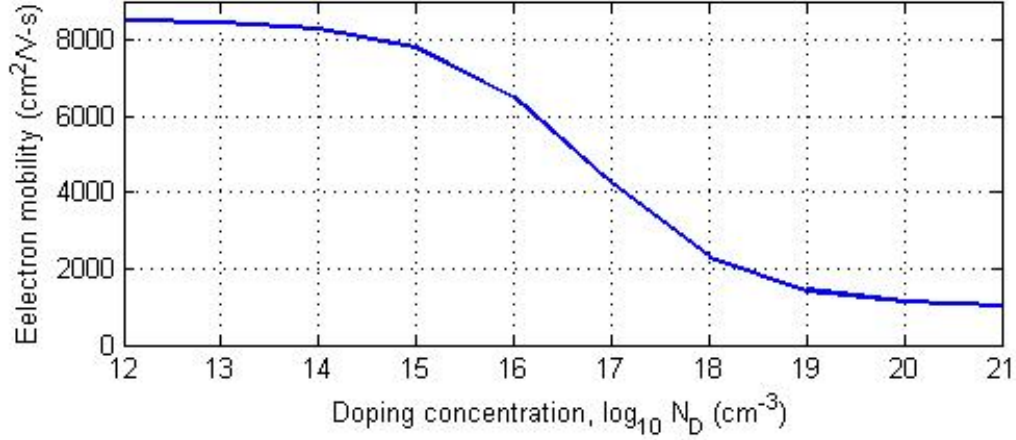
Figure 4.5: Mobility dependence in doping concentration.

4.3.2 Temperature Dependence

The intrinsic or low-doped samples are dominated by lattice vibrations that are temperature dependent. This temperature dependency results in the expression (4.61) below that affects the mobility obtained in equation (4.60) [153].

$$\mu_v(T) = \mu_v \left(\frac{T}{T_0} \right)^{\gamma_v} \qquad v = n, p, \tag{4.61}$$

where $T_0(300 \text{ K})$ is the reference temperature and γ_v is the temperature-dependent parameter. The parameter is normally 1.0 for electrons in GaAs and 2.1 for holes [142, 151].

4.3.3 Electric Field

The high-field mobility of electrons and holes is dependent on the electric field according to

$$\mu_v(E) = \frac{\mu_v^L}{\left[1 + \left(\mu_v^L \frac{E_v}{v_v^{sat}}\right)^{\beta v}\right]^{\frac{1}{\beta}v}} \qquad v = n, p, \tag{4.62}$$

where β^v is an adjustable temperature dependent parameter for both electrons and holes. μ_v is the low field mobility and v_v^{sat} is temperature dependent saturation velocity given by

$$v_v^{sat}(T) = v_0^v - d_{vel}^v(T - T_0) \qquad v = n, p, \tag{4.63}$$

where v_0 is the saturation velocity at the reference temperature $T_0 = 300$ K, and d_{vel}^v is the velocity temperature coefficient.

This equation is not a good fit for GaAs and other compound semiconductors, however, because their v vs E_v curves possess a peak higher than the saturation velocity. The following expression is used frequently to model this behavior.

$$\mu_v(E) = \frac{\mu_v^L + v_v^{sat}\frac{(E_v)^{\beta-1}}{(E_v^{pk})^\beta}}{1 + \left(\frac{E_v}{E_v^{pk}}\right)^\beta} \qquad v = n, p, \tag{4.64}$$

where E_v^{pk} is the peak electric field at maximum velocity $v = \mu_v E_v$, beyond which the velocity of electrons decreases with increasing electric field in a phenomenon known as *negative differential resistivity*. This peak electric field is temperature dependent according to

$$E_v^{pk}(T) = E_0^v - d_E^v(T - T_0) \qquad v = n, p \tag{4.65}$$

In (4.65), E_0^v is the peak electric field at temperature T_0 and d_E^v is a temperature dependent coefficient. Numerical values for the parameters used in equation (4.62) and (4.64) have been obtained for Si [150], [154] and GaAs [65], [155]. At 300 K

typical parameters values for Si and GaAs are shown in table 4.4.

Material	v_n^{sat}[cm s^{-1}]	β_n [ ]	E_n^{pk}[V cm^{-1}]	references
GaAs	1.0x10^7	4	3.3x10^3	[65]
Si	1.1x10^7	2		[150, 154]

Table 4.4: Velocity saturation coefficients for GaAs and Si.

Figure 4.6 shows a plot of mobility vs electric field for GaAs (equation (4.64)) and silicon (equation (4.62)), using the values in Table 4.4 respectively. The resulting velocity-field curves ($v = \mu_v E_v$) are shown in Figure 4.7, which resembles Figure 2.2 of Chapter 2, and were also obtained in [155] and [156].
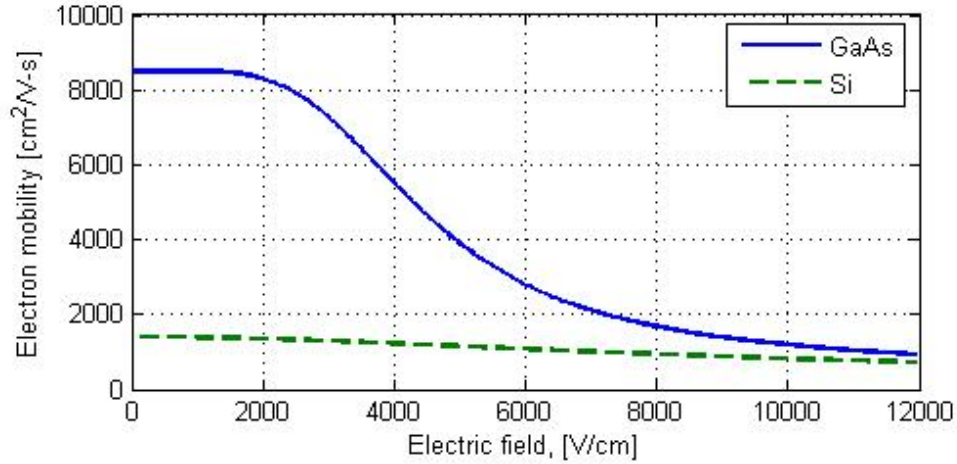
Figure 4.6: Mobility dependence in electric field.

The GaAs curve shown in Figure 4.7 portrays a peak at the critical field, E_n^{pk} before settling on the saturation velocity because of the negative differential mobility.

4.4   Boundary Conditions

To model a short gate-length planar MESFET device, specific boundary conditions must be specified at the boundaries and interfaces of the semiconductor device. These conditions are required for the unique solutions of the coupled second-order partial differential equations which include the elliptic Poisson equation and
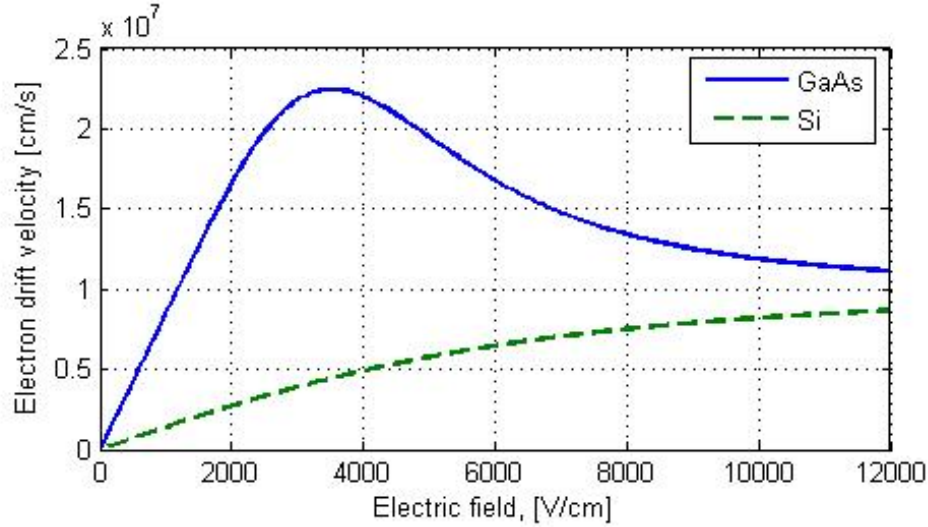
Figure 4.7: Drift velocity dependence in electric field.

parabolic continuity equations. On the boundaries and surfaces, semiconductor materials can be bounded by insulators, metals, or other semiconductor materials forming interfaces called heterojunctions. Here, we will consider semiconductor-metal contacts that can be either Ohmic or Schottky, and surface states will be discussed in section (4.4.3). It is assumed that the potential and carrier gradients normal to the rest of the surfaces are zero for a free standing device. This means that $\frac{\partial \psi}{\partial x}, \frac{\partial n}{\partial x} = 0$ and $\frac{\partial \psi}{\partial y}, \frac{\partial n}{\partial y} = 0$ for boundaries parallel to the x-axis and y-axis respectively.

4.4.1 Ohmic Contacts

Ohmic contacts are non-rectifying semiconductor-metal junctions with a very small space charge region. In a highly doped semiconductor, this implies large band bending and a very thin barrier at the interface, making it easy for charge carriers to tunnel through the energy barrier. Figure 4.8 shows an n-type semiconductor-metal ohmic contact.

The metal quasi-Fermi level is equal to the semiconductor quasi-Fermi level. The thin barrier allows charge carriers to both exit the device or enter the device,
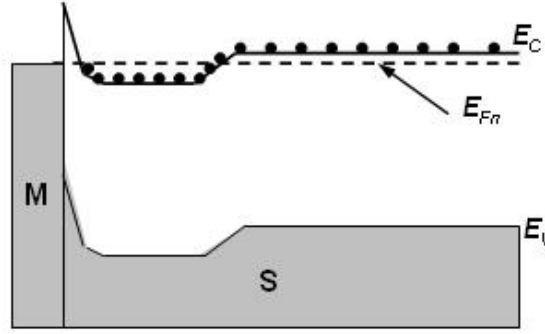
Figure 4.8: An ohmic boundary.

allowing the contacts to behave like charge reservoirs. This leads to high current densities at low voltage drops which (by Ohm's law) results in low resistance at the contacts. A charge has to be assigned a constant value at the ohmic contacts and the electrostatic potential can be determined from the local charge neutrality conditions at the boundary. In this case, we consider the contact carrier temperatures T_n for electrons and T_p for holes as constants, set equal to the lattice temperature. For charge neutrality at an ohmic contact $(n - p - N = 0)$, artificial boundaries for isolating the device are required and approximated by the Neumann boundary conditions:

$$\frac{\partial V(x)}{\partial(x)} = \frac{\partial n(x)}{\partial(x)} = \frac{\partial p(x)}{\partial(x)} = 0. \tag{4.66}$$

Dirichlet boundary conditions are applied for the electrostatic potential $V(x)$, and the electron and hole concentrations n_D and p_D respectively at the ohmic contacts. A uniform potential is applied in the form of an instantaneous drain voltage $\phi = V_D$ and source voltage $\phi = V_S$ at the drain and source contacts respectively, and the following boundary conditions are imposed

$$V(x) = V_{ap} + V_{bi}, \tag{4.67}$$

where V_{ap} denotes the applied potential on the contact and V_{bi} is the built-in potential of the semiconductor. The built-in potential depends on the doping concen-

tration, the temperature, and on the semiconductor material and can be given as a logarithmic function

$$V_{bi} = k_B T \, ln \left(\frac{n_D}{n_i} \right), \tag{4.68}$$

where $k_B T$ represents the thermal voltage. For very high doping where the contact resistance tends to zero (i.e., ideal ohmic contacts),

$$np = n_i^2 = N_C N_V exp \left(\frac{-(E_C - E_V)}{k_B T} \right), \tag{4.69}$$

where n_i is the intrinsic carrier concentration, which depends on material and temperature. $(E_C - E_V) = E_g$, is the band gap energy, and N_C and N_V are the effective density of states for the conduction band and valence bands respectively, as was discussed in section 4.2.1.

This theory leads to the applied Dirichlet boundary conditions for electron and hole concentrations n_D and p_D, expressed respectively as

$$n_D = \frac{1}{2} \left(N + \sqrt{N^2 + 4n_i^2} \right) \tag{4.70}$$

$$p_D = \frac{1}{2} \left(-N + \sqrt{N^2 + 4n_i^2} \right), \tag{4.71}$$

where N is the net concentration of dopants. We can then calculate the built-in potential V_{bi} by substituting equation (4.70) or (4.71) into equation (4.68) above, obtaining

$$V_{bi} = k_B T \, ln \left[\frac{1}{2n_i} \left(N + \sqrt{N^2 + 4n_i^2} \right) \right] \tag{4.72}$$

or

$$V_{bi} = -k_B T \, ln \left[\frac{1}{2n_i} \left(-N + \sqrt{N^2 + 4n_i^2} \right) \right] \tag{4.73}$$

respectively.

4.4.2 Schottky Contacts

A semiconductor-metal contact with a barrier height greater than the thermal volt-age ($q\phi_B > k_B T$) is referred to as a Schottky barrier. This barrier gives a fixed energy difference between the Fermi level and the conduction band edge, deter-mined by the surface states. A low doping concentration less than the density of states in the conduction band or valence band exists at the contact due to band bending. Figure 4.9 shows the formation of a Schottky contact before and after a metal and an n-type semiconductor are brought together. The metal work func-
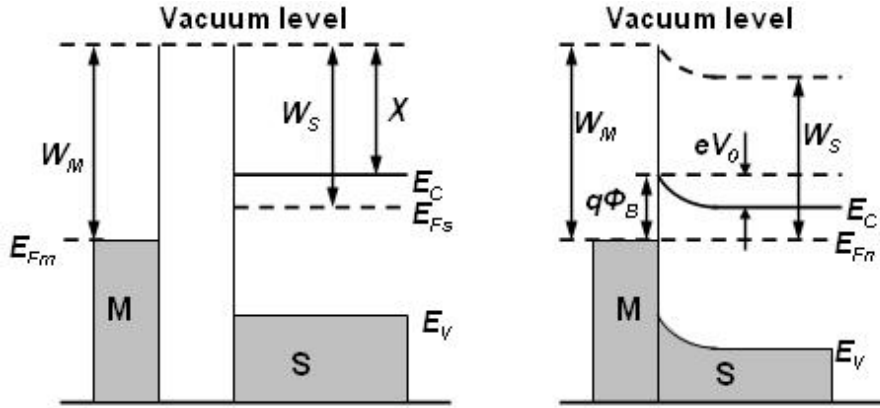
Figure 4.9: A Schottky boundary.

tion in this case is greater than the semiconductor work function ($W_M > W_S$), the more energetic electrons from the semiconductor conduction band can readily tunnel into the metal, creating an electron-depleted region near the surface of the semiconductor. This region creates a contact potential $eV_0 = W_M - W_S$ called the *built-in potential*. The barrier height of the electrons moving from the metal to the semiconductor $q\phi_B$, is given by

$$q\phi_B = W_M - \chi = eV_0 + (E_C - E_{Fn}) \tag{4.74}$$

where χ is the electron affinity of the semiconductor. As seen in Figure 4.9, $(E_C - E_{Fn})$ increases towards the contact showing a low carrier concentration given by

$$n = N_C \, exp\left(\frac{-(E_C - E_{Fn})}{k_B T}\right) \tag{4.75}$$

in the electron-depleted region.

This analysis assumes pure contact between the metal and semiconductor without any other interfacial layers. In a non-ideal case, interfacial layers, interface states, and chemical reactions on the semiconductor surface can alter the barrier height. Although this can be undesirable in other FET devices, it provides an ideal platform for the devices to be used in chemical sensing and biosensor applications. Hence, the same concept used in modeling the Schottky barrier can be used to model semiconductor interactions with biomolecules.

In Schottky contacts, Dirichlet boundary conditions apply to the electrostatic potential and the current density. For the electric potential,

$$\phi = V_{applied} + V_{Schottky}, \tag{4.76}$$

where $V_{Schottky}$ is set to the energy difference between the barrier height, and the energy between the conduction band and Fermi level in an intrinsic semiconductor:

$$V_{Schottky} = \phi_B - \frac{E_g}{2q} + \frac{k_B T}{2q} ln\left(\frac{N_C}{N_V}\right), \tag{4.77}$$

where E_g denotes the bandgap energy. The current density through the Schottky interface is calculated as follows

$$\mathbf{J}_n \cdot \hat{n} = -q\boldsymbol{v}_n \cdot (n_0 - n_S) \tag{4.78}$$

$$\mathbf{J}_p \cdot \hat{n} = -q\boldsymbol{v}_p \cdot (p_0 - p_S), \tag{4.79}$$

where $\hat{n}$ is the outward oriented vector normal to the interface, and n_S and p_S are the carrier concentrations at the surface given by

$$n_S = N_C \, exp \left(\frac{-(E_C + eV_0)}{k_B T} \right) \tag{4.80}$$

$$p_S = N_V \, exp \left(\frac{E_V - eV_0}{k_B T} \right), \tag{4.81}$$

and n_0 and p_0 are the equilibrium electron and hole density concentrations given by

$$n_0 = N_C \, exp \left(\frac{-q\phi_B}{k_B T} \right) \tag{4.82}$$

$$p_0 = N_V \, exp \left(\frac{-E_g + q\phi_B}{k_B T} \right), \tag{4.83}$$

where an assumption of infinite recombination rate applies. The current density is also proportional to the surface recombination rates $\boldsymbol{v}_n$ and $\boldsymbol{v}_p$ for electrons and holes respectively given as

$$\boldsymbol{v}_n = \sqrt{\frac{k_B T}{2\pi \cdot m_n}} = \frac{A_n^* T^2}{q N_C} \tag{4.84}$$

$$\boldsymbol{v}_p = \sqrt{\frac{k_B T}{2\pi \cdot m_p}} = \frac{A_p^* T^2}{q N_V}, \tag{4.85}$$

where A_n^* and A_p^* are defined by

$$A_{n,p}^* = \frac{4\pi \cdot q \cdot m_{n,p} \cdot k_B}{h^3}, \tag{4.86}$$

also known as the effective Richardson constants for electrons and holes, respectively, typical for thermionic emission processes.

4.4.3   Surface States

In GaAs, the Ga and As atoms are covalently bonded. Each As atom on the (100) surface has two bonds with Ga atoms from the layer below, leaving two other unsaturated free bonds responsible for the surface electronic states that strongly affect the behavior of GaAs semiconductor surfaces. These 'dangling' unsaturated free bonds give rise to states other than the Bloch-state bands, and often lie energetically in the bulk band gap. The unsaturated bonds can also rearrange themselves leading to surface reconstruction, or can become passivated by a monolayer of adatoms such as oxygen. We will assume a perfectly terminated periodic crystal, for simplicity, without surface reconstruction or passivation. The crystallographic density of surface atoms can be in the range of 10^{14}cm^{-2}, resulting in a very large density of surface states (e.g 1 state per surface atom) acting as donors or acceptors [157, 158].

The surface states have their levels in the band gap placed at a position $1/3E_g$ above the valence band. The large density of states at the position of the surface states results in the formation of a space charge layer at the surface where the Fermi level becomes "pinned" at the surface state energy. In this action, the electrons captured in the surface levels form a dipole layer which screens the semiconductor interior. This Fermi level pinning is similar to Schottky barrier pinning, as can be seen in Figure 4.10. From Figure 4.10, the average energy of the pinned states
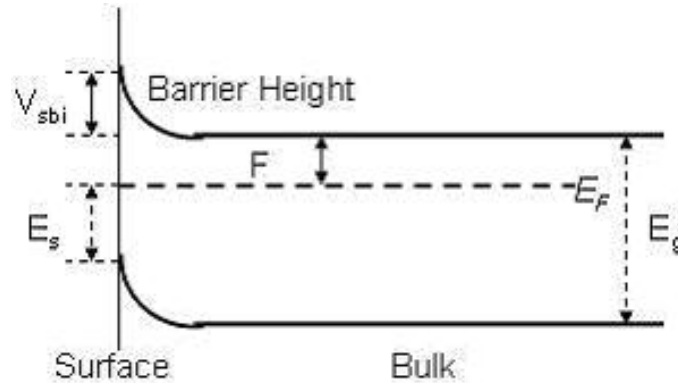
Figure 4.10: Pinning of Fermi level with large surface density of states.

is E_s above the valence band, where the surface states stabilize the Fermi level. As a result, a barrier is formed inside the semiconductor which equals the band bending. For an n-type GaAs whose band gap energy is $1.42eV$, the high density of surface states means a high electronegativity that can lead to energy barrier values of $0.8 - 0.9eV$ at the surface [157].

The deposition of metals causes the generation of new states also positioned in the band gap, as in the case of a MESFET. Metals with various work functions can result in variations of the barrier and thus the barrier potential. The surface states can also be decreased by covering the surface with a thin layer of natural oxide, a technology used for silicon MOS transistor production. In this research, the surface states are controlled by depositing biomolecules such as DNA which bind to the surface molecules of the GaAs semiconductor [118, 120]. The attachment of ssDNA biomolecules on the surface of GaAs and the binding of their complement molecules (to form double stranded DNA) results in changes in the surface states at each stage. The attachment and hybridization process results in charge transfer, hence variation of the contact barrier, depletion depth and channel electrical properties, as described for the ungated FET in Section 2.3 and in Figure 2.9.

4.5   Carrier Generation and Recombination

The generation of electron-hole pairs can occur when energy is available which is significantly greater than that of the band gap. This results in transfer of electrons from the valence band to the conduction band. A reciprocal process corresponding to the transfer of electrons from the conduction band to the lower energy valence band is also possible and is called electron-hole recombination. These generation-recombination processes involve the creation or annihilation of photons and can be radiative or nonradiative, leading to different possible classifications, outlined next.

4.5.1 Direct Generation-Recombination Model

Generation-recombination is a radiative process that involves direct band-to-band transfer of electrons from the conduction band to the valence band. In recombination of electron-hole pairs, a photon with energy equal to the band gap energy is emitted. The generation mechanism involves the absorption of energy greater than the band gap energy in the form of a photon ($E_{photon} > E_g$). The generation-recombination rate is proportional to the excess carrier density and is modeled as follows

$$R_{DIR} = R_n - G_n = C_{DIR}\left(np - n_i^2\right) \tag{4.87}$$

where R_n is the recombination rate, G_n is the generation rate, and ($n_i = n_o p_o$) is the intrinsic carrier density where n_o and p_o are the electron and hole concentrations at thermal equilibrium. C_{DIR} is a capture coefficient with typical values of $1.1\text{x}10^{-10}$ [142] to $7.2\text{x}10^{-10}\text{cm}^3/\text{s}$ [159] for GaAs. This mechanism is predominant and very important for direct band gap semiconductor materials such as GaAs, InAs, InP, and GaN for applications in optoelectronics.

4.5.2 Shockley-Read-Hall Recombination

Also known as trap-assisted generation/recombination, this mechanism involves electrons or holes occupying a trap energy level within the band gap caused by structural defects or presence of foreign particles. As a final state, the electrons and holes move to the conduction band and valence band respectively for generation, or both to the valence band state for recombination. This generation/recombination rate is modeled using the *Schockley-Read-Hall* [160] equation

$$R_{SRH} = \frac{np - n_i^2}{\tau_p\left(n + n_1\right) + \tau_n\left(p + p_1\right)}, \tag{4.88}$$

where n_1 and p_1 are defined as

$$n_1 = N_c\left(T_L\right) exp\left(\frac{E_T - E_c}{k_B T_L}\right) \qquad (4.89)$$

$$p_1 = N_v\left(T_L\right) exp\left(\frac{E_v - E_T}{k_B T_L}\right), \qquad (4.90)$$

where T_L is the lattice temperature, and τ_p and τ_n are lattice temperature dependent generation-recombination lifetimes expressed as

$$\tau_n = \frac{1}{\sigma_{T,n} N_T v_n} \qquad (4.91)$$

$$\tau_p = \frac{1}{\sigma_{T,p} N_T v_p}, \qquad (4.92)$$

where N_T is the trap density, $\sigma_{T,n}$ and $\sigma_{T,p}$ are the trap capture cross sections for electrons and holes respectively, and v_n and v_p are the electron and hole thermal velocity at room temperature expressed as

$$v_v = \sqrt{\frac{3 k_B T_L}{m_{c,v}^*}}, \qquad (4.93)$$

where $v = n$ for electrons and $v = p$ for holes. The recombination rate is maximum when the trap energy level E_T is midway between the gap and $n_1 = p_1 = n_i$.

4.5.3 Auger Recombination

This is a three particle process that involves direct recombination of an electron and hole with the energy released being absorbed by a third particle (electron or hole). This third particle is raised to a higher energy. The recombination rate for this mechanism is affected by the density of electrons or holes that receive energy

after the recombination (or release energy after generation), modeled as

$$R_{AU} = \left(C_n^{AU} n - C_p^{AU} p \right) \left(np - n_i^2 \right),$$ (4.94)

where C_n^{AU} and C_p^{AU} are Auger coefficients of electrons and holes respectively.

4.5.4 Surface Recombination

As seen in Section 4.4.3, the surface of semiconductors contains active dangling bonds that can contain a large number of recombination centers. This can be modeled as trap-assisted recombination, given by

$$U_S = \frac{np - n_i^2}{\tau_p \left(n + n_1 \right) + \tau_n \left(p + p_1 \right)},$$ (4.95)

where

$$\tau_n = \frac{1}{N_{st} v_{th} \sigma_n}$$ (4.96)

and

$$\tau_p = \frac{1}{N_{st} v_{th} \sigma_p}.$$ (4.97)

In (4.96) and (4.97), v_{th} is the thermal velocity, and σ_n and σ_p are the trap capture cross sections for electrons and holes respectively. This expression is similar to the Schockley-Read-Hall expression (4.88), where the surface states per unit area, N_{st}, is different, given that the density of traps exists only at the semiconductor surface.

Chapter 5

Numerical Techniques

The simulation study for the GaAs FET-based DNA biosensor is done using the nextnano software. nextnano is a device simulation tool for nano-scale semiconductor quantum structures and devices. The software can calculate a wide range of physical properties of devices using an extensive database for Si/Ge, II-VI, and III-V semiconductors, and electrolyte materials [161, 162]. In the software, device physical behavior and semiconductor equations are calculated with various numerical techniques. In this chapter, we outline the numerical techniques used for our study. The numerical approaches were selected to suit our needs of calculating semiconductor transport equations incorporating quantum mechanical effects. The methods outlined below were used in the calculations of the electronic band structure, discretization, and obtaining the self-consisted solution of the coupled Schrödinger, Poisson, and current equations.

5.1   Envelope Wave Approximation

The electronic band structure of semiconductor devices can be calculated using the envelope function approximation (EFA), originally developed by G. Bastard [163, 164]. The envelope function is a slow varying function that outlines the amplitudes of a rapidly varying signal, as shown in Figure 5.1.

The envelope approximation, used in the Schrödinger equation, takes the form

$$\psi(\mathbf{r}) = \sum_{\mathbf{k}} F(\mathbf{k}) e^{i\mathbf{k}\cdot\mathbf{r}} u_{\mathbf{k}}(\mathbf{r}) \tag{5.1}$$
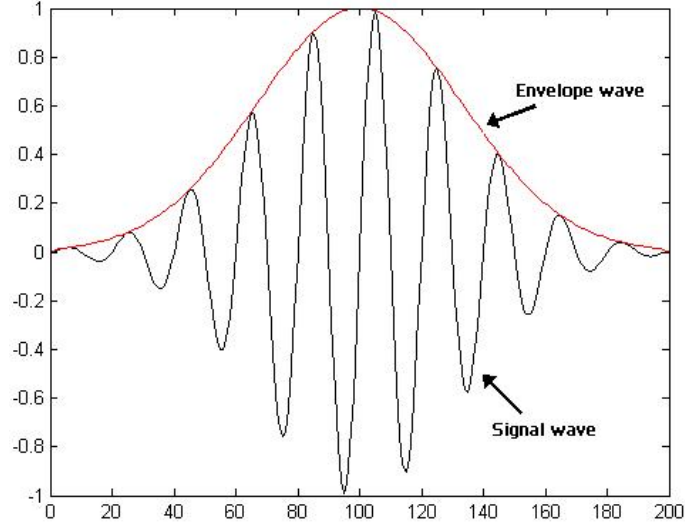
Figure 5.1: The envelope wave and the signal wave.

where the Bloch wave $\psi(\mathbf{r})$, given in (4.5), describes the energy eigenfunctions for mobile charge carriers. The summation represents the full wave function for the Hamiltonian which shows the envelope approximation. $F(\mathbf{k})$ is the envelope wave that is summed over all $\mathbf{k}$ values.

This envelope function approximation is applied to solve the $\mathbf{k}\cdot\mathbf{p}$ method described in section 4.1.2. In the $\mathbf{k}\cdot\mathbf{p}$ approximation, we use the effective mass approximation (EMA) model, in which only one band is considered. The $\mathbf{k}\cdot\mathbf{p}$ Hamiltonian matrix (4.18) for EMA reduces to a function of $\mathbf{k}$ given by

$$H_{EMA}(\mathbf{k}) = E_n(\mathbf{k}_0) + \frac{\hbar^2}{2}\mathbf{k} \cdot \frac{1}{m^*}\mathbf{k}, \tag{5.2}$$

where m^* is the effective mass tensor given by (4.21). The envelope function Hamiltonian for the conduction band, subject to an external potential V_{ext}, is then given by

$$H_{EMA}^{EA} = -\frac{\hbar^2}{2}\nabla \cdot \left(\frac{1}{m^*}\right) \nabla + E_C + V_{ext} \tag{5.3}$$

where $E_C = E_n(\mathbf{k}_0)$ is the energy of the conduction band at $\mathbf{k} = \mathbf{k}_0$ [149].

Computing the electronic structure with the $\mathbf{k}\cdot\mathbf{p}$ envelope function approxima-

tion involves very large matrix eigenvalue systems. Solving these matrix systems require efficient iterative methods. Arnoldi iteration, which computes the eigenvalues of a large sparse or structured matrix [165], is employed to solve the matrix systems. The Arnoldi iterations are implemented using the ARPACK software package [166]. ARPACK is efficient for eigenvalue methods involving sparse real and complex Hermitian matrices. These matrices result from the discretization of the $\mathbf{k} \cdot \mathbf{p}$ equations by the finite difference method.

5.2 Finite Difference Method

The semiconductor partial differential equations to be solved are multi-dimensional and non-linear in nature. To achieve versatile and accurate results, the solution of these coupled partial differential equations must calculated using a numerical approach. The finite difference method with box integration, described in [147, 153, 167], is applied to the coupled equations, and the software implementation for our computations are detailed in [149, 168]. In the finite difference method, the computational domain described by the device geometry is partitioned into a finite number of subdomains, or boxes, surrounded by mesh points. In the boxes, material properties are assumed to be constant, and currents defined on the boundaries are similar for all boxes sharing a mesh line. The mesh lines are parallel to the coordinate axis, and the meshes formed are non-uniform for greater accuracy in high derivatives, and time and memory saving for low derivatives [147]. Figure 5.2 shows the finite difference discretization for an ungated transistor device.

Discretization is performed on every mesh point which invokes its four nearest neighbors, on a scheme known as classical five-point discretization. This scheme is illustrated in Figure 5.3. The five-point discretization scheme uses a control box
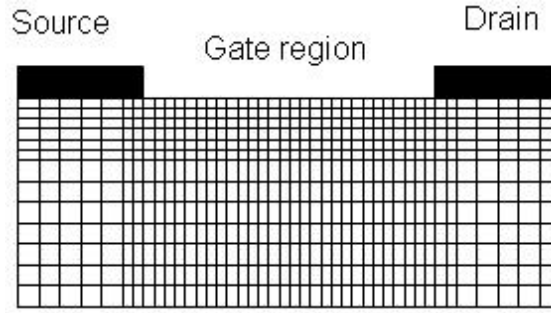
Figure 5.2: Finite difference mesh for an ungated transistor.
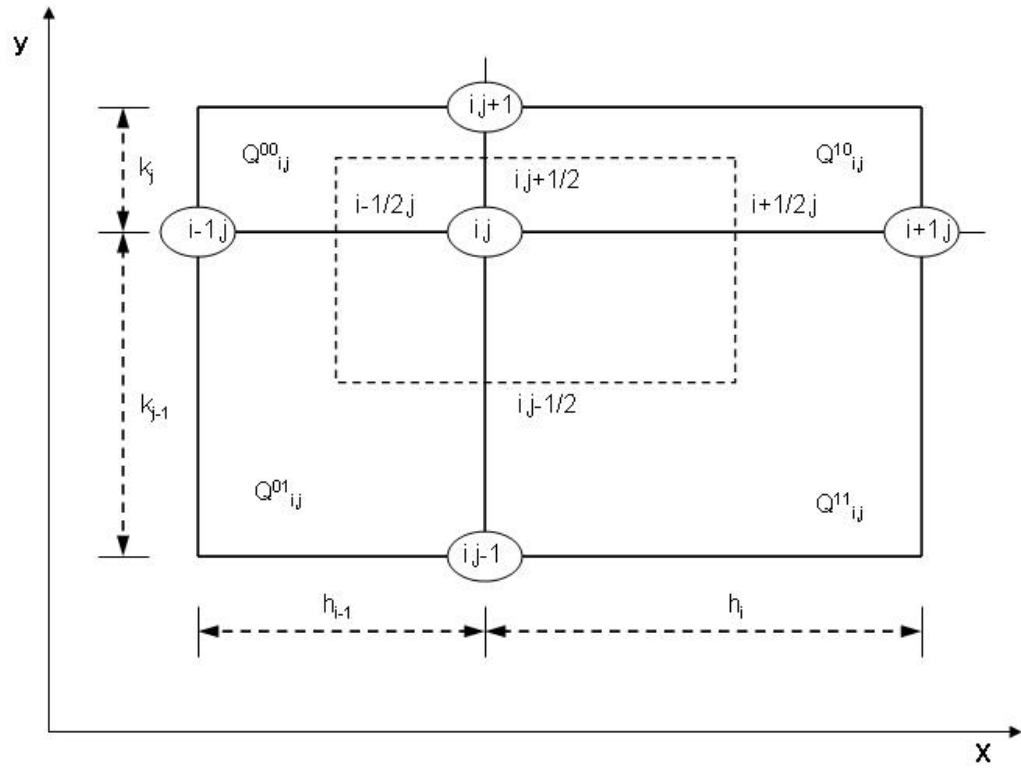
Figure 5.3: Grid node representation in a finite difference box integration scheme.

shared by the four neighboring quadrants around the mesh point represented by

$$u_{i,j} = u(x_i, y_j) \qquad i = 1, 2, 3, ...N_x, \qquad j = 1, 2, 3, ...N_y \qquad (5.4)$$

where N_x and N_y are the total number of mesh lines parallel to the x-axis and y-axis respectively.

The continuous dependent variables from the discrete points can be used to

derive the nonlinear algebraic equations necessary to approximate the solutions of the partial differential equations. These solutions are discretized values at every mesh point in the domain for physical variables such as electrostatic potential ($\phi(x)$), and carrier concentrations n and p. The Poisson equation (4.50), for example, is repeated here in a simpler form:

$$\nabla \cdot \epsilon \nabla \phi = -q \left(N_D^+ - n + p - N_A^- \right), \tag{5.5}$$

which can be discretized as follows

$$\left(\frac{\phi_{i+1,j} - \phi_{i,j}}{h_i} \Delta k + \frac{\phi_{i,j+1} - \phi_{i,j}}{k_j} \Delta h + \frac{\phi_{i-1,j} - \phi_{i,j}}{h_{i-1}} \Delta k + \frac{\phi_{i,j-1} - \phi_{i,j}}{k_{j-1}} \Delta h \right)$$

$$= -\frac{q}{\epsilon_0 \epsilon_r} \left(N_{D_{i,j}}^+ - n_{i,j} + p_{i,j} - N_{A_{i,j}}^- + n_{s_{i,j}} \right) \cdot \Delta k \Delta h \tag{5.6}$$

This discretization of the Poisson equation shows that the potential at a mesh point, in the control box of length $\Delta h = (h_i + h_{i-1})/2$ and $\Delta k = (k_j + k_{j-1})/2$, depends on the potential and charge at the mesh point, and at the four neighboring mesh points. The current continuity equations, (4.58) and (4.59), for electrons or holes can be discretized in the form of 5.7 on a uniform 2-D grid with mesh size Δ.

$$\frac{n(i,j,k+1) - n(i,j,k)}{\Delta t} = \frac{J^x(i+1/2,j,k) - J^x(i-1/2,j,k)}{q\Delta}$$

$$+ \frac{J^y(i,j+1/2,k) - J^y(i,j-1/2,k)}{q\Delta} \tag{5.7}$$

Material properties, such as the Debye length, and the dielectric relaxation time, must be taken into account when equations are discretized through the finite difference scheme. The Debye length defines the space decay constant for excess carrier distribution which decays in space (by carrier diffusion) to the bulk concentration [148]. The mesh size, therefore, must be smaller than the Debye length given

by

$$L_D = \sqrt{\frac{\epsilon k_B T}{q^2 N_D}}. \tag{5.8}$$

The field produced by charge carriers causes them to fluctuate. The simulation time step is limited by the decay time (dielectric relaxation time) for these fluctuations given by

$$t_{dr} = \frac{\epsilon}{q N_D \mu}. \tag{5.9}$$

For GaAs, at a typical doping density, $N_D \approx 10^{18} \text{cm}^{-3}$, and mobility $\mu(N_D) \approx 6000 \text{cm}^2/\text{V-s}$, the Debye length is approximately 5 nm, and t_{dr} is approximately 10^{-15}s.

5.3   The Newton-Raphson Method

Newton's method is an iterative technique suitable for the solution of the discretized set of simultaneous equations formed by the finite difference method. Newton's method is based on a linear approximation of the function $f(x)$, using a tangent to the function curve, as illustrated in Figure 5.4 [169].

The initial point x_1, guessed close to the root, is used to determine the next point x_2 using the tangential angle θ relationship as follows

$$x_2 = x_1 - \frac{f(x_1)}{f'(x_1)} \tag{5.10}$$

with the general form

$$x_{k+1} = M(x) = x_k - \frac{f(x_k)}{f'(x_k)} \qquad k = 1, 2, 3, ... \tag{5.11}$$

The method is quadratically convergent if $|M'(x)| < 1$ on an interval about the root
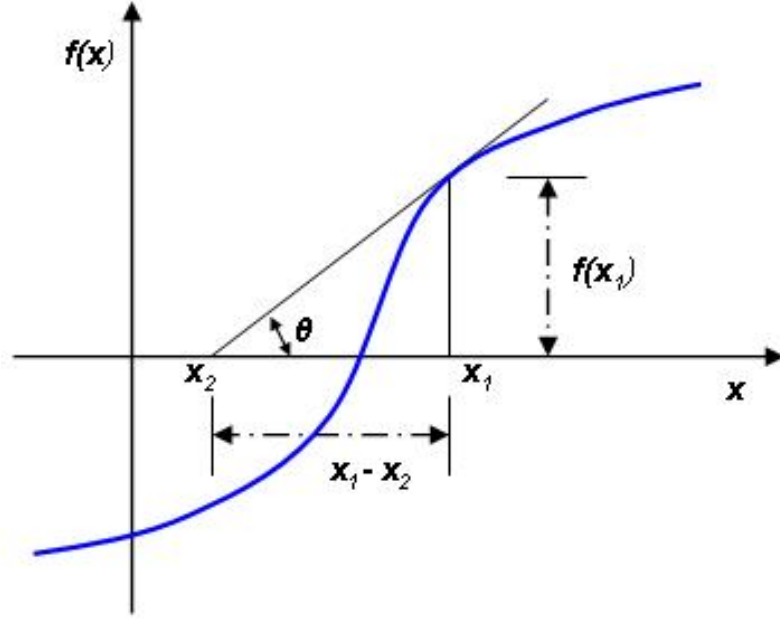
Figure 5.4: Illustration of the Newton method.

r, and converges when

$$\lim_{k \to \infty} \|x_{k+1} - x_k\| = 0 \tag{5.12}$$

or

$$\lim_{k \to \infty} f(x_k) = 0 \tag{5.13}$$

When Newton's method is applied to the discretized Poisson equation (5.6), the equation assumes the matrix form

$$[A][\phi] = [B(\phi)], \tag{5.14}$$

where the matrix $[A]$ is the coefficient matrix, and $[B(\phi)]$ contains the terms in the right hand of (5.6). This equation shows the non-linear dependence of the charge density $\rho(\phi) = q \left[N_D^+(\phi) - n(\phi) + p(\phi) - N_A^-(\phi) \right]$ on the electrostatic potential ϕ in the Poisson equation (5.5). For the solution using the Newton-Raphson algorithm,

The Poisson equation takes the form

$$f(\phi) = \nabla \cdot \epsilon \nabla \phi + \rho(\phi) = 0, \tag{5.15}$$

where Newton's iterations converge to the solution ϕ of the function $f(\phi) \equiv f(x_k)$ in (5.11). For local convergence, the solution of (5.15) can be expressed as

$$\psi_{k+1}(\lambda) = \psi_k - \lambda \frac{f(\phi_k)}{(J_\phi f)(\phi_k)}, \tag{5.16}$$

where λ is the step length in the direction of the steepest descent $f(\phi_k)/(J_\phi f)(\phi_k)$, and J_ϕ is the Jacobian matrix [149, 153, 168].

5.4 The Predictor-Corrector Method

The predictor-corrector method is based on a multistep scheme. The solution of a function y is first estimated with a local truncation error, then improved with a correction term. An algorithm such as the Euler method [169], written as

$$y_{k+1} = y_k + hy'_k + O(h^2) \tag{5.17}$$

can be improved to

$$y_{k+1} = y_k + h\frac{y'_k + y'_{k+1}}{2} \tag{5.18}$$

which requires that y'_{k+1} be known. The simple Euler method (5.17), the "predictor", can be used to predict a value of y_{k+1}. y_{k+1} is then used to compute y'_{k+1}, which in turn improves the estimated y_{k+1} in the improved Euler method (5.18), the "corrector".

The implementation of the predictor-corrector method on the coupled Schrödinger-Poisson equations is outlined here, and a detailed discussion is found elsewhere

[149,170]. The solution, ϕ, presented in section 5.3 above for the non-linear Poisson equation (5.5), depends on the charge density

$$\rho(\phi) = q \left[N_D^+(\phi) - n(\phi) + p(\phi) - N_A^-(\phi) \right] \tag{5.19}$$

In the equilibrium situation, the charge densities $n(\phi)$, and $p(\phi)$, are obtained from equations (4.33), and (4.35) respectively, given here with their electrostatic potential-dependent predictors.

$$n(\phi) = N_C \, exp\left(\frac{E_f - E_c + q(\phi_k - \phi_{k-1})}{kT} \right) \tag{5.20}$$

$$p(\phi) = N_V \, exp\left(\frac{E_v - E_f - q(\phi_k - \phi_{k-1})}{kT} \right) \tag{5.21}$$

where ϕ_{k-1} is the electrostatic potential from the previous step. The self-consistent solution of the charge densities depends on the energies and wave functions from the solution of the Schrödinger equation (4.2), repeated here as

$$H\psi_n(r) = E_n\psi_n(r). \tag{5.22}$$

The solution eigenfunctions ψ_n for this equation depend on the elecrostatic potential ϕ from the Poisson equation:

$$\nabla \cdot \epsilon \nabla \phi + \rho(\phi) = \left[N_D^+(\phi) - n(\phi) + p(\phi) - N_A^-(\phi) \right] \tag{5.23}$$

The predictor-corrector method can then be used to find the solution to this coupled system of Schrödinger-Poisson equations. In the implementation, the quantum densities $n(\phi)$, and $p(\phi)$ are used as predictors for the Poisson equation. A new potential ϕ is determined and used in the Schrödinger equation to calculate a new set of eigenfunctions and eigenenergies. This system of iterations continues until a

specified maximum number of iterations is met, or stabilization occurs at a specified residual $R(n) = \|n_{k+1} - n_k\| \le \epsilon_{res}$.

In the non-equilibrium situation, the solution to be determined is that of a coupled Schrödinger, current, and Poisson equations. The drift-diffusion current equations (4.58) and (4.59) (determined in section 4.2.2) become coupled to the Poisson equation through the quasi Fermi energies which determine the charge densities. The charge densities used in this case are those for a non-equilibrium situation described in section 4.2.1.2, and obtained from equation (4.44) and (4.46) respectively. These charge densities with their electrostatic potential-dependent predictors, are expressed as

$$n(\phi) = N_C F_{1/2} \left(\frac{E_f - E_c + q(\phi_k - \phi_{k-1})}{kT} \right), \qquad (5.24)$$

and

$$p(\phi) = N_C F_{1/2} \left(\frac{E_v - E_f - q(\phi_k - \phi_{k-1})}{kT} \right). \qquad (5.25)$$

The current equations are also coupled to the Schrödinger equation through the eigenstates and eigenenergies.

This inclusion of the current equations limits the used of the predictor-corrector method, and calls for other iterative schemes. One approach described in [168, 170] involves alternating the solutions of the Schrödinger-Poisson equations solved by the predictor-corrector method, with the fixed quasi Fermi levels $E_{F,n}$, or $E_{F,p}$ and the current equations with fixed eigenpairs $\{\psi_i, E_i\}$. An underrelaxation approach is used for the quasi Fermi energies, with an adaptively-determined relaxation parameter ω_k.

Chapter 6

Device Simulation and Results

Performance optimization is essential in semiconductor device manufacturing. Device simulation reduces the costs involved in manufacturing and testing for performance enhancement. Detailed behavior of general device structures with different geometries and doping profiles can be simulated and analyzed within hours. Processing methods and parameters can be altered giving insight into how they affect the semiconductor device and performance. In this study, we use a semiconductor device equation solver (NextNano) to simulate a GaAs FET-based biosensor device governed by the semiconductor equations presented earlier. The geometry and material properties of the device are specified in an input text file. This input file is also used to specify the computations to be done, the numerical techniques to be applied, and the output setup and formats. In this manner, we hope to learn the effects of molecular interactions at the device surface.

6.1   Device Setup

We simulate a two dimensional (2D) physical model of the GaAs biosensor device. The 2D device model gives a comprehensive and accurate representation of the device's physical and electrical properties. The model takes into account the active region with appropriate boundary conditions for contacts and surfaces, computing the equilibrium and non-equilibrium transport equations. The device is grown on a semi-insulating GaAs substrate.

GaAs field effect devices are unipolar, reducing the semiconductor equations to ones describing electron transport only. Therefore, we neglect the minority carriers

and assume negligible generation and recombination effects. For an isolated device, both the boundaries inside the semiconductor bulk and the current free surfaces are modeled with zero-valued derivatives normal to the boundary for both potential and carrier density. The source and drain ohmic contacts are assumed to be ideal with pre-specified fixed potential and fixed carrier concentrations imposed as boundary conditions. The source potential is set to zero, and a varying potential is applied to the drain contact to derive the current as a function of drain-to-source voltage V_{DS}. The gate region potential is controlled by the surface charge, or by charge effects associated with the addition of DNA biomolecules. The semi-insulating substrate is assumed to have a negligible effect on the drain-source current. The 2D FET biosensor device is illustrated in Figure 6.1.
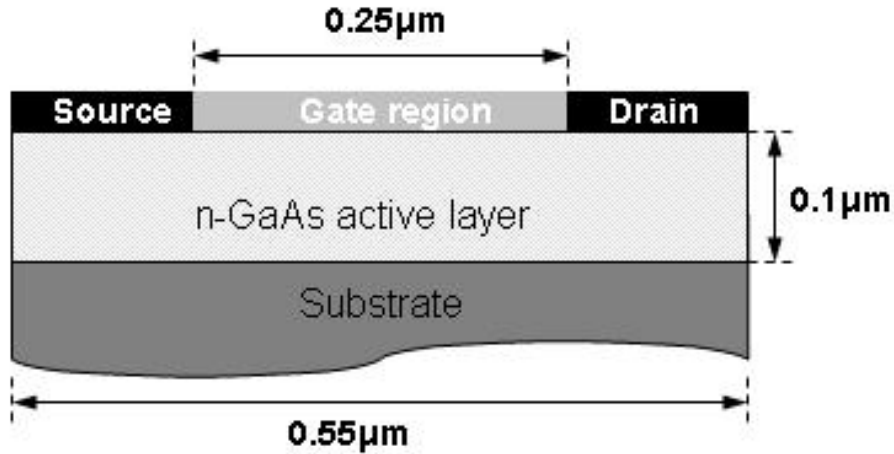
Figure 6.1: The 2D FET biosensor device geometry used in simulation.

The geometry of the device is defined by the basic and essential parameters which determine the performance and current-voltage relationship. These parameters include gate length (L_g), gate width (W_g), and active channel thickness (A). The device used in this study, and shown in Figure 6.1, has an active n-doped GaAs layer of thickness $A = 0.1\,\mu\text{m}$, and a gate region length $L_g = 0.25\,\mu\text{m}$ for the 2D simulation. For an actual device in three dimensions, the cross-section of the 2D device shown in Figure 6.1 is projected along the device width. The device width

(W_g), for typical GaAs FET devices ranges from 2 to 3 orders of magnitude higher than the gate length [6, 74].

The n-GaAs active channel is assumed to have a constant doping profile with doping density $N_D = 0.15 \times 10^{18} \text{cm}^{-3}$ of n-type impurities, with full ionization of electrons from the donors. The material properties for the GaAs zincblende structure, such as the conduction band and valence band effective masses discussed in section 4.1.3 are taken from Vurgaftman et al. [141]. The GaAs lattice constant $a = 0.5653$ nm, and the static dielectric constant is taken to be $\epsilon_r = 12.93$. The lattice temperature is set to 300 K and assumed constant over the entire device. The device performance depends on temperature, and various characteristic relationships have been defined for temperature-dependent parameters. Some of the parameters that depend on temperature include the lattice constant, band gap energy (4.14), carrier mobility (4.61), device saturation velocity (4.63), and peak electric field (4.65). These parameters have a direct effect on the device carrier transport equations, hence on the performance of the device.

The solution of the coupled system of semiconductor equations requires discretization of the physical device. The discretization results in a mesh scheme that ensures that enough nodes are included for convergence of the solution. At areas near the boundaries, or areas where physical properties change rapidly, it is essential to have more nodes to accurately model device behavior. We have defined meshes of size 5.0 x 1.0 nm in most of the device and 2.5 x 1.0 nm near the source and drain junctions, and near the ends of the gate region. The mesh sizes are smaller than the Debye length, $L_D = 11.1$ nm at $N_D = 0.15 \times 10^{18} \text{cm}^{-3}$ (5.8), as required for spatial decay of carrier distribution due to diffusion.

Table 6.1 summarizes the parameters used for the GaAs biosensor device simulation.

Parameter		value
Gate region length	L_g	$= 0.25 \ \mu m$
Active channel thickness	A	$= 0.1 \ \mu m$
Doping density	N_D	$= 0.15 \text{x} 10^{18} \text{cm}^{-3}$
Temperature	T	$= 300$ K
Dielectric constant	ϵ_r	$= 12.93$
Lattice constant	a	$= 0.5653$ nm
Peak electric field	E^{pk}	$= 3.2$ KV/cm
Saturation velocity	v_s	$= 1.2 \text{x} 10^7 \text{cm/s}$

Table 6.1: Device parameters for the GaAs FET device.

6.2 Simulation Flow

Program execution depends on the device specifications in the input file and the material properties defined in the database, as shown in Figure 6.2. The calculation
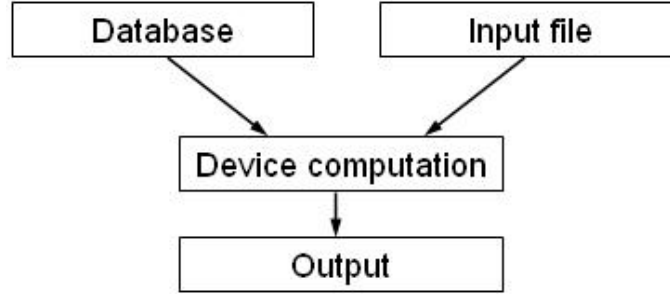
Figure 6.2: Program interaction with the input file and material properties in the database.

flow for solving the coupled Schrödinger, Poisson and current equations is shown in Figure 6.3. All constants and data which remain invariant during the iterative solving of the coupled equations are calculated and set up in the initialization stage. This stage also includes preparation and conversion of all semiconductor and GaAs material-specific parameters needed and found in the input file or the database, and the evaluation of the bulk band structures. The electronic band structure is calculated within the effective mass approximation, using the envelope wave approximation discussed in section 5.1.

The nonlinear Poisson equation is used to calculate the built-in potential classi-
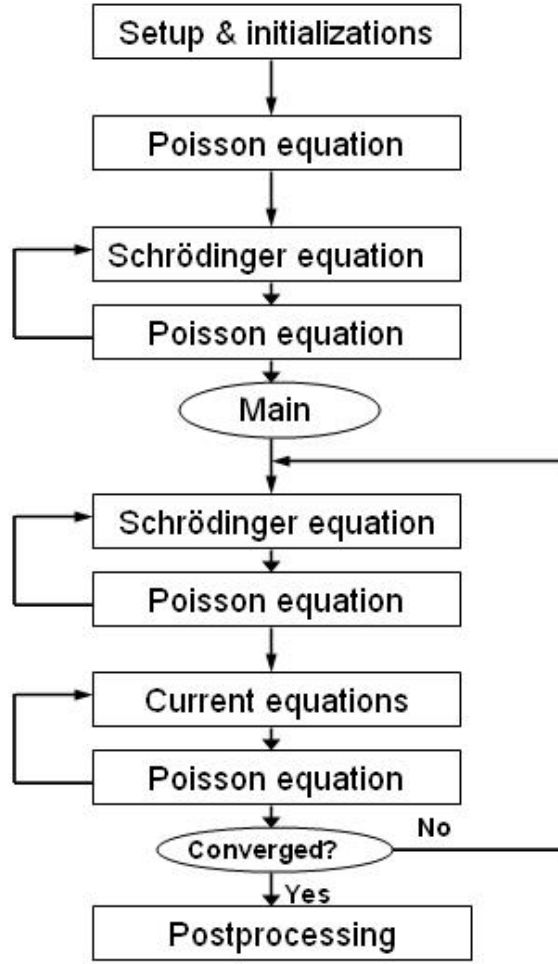
Figure 6.3: Computational flow for device simulation.

cally for the equilibrium conditions. The Fermi level is set to 0 eV, and an initial guess for the electrostatic potential is calculated. Newton's method is used for the solution of the Poisson equation with Neumann boundary conditions for zero electric field. The intrinsic density is calculated using the built-in potential. For quantum mechanical effects, the built-in potential is also calculated quantum mechanically using the classical built-in potential as an initial guess for the electrostatic potential. The coupled nonlinear Schrödinger-Poisson equation is applied and iterated to a solution using the predictor-corrector algorithm. In the iterations, the Poisson equation is solved for the electrostatic potential using a predicted value for the charge density. The electrostatic potential is used in the Schrödinger equation,

with the corrected value for the charge density to solve for the eigenstates ψ_i, and eigenenergies E_i, in turn used by the Poisson equation. The iterations continue until convergence of the electron density, or until a specified maximum number of iterations is exceeded.

For the nonequilibrium conditions, an electric field is applied across the contacts by applying a bias potential V_{DS} across the drain and source contacts. Therefore, we include the current equations defined by the drift-diffusion model described in section 4.2.2. In this model, we only consider electrons as the charge-carriers, and ignore any carrier generation or recombination. The carrier mobility is modeled with a dependence on the lattice temperature (according to (4.61)), doping density (4.60), and electric field (4.64).

With the inclusion of the current equations, the quantum mechanical solution of the coupled system of Schrödinger, Poisson, and current equations is solved self-consistently. For the quasi-Fermi level, Dirichlet boundary conditions are applied for the ohmic contacts and for the gate region. The surface charge density in the gate region also results in band bending, and a barrier potential ϕ_B exists between the Fermi level and the conduction band energy E_C. Dirichlet boundary conditions are applied for the electrostatic potential at the interface. The coupled system of Schrödinger and Poisson equations is iterated using the predictor-corrector algorithm described earlier. The coupled current-Poisson equation is solved using Newton's method to determine the quasi-Fermi levels and the electrostatic potential used in the Hamiltonian for the Schrödinger equation. The current equation is solved with underrelaxed Fermi energies that determine charge density for the Poisson equation.

In the postprocessing step, solutions of the electrostatic potential, quasi-Fermi levels, and charge densities obtained from the self-consistent solution of the Schrödinger, Poisson, and current equations are used in further calculations to determine any

other desired quantities, such as current density, band structures, and current-voltage relationships (I-V curves). If a voltage sweep is applied to the contacts for the purpose of obtaining I-V curves, the self-consistent solutions of the Schrödinger, Poisson, and current equations determined as shown in Figure 6.3 must be repeated for each voltage step.

6.3 Simulation Results and Device Modeling

This section presents simulation results of a GaAs field-effect DNA biosensor. To understand the performance of the GaAs transistor-based DNA sensor, we first look at the electronic band structure and the changes associated with molecular immobilization and hybridization of complementary DNA biomolecules. DC current-voltage relationships are simulated, investigating the effect of DNA charge on the electrical behavior of the device. Small-signal parameters of the biosensor device are derived from incremental perturbations of the DC measurements. These parameters are then used to analyze the small signal AC response of the device for potential application at high frequencies where $1/f$ noise decreases. For the AC response, we consider only the intrinsic device parameters at a given bias point. An extensive study of device behavior at high frequencies (in the microwave and millimeter wave range of the electromagnetic spectrum) is beyond the scope of this dissertation, and is left for future research.

6.3.1 Electronic Band Structure

The electronic band energies are first calculated and presented in Table 6.2. These energy values are based on the Varshni equation given in (4.14), and the parameters in Table 4.1. The band gap energy, 1.422 eV, is the difference between the Γ conduction band energy and the heavy-hole valence band energy. Table 6.3 shows

Electronic band	Energy [eV]
Γ	0.6
L	0.885
X	1.077
Heavy-hole	-0.82233
Light-hole	-0.82233
Split-off	-1.16333

Table 6.2: Electronic band energies at 300 K, relative to the Fermi energy $E_F = 0.0$ eV.

the calculated effective density of states for the conduction and valence bands. The density of states directly affects the carrier concentration n for both the equilibrium and nonequilibrium conditions according to (4.33) and (4.44) respectively.

Effective density of states	Value [1×10^{18} cm^{-3}]
$N_C(\Gamma)$	0.4352
$N_C(L)$	10.4323
$N_C(X)$	19.7421
N_V(Heavy-hole)	8.8721
N_V(Light-hole)	0.445
N_V(Split-off)	1.7901

Table 6.3: Effective density of states for conduction and valence bands at 300 K.

The potential distribution across the active channel region for a pure surface charge at equilibrium conditions is shown in Figure 6.4. This figure shows that, at zero bias potential ($V_{DS} = 0$ V) there is a built-in potential energy of -0.576 eV associated with the surface charge over the gate region. This potential is uniform from the source contact to the drain contact and decays with depth from the gate region interface to the semiconductor bulk. In nonequilibrium conditions (Figure 6.5), an applied bias voltage $V_{DS} = 0.6$ V creates a high-field region at the drain side. The current channel is modulated, under both equilibrium and nonequilibrium conditions, by the depletion region resulting from the surface charge. Changes in the surface charge resulting from immobilization of ssDNA and hybridization by

complementary strands results in a change in V_{sbi}. This change in V_{sbi}, using the pure surface charge case as a reference, is illustrated in Figure 6.6. V_{sbi} increases by 2.54 mV after immobilization of a 20-mer ssDNA, and by 5.08 mV after DNA hybridization with a completely complementary strand. The change in potential that results from the immobilization of DNA molecules also decreases with depth, from the interface to the semiconductor bulk.
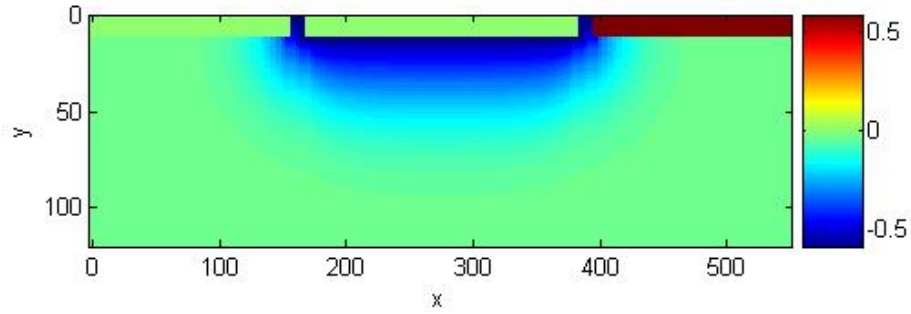
Figure 6.4: Potential energy [eV] across the active channel layer in equilibrium conditions.
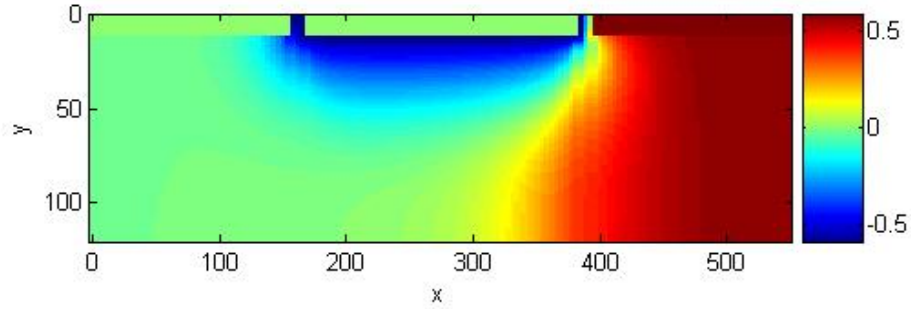
Figure 6.5: Potential energy [eV] across the active channel layer with an applied $V_{DS} = 0.6$ V.

The charge distribution in the biosensor modulates the conductance of the channel from drain to source. Figure 6.7 shows the internal space charge density, with the depletion layer characterized by a decrease in carrier concentration at the boundary. The space charge is created by positive charge in the semiconductor, which compensates for negative surface charge resulting from DNA immobilization, maintaining charge neutrality. The change in charge density under the gate region (near the
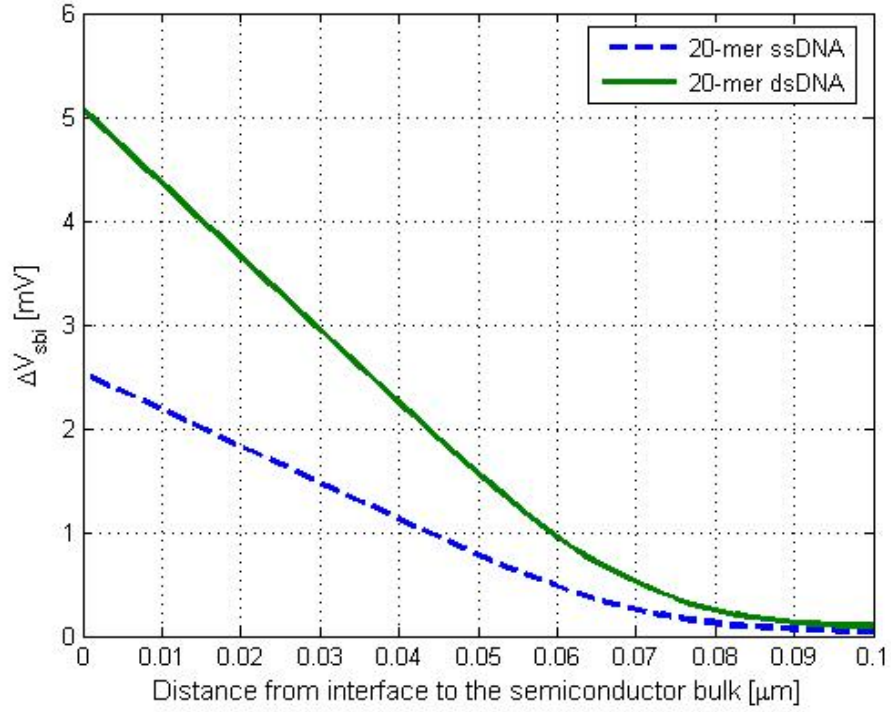
Figure 6.6: Plot of ΔV_{sbi}, the change in V_{sbi} associated with DNA immobilization and hybridization, relative to a pure surface charge.

drain end) is characterized by high electric fields, yielding a drift velocity which rises to a peak according to Figure 4.7, and falls to an equilibrium value at saturation. This velocity-field relationship results in nearly equal charges in the depletion layer and in the conducting channel.
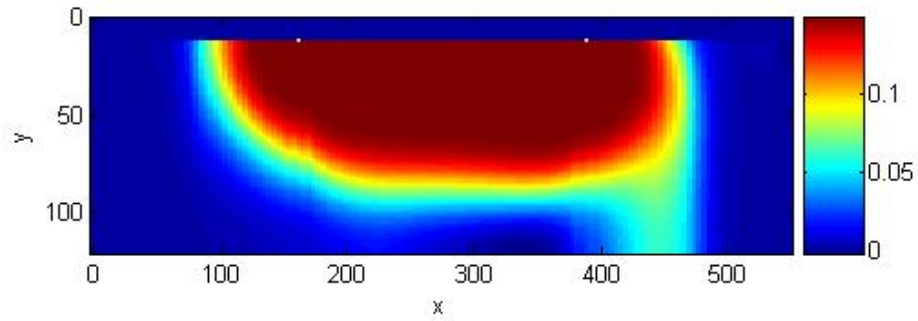
Figure 6.7: Space charge density [x10^{18} e/cm^3] across the active region with $V_{DS} = 0.6$ V.

6.3.2 Device I-V Curves

The current-voltage relationship predicted by our model was compared against experimental results of Baek, et al., [5] for similar device dimensions, with $V_{sbi} = 0.576$V and $N_D = 0.15\text{x}10^{18}\text{cm}^{-3}$. Figure 6.8 shows that the results of our simulation are in relative qualitative and quantitative agreement with Baek's results. One distinction is that our model assumes zero ohmic contact resistance, while Baek's device portrays an infinite (ideal) output resistance R_{ds}, shown by the constant output current in saturation.
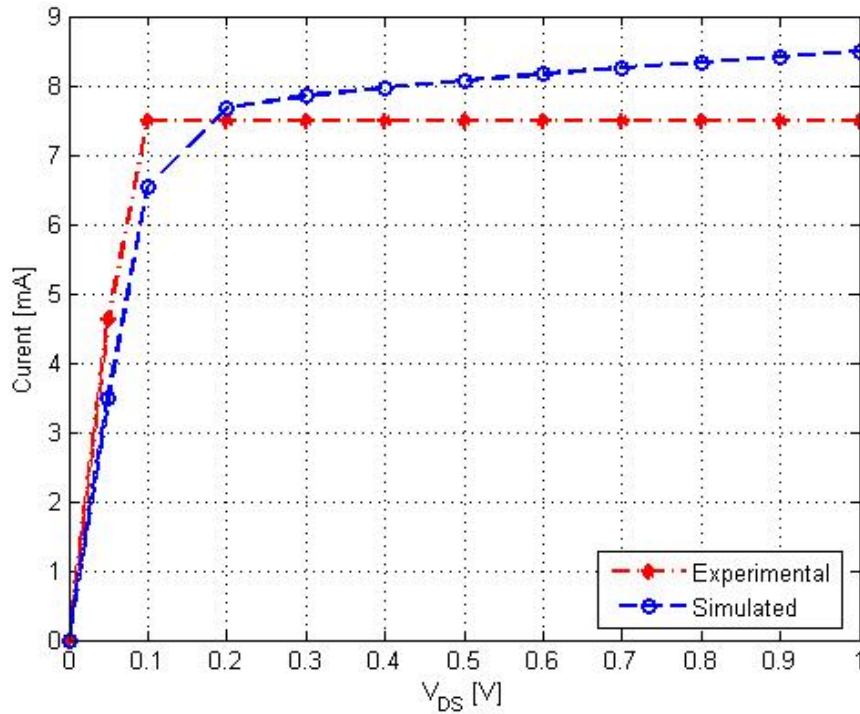
Figure 6.8: I-V curves from surface charges comparing our simulated results and the experimental results from Baek et. al. [5] for a 100 μm wide device.

Immobilization and hybridization of DNA molecules results in a change in the charge density at the gate region. This change in charge modulates the depletion layer and the channel current which flows under the gate region. This change in channel dimensions is illustrated by the respective change in current density within the channel as shown in Figure 6.9. As shown in this figure, the simulation predicts a

decrease in current after immobilization of ssDNA molecules, and a further decrease after their hybridization with complementary strands. The actual change in current density with respect to the pure surface charge case is shown in Figure 6.10. There is a decrease in current density of about 0.45 A/m after immobilization, resulting from an increase in net charge density over the gate region, associated with an increase in depletion depth. The increase in the depletion depth within the active region reduces the channel conducting area, hence a decrease in current density. Hybridization results in a further increase in charge density and a further decrease in current density (0.9 A/m with respect to pure surface charge), as expected.
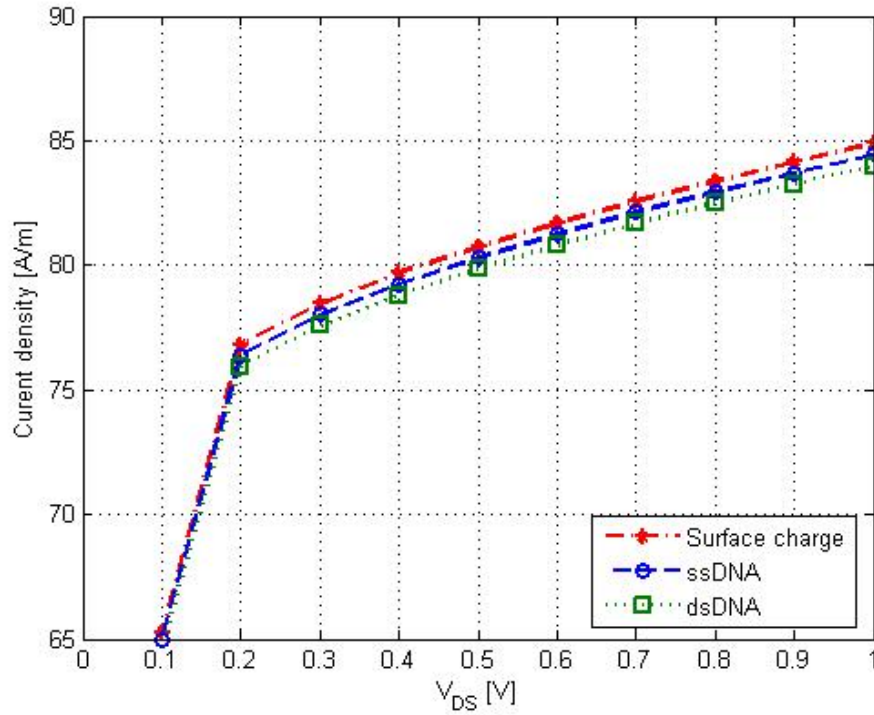
Figure 6.9: I-V Curves for the biosensor device before immobilization of ssDNA, after immobilization, and after hybridization event.

The effect of DNA oligonucleotide length on current density is of great interest, and was also simulated. Longer oligonucleotides ($L_{dna} > 20$ mers) will have additional negative charge along the DNA molecule that is situated further from the surface. Shorter molecules ($L_{dna} < 20$ mers) will have fewer negative charges. We
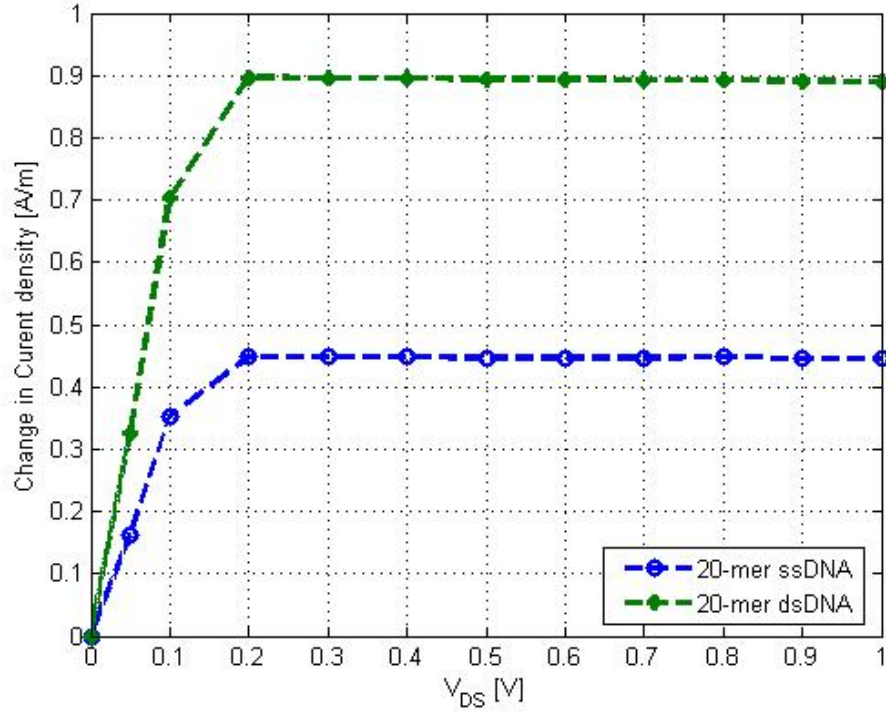
Figure 6.10: Change in current density associated with DNA immobilization and hybridization, relative to pure surface charge.

investigated shorter DNA oligonucleotides (L_{dna} = 12 mers), and longer oligonucleotides (L_{dna} = 28 mers), comparing them against the initial (L_{dna} = 20 mers) oligonucleotides. Figure 6.11 shows the resulting I-V curves for the immobilization of various ssDNA lengths, compared to a pure surface charge. The changes involved are small, but a magnified view at the V_{DS} = 0.6 V bias point is shown in Figure 6.12, providing an insight into the magnitude of the effect. All DNA lengths in the figure exhibit an average decrease in current density of $\approx$ 0.45 A/m with respect to that of the pure surface charge current density. The insert in Figure 6.12 shows that the longer the DNA length, the greater the decrease in current density. However, this decrease in current density is small and decays with increasing DNA lengths. The decay results from a decreasing effect of DNA molecular charge at an increasing distance R from the surface. The decrease is proportional to $1/R^2$, which results in a small net electric field at the surface, shown in Figure 3.8.
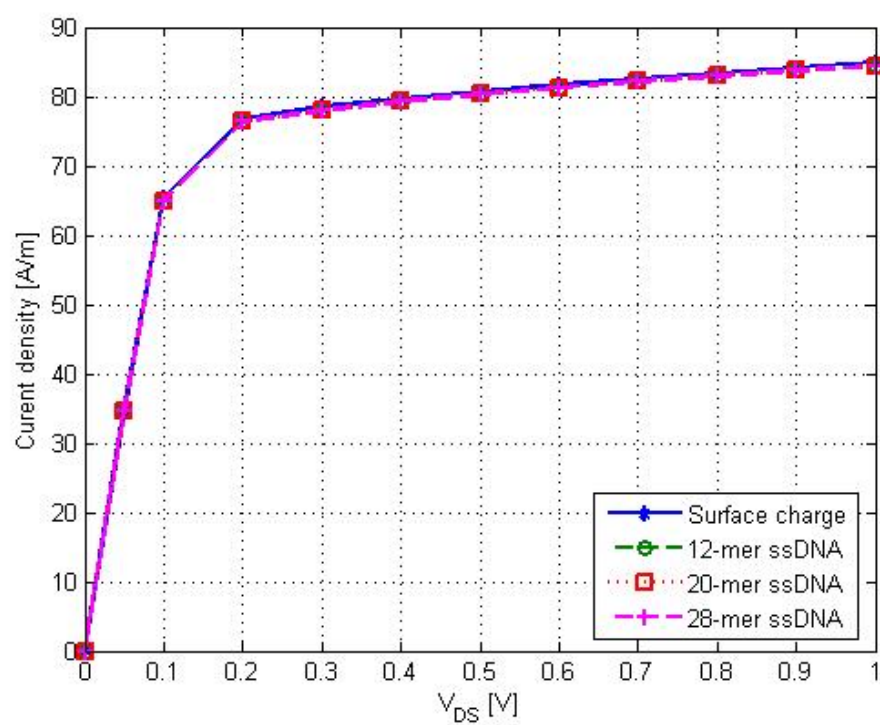
Figure 6.11: The effect of DNA oligomer length on the conducting channel, illustrated by changes in the I-V curves.
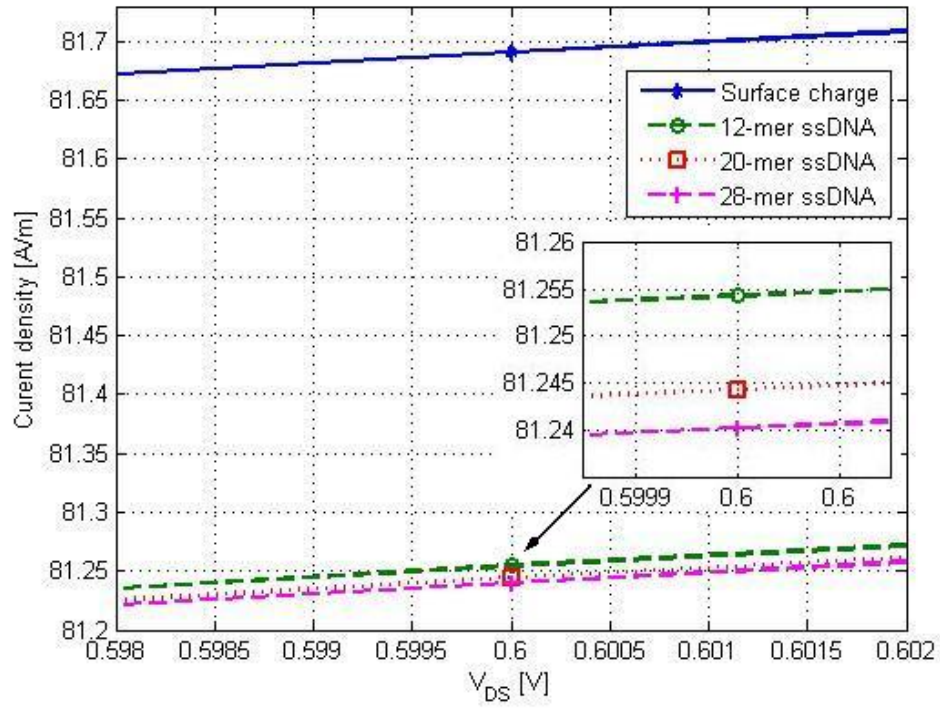
Figure 6.12: The effect of DNA oligomer length (manifested by molecular charge) illustrated at a bias point $V_{DS} = 0.6$ V.

6.3.3   Small Signal Analysis

Using the DC current-voltage relationships and the charge density behavior predicted by the simulation, we can obtain the intrinsic AC small-signal parameters discussed in Section 2.2. Using these parameters, we can predict the AC response of the device. We will only consider the small-signal values at a single bias point, since most transistor devices are typically characterized and modeled at high frequencies by impedance (S-parameter) measurements at a single bias voltage and current. The small-signal values at the bias point will also be sufficient to illustrate the performance of the small-signal equivalent circuit of Figure 2.7. We select the bias point $V_{DS} = 0.6$ V, with current $I_{DS} = 8.17$ mA for a typical 100 μm wide device, based on the I-V characteristics (Figure 6.8) of our simulated device.

Some important AC small-signal parameters which can be derived from our simulated results are the output conductance of the device, the transconductance of the active channel, and the capacitances resulting from the charge density under the gate region. Figure 6.13 shows the output conductance g_{ds}, and Figure 6.14 shows the resulting output resistance $R_{ds} = 1/g_{ds}$ obtained from (2.14). The value of g_{ds} decreases with increasing V_{DS} and becomes nearly constant at the onset of saturation. R_{ds} behaves inversely to g_{ds}. Figure 6.15 illustrates the transconductance g_m of the active channel with increasing V_{DS}. The transconductance increases at low bias voltages and stabilizes in the saturation region.

The capacitances C_{gs}, C_{gd}, and C_{ds} are voltage-dependent, according to equations (2.15), (2.16), and (2.17), respectively. C_{gs} decreases with increase in V_{GS} when V_{GD} is held constant. C_{gd} decreases as V_{DS} is increased, while C_{ds} increases with increasing V_{DS}. From these results, we can calculate the so-called transition frequency f_T (2.18), the maximum frequency of oscillation, f_{max} (2.19), the carrier transit time τ (2.21), and the charging resistance R_i (2.22). At the bias point $V_{DS} = 0.6$ V and $I_{DS} = 8.17$ mA, these parameter values were calculated and are
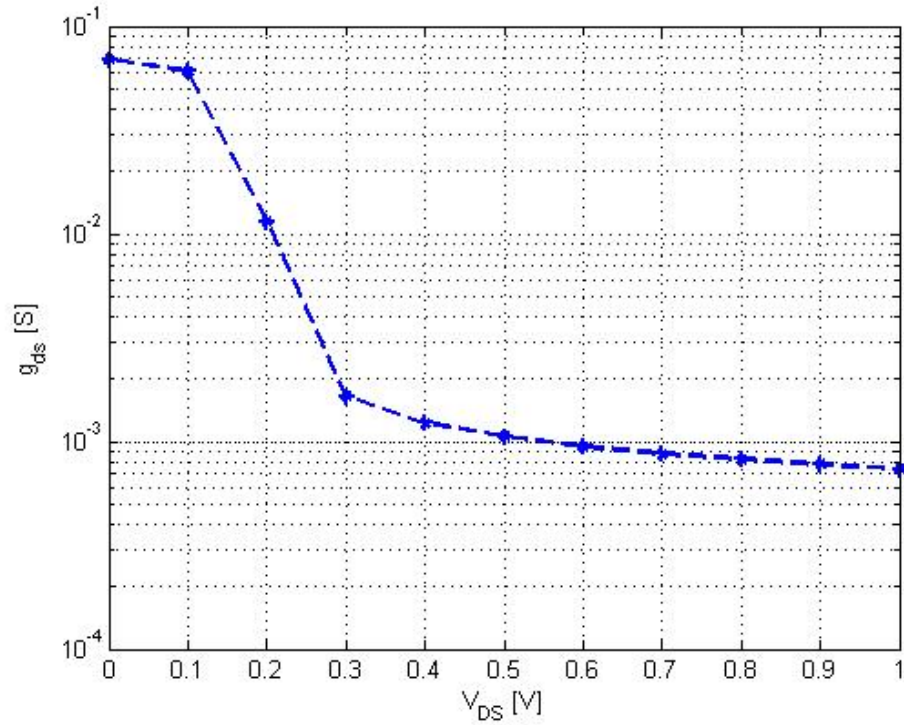
Figure 6.13: Output conductance as a function of V_{DS}.

shown in Table 6.4.

Parameter	Value	
g_{ds}	0.943	mS
g_m	17.6	mS
R_{ds}	1060	Ω
C_{gs}	0.0378	pF
C_{gd}	0.0364	pF
C_{ds}	0.4163	fF
R_i	0.0963	Ω
f_T	37.77	GHz
f_{max}	355.0	GHz
τ	0.0208	ps

Table 6.4: Small signal parameter values at a bias voltage $V_{DS} = 0.6$ V and drain-to-source current $I_{DS} = 8.17$ mA for a 100 μm wide device.

The response of the impedance across the drain and source contacts is influenced by the modulation of the current channel and can be analyzed at different frequencies. The impedance (S-parameter) measurements were obtained for the small-signal
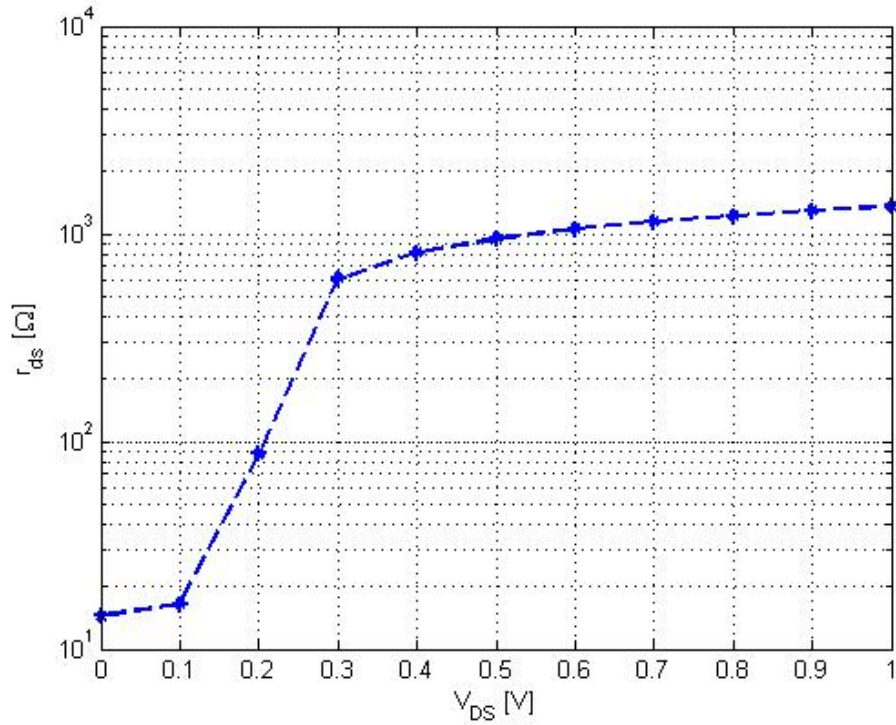
Figure 6.14: Output resistance as a function of V_{DS}.

equivalent circuit shown in Figure 6.16. The circuit was configured for one-port measurements with the parameter values in Table 6.4, and analyzed using the Qucs circuit simulator. Figure 6.17 shows the reflection coefficient S_{11}(magnitude and phase angle) of the device over the frequency range 0 Hz to 100 GHz, using a Smith chart presentation. The resulting output impedance of the device can be obtained from

$$Z_{out} = Z_0 \frac{1 + S_{11}}{1 - S_{11}} \qquad (6.1)$$

where $Z_0 = 50\ \Omega$ is the standard characteristic impedance used in the analysis, and S_{11} is a complex quantity in general. Figure 6.18 shows the magnitude of the output impedance of the device as a function of frequency. At low frequencies, $Z_{out} \approx 1060$ Ω, dominated by the value of the output resistance R_{ds} (Table 6.4) obtained from a DC analysis. As frequency increases, the device output resistance drops by (at least) an order of magnitude over the 100 GHz frequency range. Shifts in device
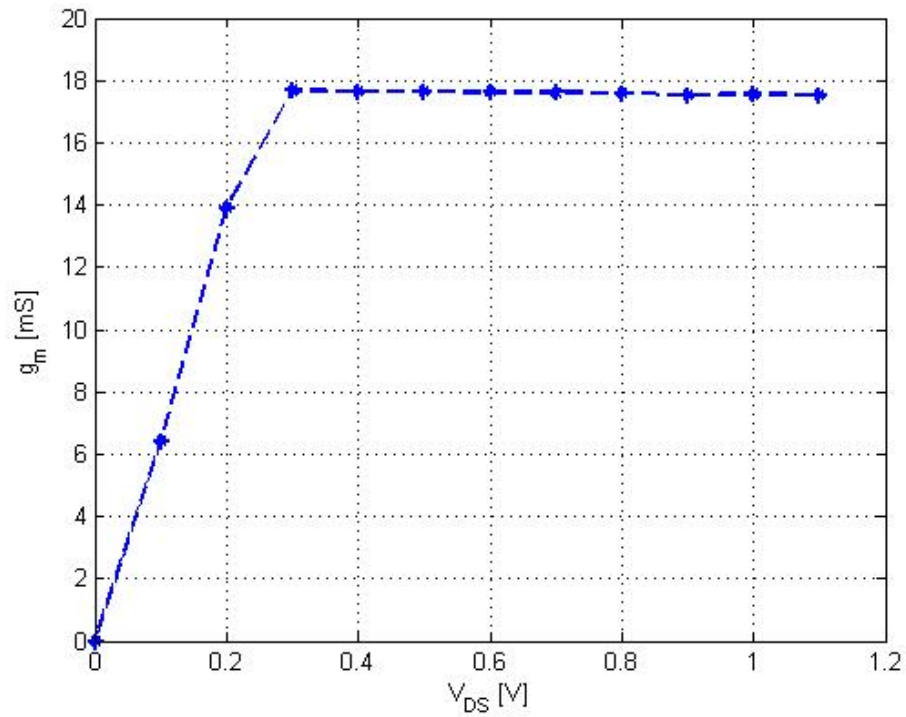
Figure 6.15: Transconductance of the device as a function of V_{DS}.
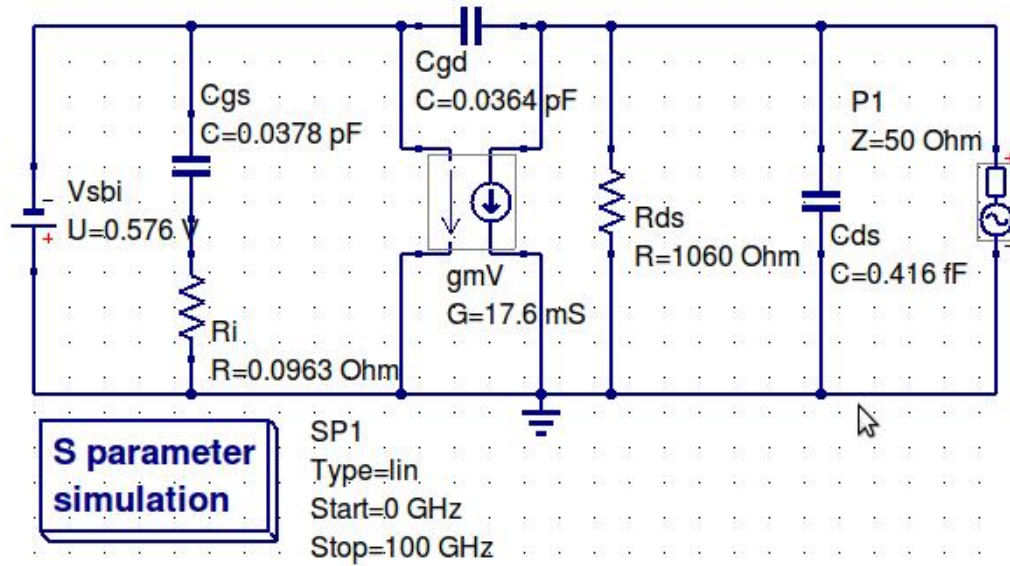
Figure 6.16: Intrinsic equivalent circuit for the GaAs biosensor device modeled for high-frequency analysis.

small-signal parameters such as transconductance and capacitance values are also similar as a function of frequency [74, 171]. Understanding the device behavior over
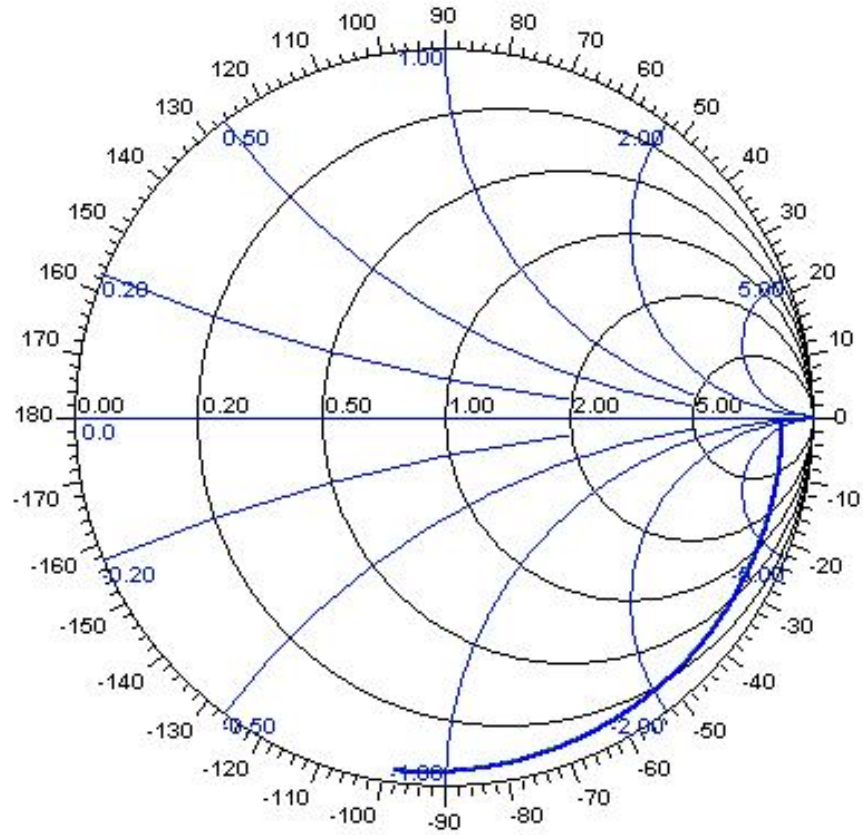
Figure 6.17: The reflection coefficient of the biosensor device as a function of frequency, using a Smith chart presentation. (Center point = 50 Ω normalization impedance.)

a wide frequency range is critical for the successful design of GaAs transistor-based biosensor devices, and allows one to optimize a transistor-based DNA detection device for highest sensitivity and specificity.
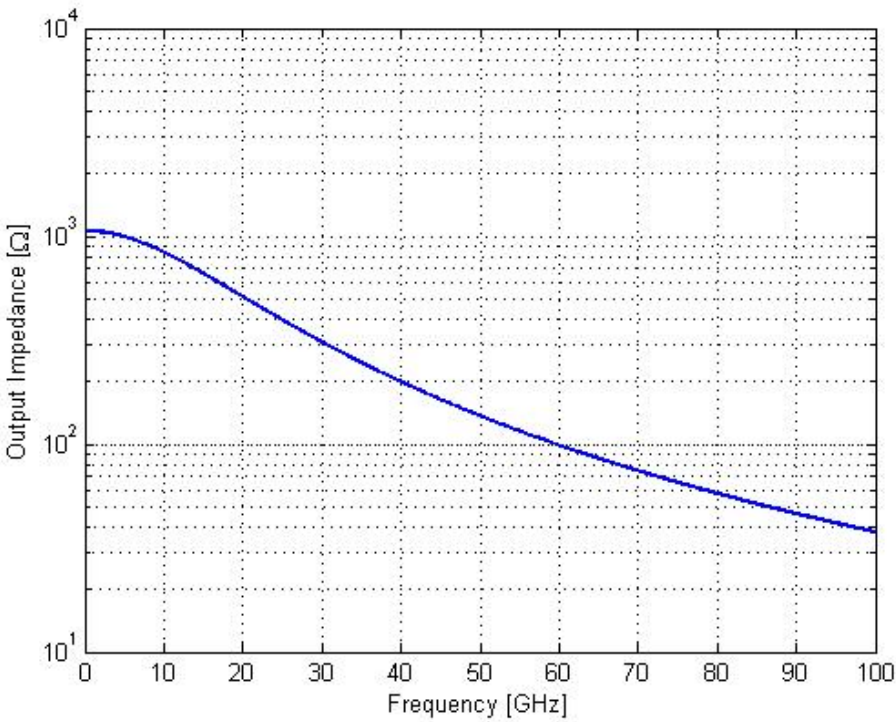
Figure 6.18: Output impedance as a function of frequency.

Chapter 7

Conclusion

A physical model for a GaAs FET-based DNA biosensor was developed and simulated. In this model, GaAs FET transistor physical properties were studied, and device transport equations modeled, incorporating the electrical charge effect from DNA biomolecules. A DNA charge model was developed assuming covalent tethering of DNA molecules to dangling bonds on the field-effect device surface. DNA charges on the surface have an effect nearly equal to that of the pre-existing surface charges; those charges on the molecule more distant from the surface have a decreasing electrostatic effect on sensor performance. This model also assumes that DNA molecules are, on average, oriented at an angle of 54° to the sensor surface, as predicted in the literature.

The electronic band structure of the device was studied (as influenced by DNA binding), and results show that there is an increase in surface built-in potential V_{sbi} by 2.54 mV after immobilization, increasing to 5.08 mV after hybridization of complementary DNA molecules. The increase in V_{sbi} results from an increase in net negative charge in proximity to the gate region, over and above that of contributions by the pre-existing surface charges. The effect of these changes in charge density at the gate region was also studied, specifically examining charges in the current-voltage relationships obtained. The I-V characteristics show a decrease in current density along the conducting channel by $\approx$0.45 A/m after immobilization, and $\approx$0.9 A/m following hybridization by complementary DNA strands. The decrease in current density was associated with an increase in negative charge density at the gate region, resulting in an increase in the depletion depth and a decrease in the effective area

of the conducting channel.

Potential applications of a GaAs biosensor device at high frequencies were then presented, based on extraction of the intrinsic small signal AC parameters from the DC measurements. The AC response was specifically analyzed at a single bias point, conveniently selected from the DC characteristics. The analysis shows that the output impedance of the device decreases with frequency, and good performance can be achieved up to the cut-off frequency of $f_T = 37.77$ GHz. The maximum frequency of oscillation is $f_{max} = 355$ GHz, suggesting that the device has the potential to be used at frequencies even higher than f_T, but the design of biosensor applications at these high frequencies may be hindered by the availability of testing and characterization equipment. An extensive study of higher frequency performance is left for future study. Such a research undertaking should include a noise analysis (which becomes important at high frequencies), as well as the effects of parasitic resistances, capacitances, and inductances, some induced perhaps by the biomolecules themselves.

The research presented in this dissertation provides a means for reliably characterizing and modeling a GaAs DNA biosensor device. The performance of the device can be improved by optimization of all physical and electrical device parameters involved, as well as accurate modeling of the device environment. In modeling a semiconductor field-effect device, an expanded study would also examine parasitic effects such as substrate effects, contact resistances, and fringing fields.

In a DNA sensing application, the complementary ssDNA molecules to be detected are presented in an ionic solution. The solution contains charged particles from other compounds or elements in solution, such as H_3O^+, OH^-, Na^+, or K^+. These ions may affect the charge distribution and the working pH conditions of the device, and an extensive analysis of these effects could be incorporated in the device model, based on an understanding of the changes in charge distribution involved as

well as interface parameters.

While research into devices based on GaAs and its alloys continues to expand, other compound semiconductors such as GaN, InP, and their alloys have also been investigated as platforms for biosensor design [172–178]. These materials are currently used in MESFETs and high electron mobility transistor (HEMTs) devices. GaN has shown great promise in high-frequency, high-power applications, and research study which includes applications in biosensing is ongoing. The DNA biosensor device model developed here can also be extended to GaN and other high-frequency compound semiconductor devices. These high-frequency devices can potentially result in improved sensitivity and specificity, which could in turn support the use of semiconductor-based molecular sensors for medical diagnosis.

Bibliography

[1] R. Williams, *Modern GaAs Processing Methods*. Norwood; Massachusetts: Artech House, 1990.

[2] C. Liechti, "Microwave field-effect transistors-1976," *Microwave Theory and Techniques, IEEE Transactions on*, vol. 24, no. 6, pp. 279 – 300, jun 1976.

[3] B. Alberts, D. Bray, K. Hopkin, A. Johnson, J. Lewis, M. Raff, K. Roberts, and P. Walter, *Essential Cell Biology*, 3rd ed. Garland Science, 2009.

[4] J. S. Blakemore, "Semiconducting and other major properties of gallium arsenide," *Journal of Applied Physics*, vol. 53, no. 10, pp. R123–R181, 1982.

[5] J. Baek, M. Shur, K. Lee, and T. Vu, "Current-voltage characteristics of ungated GaAs FET's," *Electron Devices, IEEE Transactions on*, vol. 32, no. 11, pp. 2426 – 2430, nov 1985.

[6] M. Shur, *GaAs Devices and Circuits*. Plenum Press, New York, 1987.

[7] G. D. Pitt and J. Lees, "Electrical properties of the GaAs X_{1C} minima at low electric fields from a high-pressure experiment," *Phys. Rev. B*, vol. 2, pp. 4144–4160, Nov 1970.

[8] Y. Yao, B. Yi, J. Xiao, and Z. Li, "Surface plasmon resonance biosensors and its application," in *Bioinformatics and Biomedical Engineering, 2007. ICBBE 2007. The 1st International Conference on*, july 2007, pp. 1043 –1046.

[9] R. L. Rich and D. G. Myszka, "Advances in surface plasmon resonance biosensor analysis," *Current Opinion in Biotechnology*, vol. 11, no. 1, pp. 54 – 61, 2000.

[10] E. Bakker and M. Telting-Diaz, "Electrochemical sensors," *Analytical Chemistry*, vol. 74, no. 12, pp. 2781–2800, 2002.

[11] E. Bakker and Y. Qin, "Electrochemical sensors," *Analytical Chemistry*, vol. 78, no. 12, pp. 3965–3984, 2006.

[12] J. Ngeh-Ngwainbi, A. A. Suleiman, and G. G. Guilbault, "Piezoelectric crystal biosensors," *Biosensors and Bioelectronics*, vol. 5, no. 1, pp. 13 – 26, 1990.

[13] R. L. Bunde, E. J. Jarvi, and J. J. Rosentreter, "Piezoelectric quartz crystal biosensors," *Talanta*, vol. 46, no. 6, pp. 1223 – 1236, 1998.

[14] C. Ziegler, "Cantilever-based biosensors," *Analytical and Bioanalytical Chemistry*, vol. 379, no. 7, pp. 946–959, Aug. 2004.

[15] K.-U. Kirstein, Y. Li, M. Zimmermann, C. Vancura, T. Volden, W. H. Song, J. Lichtenberg, and A. Hierlemannn, "Cantilever-based biosensors in CMOS technology," in *Proceedings of the conference on Design, Automation and Test in Europe - Volume 2*, 2005, pp. 1340–1341.

[16] S. Joo and R. B. Brown, "Chemical sensors with integrated electronics," *Chemical Reviews*, vol. 108, no. 2, pp. 638–651, 2008.

[17] L. Clark, "Monitor and control of blood and tissue oxygen tensions," *ASAIO Journal*, vol. 2, 1956.

[18] M. Strianese, G. Zauner, A. W. Tepper, L. Bubacco, E. Breukink, T. J. Aartsma, G. W. Canters, and L. C. Tabares, "A protein-based oxygen biosensor for high-throughput monitoring of cell growth and cell viability," *Analytical Biochemistry*, vol. 385, no. 2, pp. 242 – 248, 2009.

[19] J. Sasano, D. Niwa, and T. Osaka, "Micro pH sensors and biosensors based on electrochemical field effect transistors," in *Electrochemical Nanotechnologies*, ser. Nanostructure Science and Technology, 2010, pp. 133–149.

[20] P. Pinton, A. Rimessi, A. Romagnoli, A. Prandini, and R. Rizzuto, "Biosensors for the detection of calcium and pH," in *Mitochondria, 2nd Edition*, ser. Methods in Cell Biology. Academic Press, 2007, vol. 80, pp. 297 – 325.

[21] L. C. Clark and C. Lyons, "Electrode systems for continuous monitoring in cardiovascular surgery," *Annals of the New York Academy of Sciences*, vol. 102, no. 1, pp. 29–45, 1962.

[22] J. Newman and S. Setford, "Enzymatic biosensors," *Molecular Biotechnology*, vol. 32, pp. 249–268, 2006.

[23] B. Strehlitz, N. Nikolaus, and R. Stoltenburg, "Protein detection with aptamer biosensors," *Sensors*, vol. 8, no. 7, pp. 4296–4307, 2008.

[24] K. A. Giuliano, D. R. Premkumar, and D. L. Taylor, *Optimal Characteristics of ProteinProtein Interaction Biosensors for Cellular Systems Biology Profiling*. John Wiley & Sons, Inc., 2007.

[25] J. Zhai, H. Cui, and R. Yang, "DNA based biosensors," *Biotechnology Advances*, vol. 15, no. 1, pp. 43 – 58, 1997.

[26] T. G. Drummond, M. G. Hill, and J. K. Barton, "Electrochemical DNA sensors," *Nature Biotechnology*, vol. 21, pp. 1192–1199, 2003.

[27] S. Cagnin, M. Caraballo, C. Guiducci, P. Martini, M. Ross, M. SantaAna, D. Danley, T. West, and G. Lanfranchi, "Overview of electrochemical DNA biosensors: New approaches to detect the expression of life," *Sensors*, vol. 9, no. 4, pp. 3122–3148, 2009.

[28] L. J. Edgar., "Method and apparatus for controlling electric currents," Patent US 1 745 175, January, 1930. [Online]. Available: http://www.freepatentsonline.com/1745175.html

[29] L. Edgar., "Device for controlling electric current," Patent US 1 900 018, March, 1933. [Online]. Available: http://www.freepatentsonline.com/1900018.html

[30] S. J. Updike and G. P. Hicks, "The enzyme electrode," *Nature*, vol. 214, pp. 986 – 988, 1967.

[31] G. G. Guilbault and J. G. Montalvo, "Urea-specific enzyme electrode," *Journal of the American Chemical Society*, vol. 91, no. 8, pp. 2164–2165, 1969.

[32] P. Bergveld, "Development of an ion-sensitive solid-state device for neurophysiological measurements," *Biomedical Engineering, IEEE Transactions on*, vol. BME-17, no. 1, pp. 70 –71, jan. 1970.

[33] D. W. Lubbers and N. Opitz, "The pCO2/pO2 optrode: A new pCO2, pO2 device for the measurement of pCO2 or pO2 in gases or fluids," *Z. Naturforsch. C: Biosci.*, vol. 30c, pp. 532–533, 1975.

[34] N. C. Fawcett, J. A. Evans, L.-C. Chien, and N. Flowers, "Nucleic acid hybridization detected by piezoelectric resonance," *Analytical Letters*, vol. 21, no. 7, pp. 1099–1114, 1988.

[35] J. D. Newman and A. P. Turner, "Home blood glucose biosensors: a commercial perspective," *Biosensors and Bioelectronics*, vol. 20, no. 12, pp. 2435–2453, 2005.

[36] M. Gault and C. E. Harding, "Evaluation of i-STAT portable clinical analyzer in a hemodialysis unit," *Clinical Biochemistry*, vol. 29, no. 2, pp. 117 – 124, 1996.

[37] C. R. Lowe, "Biosensors," *Trends in Biotechnology*, vol. 2, no. 3, pp. 59 – 64, 1984.

[38] T. M.-H. Lee, "Over-the-counter biosensors: Past, present, and future," *Sensors*, vol. 8, no. 9, pp. 5535–5559, 2008.

[39] A. P. F. Turner, "Biosensors-sense and sensitivity," *Science*, vol. 290, no. 5495, pp. 1315–1317, 2000.

[40] M. Abe, "Hemt technology and its impact on computers and communications," *III-Vs Review*, vol. 5, no. 5, pp. 19 – 23, 1992.

[41] C. R. Lowe, "Chemoselective biosensors," *Current Opinion in Chemical Biology*, vol. 3, no. 1, pp. 106 – 111, 1999.

[42] H. Shi, T. Xia, A. Nel, and J. Yeh, "Part II: coordinated biosensors - development of enhanced nanobiosensors for biological and medical applications." *Nanomed*, vol. 2, no. 5, pp. 599–614, 2007.

[43] A. Tiwari and S. Gong, "Electrochemical detection of a breast cancer susceptible gene using cDNA immobilized chitosan-co-polyaniline electrode," *Talanta*, vol. 77, no. 3, pp. 1217 – 1222, 2009.

[44] F. Dondero, L. Piacentini, F. Marsano, M. Rebelo, L. Vergani, P. Venier, and A. Viarengo, "Gene transcription profiling in pollutant exposed mussels (mytilus spp.) using a new low-density oligonucleotide microarray," *Gene*, vol. 376, no. 1, pp. 24 – 36, 2006.

[45] I. Palchetti and M. Mascini, "Nucleic acid biosensors for environmental pollution monitoring," *Analyst*, vol. 133, pp. 846–854, 2008.

[46] E. R. Richter, "Biosensors: Applications for dairy food industry," *Journal of Dairy Science*, vol. 76, no. 10, pp. 3114 – 3117, 1993.

[47] R. Gambari and G. Feriotto, "Surface plasmon resonance for detection of genetically modified organisms in the food supply," *Journal of AOAC International*, vol. 89, no. 3, pp. 893 –897, may 2006.

[48] J. Fritz, E. B. Cooper, S. Gaudet, P. K. Sorger, and S. R. Manalis, "Electronic detection of DNA by its intrinsic molecular charge," vol. 99, no. 22, pp. 14 142–14 146, 2002.

[49] F. Uslu, S. Ingebrandt, D. Mayer, S. Bcker-Meffert, M. Odenthal, and A. Offenhusser, "Labelfree fully electronic nucleic acid detection system based on a field-effect transistor device," *Biosensors and Bioelectronics*, vol. 19, no. 12, pp. 1723 – 1731, 2004.

[50] C. Kataoka-Hamai and Y. Miyahara, "Label-free detection of DNA by field-effect devices," *Sensors Journal, IEEE*, vol. 11, no. 12, pp. 3153 –3160, dec. 2011.

[51] L. Benini, C. Guiducci, and C. Paulus, "Electronic detection of DNA hybridization: Toward CMOS microarrays," *Design Test of Computers, IEEE*, vol. 24, no. 1, pp. 38 –48, jan.-feb. 2007.

[52] Y. Liu and R. W. Dutton, "Effects of charge screening and surface properties on signal transduction in field effect nanowire biosensors," *Journal of Applied Physics*, vol. 106, no. 1, pp. 014 701 –014 701–8, jul 2009.

[53] I. Mannelli, M. Minunni, S. Tombelli, R. Wang, M. M. Spiriti, and M. Mascini, "Direct immobilisation of DNA probes for the development of affinity biosensors," *Bioelectrochemistry*, vol. 66, no. 1-2, pp. 129 – 138, 2005.

[54] W. Jin, X. Lin, S. Lv, Y. Zhang, Q. Jin, and Y. Mu, "A DNA sensor based on surface plasmon resonance for apoptosis-associated genes detection," *Biosensors and Bioelectronics*, vol. 24, no. 5, pp. 1266 – 1269, 2009.

[55] A. J. Thiel, A. G. Frutos, C. E. Jordan, R. M. Corn, and L. M. Smith, "In situ surface plasmon resonance imaging detection of DNA hybridization to oligonucleotide arrays on gold surfaces," *Analytical Chemistry*, vol. 69, no. 24, pp. 4948–4956, 1997.

[56] J. Homola, S. S. Yee, and G. Gauglitz, "Surface plasmon resonance sensors: review," *Sensors and Actuators B: Chemical*, vol. 54, no. 1-2, pp. 3 – 15, 1999.

[57] B. Seplveda, L. G. Carrascosa, D. Regatos, M. A. Otte, D. Faria, and L. M. Lechuga, "Surface plasmon resonance biosensors for highly sensitive detection in real samples," *Proc. SPIE, Biosensing II*, vol. 7397, pp. 73 970Y–73 970Y–11, 2009.

[58] A. Sassolas, B. D. Leca-Bouvier, and L. J. Blum, "DNA biosensors and microarrays," *Chemical Reviews*, vol. 108, no. 1, pp. 109–139, 2008.

[59] V. M. Goldschmidt, "Crystal structure and chemical constitution," *Trans. Faraday Soc.*, vol. 25, pp. 253–283, 1929.

[60] O. Stuetzer, "A crystal amplifier with high input impedance," *Proceedings of the IRE*, vol. 38, no. 8, pp. 868 – 871, aug. 1950.

[61] W. Shockley, "A unipolar "field-effect" transistor," *Proceedings of the IRE*, vol. 40, no. 11, pp. 1365 –1376, nov. 1952.

[62] W. Hooper and W. Lehrer, "An epitaxial gaas field-effect transistor," *Proceedings of the IEEE*, vol. 55, no. 7, pp. 1237 – 1238, july 1967.

[63] C. Mead, "Schottky barrier gate field effect transistor," *Proceedings of the IEEE*, vol. 54, no. 2, pp. 307 – 308, feb. 1966.

[64] K. Drangeid, R. Sommerhalder, and W. Walter, "High-speed gallium-arsenide schottky-barrier field-effect transistors," *Electronics Letters*, vol. 6, no. 8, pp. 228 –229, 16 1970.

[65] W. Curtice, "Direct comparison of the electron-temperature model with the particle-mesh (monte-carlo) model for the GaAs MESFET," *Electron Devices, IEEE Transactions on*, vol. 29, no. 12, pp. 1942 – 1943, dec 1982.

[66] W. Curtice and M. Ettenberg, "A nonlinear GaAs FET model for use in the design of output circuits for power amplifiers," *Microwave Theory and Techniques, IEEE Transactions on*, vol. 33, no. 12, pp. 1383 – 1394, dec 1985.

[67] H. Statz, P. Newman, I. Smith, R. Pucel, and H. Haus, "GaAs FET device and circuit simulation in SPICE," *Electron Devices, IEEE Transactions on*, vol. 34, no. 2, pp. 160 – 169, feb 1987.

[68] C.-S. Chang and D.-Y. Day, "Analytic theory for current-voltage characteristics and field distribution of GaAs MESFET's," *Electron Devices, IEEE Transactions on*, vol. 36, no. 2, pp. 269 –280, feb 1989.

[69] P. Hower and N. Bechtel, "Current saturation and small-signal characteristics of GaAs field-effect transistors," *Electron Devices, IEEE Transactions on*, vol. 20, no. 3, pp. 213 – 220, mar 1973.

[70] M. Shur, "Small-signal nonlinear curcuit model of GaAs MESFET," *Solid-State Electronics*, vol. 22, no. 8, pp. 723 – 728, 1979.

[71] R. Dawson, "Equivalent circuit of the schottky-barrier field-effect transistor at microwave frequencies," *Microwave Theory and Techniques, IEEE Transactions on*, vol. 23, no. 6, pp. 499 – 501, jun 1975.

[72] G. Vendelin and M. Omori, "Circuit model for the GaAs m.e.s.f.e.t. valid to 12 ghz," *Electronics Letters*, vol. 11, no. 3, pp. 60 –61, 6 1975.

[73] P. H. Ladbrooke, *MMIC Design: GaAs FETs and HEMTs.* Artech House, 1989.

[74] J. M. Golio, *Microwave MESFETs and HEMTs.* Massachusetts: Artech House, 1991.

[75] E. Arnold, M. Golio, M. Miller, and B. Beckwith, "Direct extraction of GaAs MESFET intrinsic element and parasitic inductance values," in *Microwave Symposium Digest, 1990., IEEE MTT-S International*, may 1990, pp. 359 –362 vol.1.

[76] M. Shur, "Analytical model of GaAs MESFET's," *Electron Devices, IEEE Transactions on*, vol. 25, no. 6, pp. 612 – 618, jun 1978.

[77] M. Shur and L. Eastman, "Current-voltage characteristics, small-signal parameters, switching times and power-delay products of GaAs MESFET's," in *Microwave Symposium Digest, 1978 IEEE-MTT-S International*, june 1978, pp. 150 –152.

[78] T. Takada, Yokoyama, Kiyoyuki, M. Ida, and T. Sudo, "A MESFET variable-capacitance model for GaAs integrated circuit simulation," *Microwave Theory and Techniques, IEEE Transactions on*, vol. 30, no. 5, pp. 719 –724, may 1982.

[79] T.-H. Chen and M. Shur, "A capacitance model for GaAs MESFET's," *Electron Devices, IEEE Transactions on*, vol. 32, no. 5, pp. 883 – 891, may 1985.

[80] M. Ahmed, N. Ahmed, K. Chaudhary, and M. Iqbal, "Estimation of intrinsic small signal parameters of a GaAs MESFET from DC measurements," in *Multi Topic Conference, 2001. IEEE INMIC 2001. Technology for the 21st Century. Proceedings. IEEE International*, 2001, pp. 97 – 103.

[81] M. Ahmed, "An improved method to estimate intrinsic small signal parameters of a GaAs MESFET from measured DC characteristics," *Electron Devices, IEEE Transactions on*, vol. 50, no. 11, pp. 2196 – 2201, nov. 2003.

[82] J. D. Watson and F. H. C. Crick, "Molecular structure of nucleic acids: A structure for deoxyribose nucleic acid," *Nature*, vol. 171, pp. 737 – 738, 1953.

[83] A. Sayre, *Rosalind Franklin and DNA*. W. W. Norton & Co., New York, NY, 2001.

[84] D. Y. Wu, L. Ugozzoli, B. K. Pal, and R. B. Wallace, "Allele-specific enzymatic amplification of beta-globin genomic DNA for diagnosis of sickle cell anemia," *Proceedings of the National Academy of Sciences*, vol. 86, no. 8, pp. 2757–2760, 1989.

[85] R. T. Marconi and C. F. Garon, "Development of polymerase chain reaction primer sets for diagnosis of lyme disease and for species-specific identification of lyme disease isolates by 16s rRNA signature nucleotide analysis," *Journal of Clinical Microbiology*, vol. 30, no. 11, pp. 2830–2834, 1992.

[86] G. Frankel, "Detection of salmonella typhi by PCR," *Journal of Clinical Microbiology*, vol. 32, no. 5, p. 1415, 1994.

[87] H. Okamoto, Y. Sugiyama, S. Okada, K. Kurai, Y. Akahane, Y. Sugai, T. Tanaka, K. Sato, F. Tsuda, Y. Miyakawa, and M. Mayumi, "Typing hepatitis C virus by polymerase chain reaction with type-specific primers: application to clinical surveys and tracing infectious sources," *Journal of General Virology*, vol. 73, no. 3, pp. 673–679, 1992.

[88] C. Pritchard, N. Zhu, J. Zuo, L. Bull, M. A. Pericak-Vance, J. M. Vance, A. D. Roses, A. Milatovich, U. Francke, D. R. Cox, and R. M. Myers, "Recombination of 4pl6 DNA markers in an unusual family with huntington's disease," *American Journal of Human Genetics*, vol. 50, pp. 1218–1230, 1992.

[89] D. S. H. Jeremy Nathans, Darcy Thomas, "Molecular genetics of human color vision: the genes encoding blue, green, and red pigments," *Science*, vol. 232, no. 4747, pp. 193–202, 1986.

[90] F. F. Chehab, M. Doherty, S. Cai, Y. W. Kan, S. Cooper, and E. M. Rubin, "Detection of sickle cell anaemia and thalassaemias," *Nature*, vol. 329, pp. 293–294, 1987.

[91] S. H. Lee, V. S. Vigliotti, J. S. Vigliotti, W. Jones, and S. Pappu, "Increased sensitivity and specificity of borrelia burgdorferi 16s ribosomal DNA detection," *American Journal of Clinical Pathology*, vol. 133, no. 4, pp. 569–576, 2010.

[92] T. H. Helbich, G. Heinz-Peer, I. Eichler, P. Wunderbaldinger, M. Götz, C. Wojnarowski, R. C. Brasch, and C. J. Herold, "Cystic fibrosis: CT assessment of lung involvement in children and adults," *Radiology*, vol. 213, no. 2, pp. 537–544, 1999.

[93] M.-P. Audrezet, A. Dabricot, C. L. Marechal, and C. Ferec, "Validation of high-resolution dna melting analysis for mutation scanning of the cystic fibrosis transmembrane conductance regulator (cftr) gene," *The Journal of Molecular Diagnostics*, vol. 10, no. 5, pp. 424 – 434, 2008.

[94] S. Rust, M. Rosier, H. Funke, J. Real, Z. Amoura, J.-C. Piette, J.-F. Deleuze, H. B. Brewer, N. Duverger, P. Denfle, and G. Assmann, "Tangier disease is caused by mutations in the gene encoding ATP-binding cassette transporter 1," *Nature Genetics*, vol. 22, pp. 352 – 355, 1999.

[95] M. Hatta and H. L. Smits, "Detection of salmonella typhi by nested polymerase chain reaction in blood, urine, and stool samples," *The American Journal of Tropical Medicine and Hygiene*, vol. 76, no. 1, pp. 139–143, 2007.

[96] G. Pozzato, C. Mazzaro, M. Crovatto, M. Modolo, S. Ceselli, G. Mazzi, S. Sulfaro, F. Franzin, P. Tulissi, and M. Moretti, "Low-grade malignant lymphoma, hepatitis C virus infection, and mixed cryoglobulinemia," *Blood*, vol. 84, no. 9, pp. 3047–3053, 1994.

[97] T. Boland and B. D. Ratner, "Two-dimensional assembly of purines and pyrimidines on au(111)," *Langmuir*, vol. 10, no. 10, pp. 3845–3852, 1994.

[98] G. Ashkenasy, D. Cahen, R. Cohen, A. Shanzer, and A. Vilan, "Molecular engineering of semiconductor surfaces and devices," *Accounts of Chemical Research*, vol. 35, no. 2, pp. 121–128, 2002.

[99] F. Seker, K. Meeker, T. F. Kuech, and A. B. Ellis, "Surface chemistry of prototypical bulk II-VI and III-V semiconductors and implications for chemical sensing," *Chemical Reviews*, vol. 100, no. 7, pp. 2505–2536, 2000.

[100] R. Cohen, L. Kronik, A. Shanzer, D. Cahen, A. Liu, Y. Rosenwaks, J. K. Lorenz, and A. B. Ellis, "Molecular control over semiconductor surface electronic properties: Dicarboxylic acids on CdTe, CdSe, GaAs, and InP," *Journal of the American Chemical Society*, vol. 121, no. 45, pp. 10 545–10 553, 1999.

[101] A. Mamishev, K. Sundara-Rajan, F. Yang, Y. Du, and M. Zahn, "Interdigital sensors and transducers," *Proceedings of the IEEE*, vol. 92, no. 5, pp. 808 – 845, may 2004.

[102] E. Parton, C. Bartic, and A. Campitelli, "Micro-system platforms/new materials for biosensor applications," *Solid state technology*, vol. 47, pp. S1–S2, 2004.

[103] C. W. Sheen, J. X. Shi, J. Martensson, A. N. Parikh, and D. L. Allara, "A new class of organized self-assembled monolayers - alkane thiols on GaAs(100)," *Journal of the American Chemical Society*, vol. 114, no. 4, pp. 1514–1515, 1992.

[104] A. Ulman, "Formation and structure of self-assembled monolayers," *Chemical Reviews*, vol. 96, no. 4, pp. 1533–1554, 1996.

[105] K. Adlkofer, M. Tanaka, H. Hillebrandt, G. Wiegand, E. Sackmann, T. Bolom, R. Deutschmann, and G. Abstreiter, "Electrochemical passivation of gallium arsenide surface with organic self-assembled monolayers in aqueous electrolytes," *Applied Physics Letters*, vol. 76, no. 22, pp. 3313–3315, 2000.

[106] A. Shaporenko, K. Adlkofer, L. S. O. Johansson, M. Tanaka, and M. Zharnikov, "Functionalization of GaAs surfaces with aromatic self-assembled monolayers: A synchrotron-based spectroscopic study," *Langmuir*, vol. 19, pp. 4992–4998, 2003.

[107] C. L. McGuiness, "Molecular assembly at bare semiconductor surfaces," Ph.D. dissertation, The Pennsylvania State University, Pennsylvania, PA, 2006.

[108] J. Y., Z. XY., and H. JW., "Formation of alkanethiol and alkanedithiol monolayers on GaAs(001)," *Langmuir*, vol. 22, no. 8, pp. 3627–3632, 2006.

[109] X. Ding, K. Moumanis, J. J. Dubowski, L. Tay, and N. L. Rowell, "Fourier-transform infrared and photoluminescence spectroscopies of self-assembled monolayers of long-chain thiols on (001) GaAs," *Journal of Applied Physics*, vol. 99, no. 5, p. 054701, 2006.

[110] H. P. Wampler, D. Y. Zemlyanov, K. Lee, D. B. Janes, and A. Ivanisevic, "Mixed adlayer of alkanethiol and peptide on GaAs(100): Quantitative characterization by x-ray photoelectron spectroscopy," *Langmuir*, vol. 24, no. 7, pp. 3164–3170, 2008.

[111] R. Artzi, S. S. Daube, H. Cohen, and R. Naaman, "Adsorption of organic phosphate as a means to bind biological molecules to GaAs surfaces," *Langmuir*, vol. 19, no. 18, pp. 7392–7398, 2003.

[112] O. Voznyy and J. J. Dubowski, "Adsorption and self-assembly of alkanethiols on GaAs (001) surface," in *Lasers and Electro-Optics Society, 2006. LEOS 2006. 19th Annual Meeting of the IEEE*, Oct. 2006, pp. 308 –309.

[113] O. A. Voznyy and J. J. Dubowski, "Structure of thiol self-assembled monolayers commensurate with the GaAs (001) surface," *Langmuir*, vol. 24, no. 23, pp. 13 299–13 305, 2008.

[114] Q. Liu, L. Wang, A. G. Frutos, A. E. Condon, R. M. Corn, and L. M. Smith, "DNA computing on surfaces," *Nature*, vol. 403, pp. 175–179, 1999.

[115] K. Goede, P. Busch, and M. Grundmann, "Binding specificity of a peptide on semiconductor surfaces," *Nano Letters*, vol. 4, no. 11, pp. 2115–2120, 2004.

[116] K. Goede, M. Grundmann, K. Holland-Nell, and A. G. Beck-Sickinger, "Cluster properties of peptides on (100) semiconductor surfaces," *Langmuir*, vol. 22, no. 19, pp. 8104–8108, 2006.

[117] A. Steel, R. Levicky, T. Herne, and M. Tarlov, "Immobilization of nucleic acids at solid surfaces: Effect of oligonucleotide length on layer assembly," *Biophysical Journal*, vol. 79, no. 2, pp. 975 – 981, 2000.

[118] L. Mohaddes-Ardabili, L. J. Martínez-Miranda, J. Silverman, A. Christou, L. G. Salamanca-Riba, M. Al-Sheikhly, W. E. Bentley, and F. Ohuchi, "Attachment of DNA probes on gallium arsenide surface," *Applied Physics Letters*, vol. 83, no. 1, pp. 192–194, 2003.

[119] L. Mohaddes-Ardabili, L. J. Martínez-Miranda, L. G. Salamanca-Riba, A. Christou, J. Silverman, W. E. Bentley, and M. Al-Sheikhly, "Preferred orientation of DNA oligonucleotide probes on the (2 x 4) reconstructed surface of (001) GaAs," *Journal of Applied Physics*, vol. 95, no. 11, pp. 6021–6024, 2004.

[120] J. Yang, "The attachment and characterization of DNA probes on gaas-based semiconductor surfaces," Ph.D. dissertation, University of Maryland, College Park, Md., 2007.

[121] Z.-M. Wang, Y.-C. Cheung, P.-H. Leung, and J.-Y. Wu, "Ultrasonic treatment for improved solution properties of a high-molecular weight exopolysaccharide produced by a medicinal fungus," *Bioresource Technology*, vol. 101, no. 14, pp. 5517 – 5522, 2010.

[122] E. Souteyrand, J. P. Cloarec, J. R. Martin, C. Wilson, I. Lawrence, S. Mikkelsen, and M. F. Lawrence, "Direct detection of the hybridization of synthetic homo-oligomer DNA sequences by field effect," *The Journal of Physical Chemistry B*, vol. 101, no. 15, pp. 2980–2985, 1997.

[123] S. Q. Lud, M. G. Nikolaides, I. Haase, M. Fischer, and A. R. Bausch, "Field effect of screened charges: Electrical detection of peptides and proteins by a thin-film resistor," *ChemPhysChem*, vol. 7, no. 2, pp. 379–384, 2006.

[124] S. Birner, C. Uhl, M. Bayer, and P. Vogl, "Theoretical model for the detection of charged proteins with a silicon-on-insulator sensor," *Journal of Physics: Conference Series*, vol. 107, no. 1, p. 012002, 2008.

[125] C. Berggren, P. Stalhandske, J. Brundell, and G. Johansson, "A feasibility study of a capacitive biosensor for direct detection of DNA hybridization," *Electroanalysis*, vol. 11, no. 3, pp. 156–160, 1999.

[126] C. Berggren, B. Bjarnason, and G. Johansson, "Capacitive biosensors," *Electroanalysis*, vol. 13, no. 3, pp. 173–180, 2001.

[127] C. Guiducci, C. Stagni, G. Zuccheri, A. Bogliolo, L. Benini, B. Samorì, and B. Riccò, "DNA detection by integrable electronics." *Biosens Bioelectron*, vol. 19, no. 8, pp. 781–7, 2004.

[128] H. Berney, J. West, E. Haefele, J. Alderman, W. Lane, and J. Collins, "A DNA diagnostic biosensor: development, characterisation and performance," *Sensors and Actuators B: Chemical*, vol. 68, no. 1-3, pp. 100 – 108, 2000.

[129] D. Landheer, G. Aers, W. R. McKinnon, M. J. Deen, and J. C. Ranuarez, "Model for the field effect from layers of biological macromolecules on the gates of metal-oxide-semiconductor transistors," *Journal of Applied Physics*, vol. 98, no. 4, p. 044701, 2005.

[130] C. Heitzinger, R. Kennell, G. Klimeck, N. Mauser, M. McLennan, and C. Ringhofer, "Modeling and simulation of field-effect biosensors (BioFETs) and their deployment on the nanoHUB," *Journal of Physics: Conference Series*, vol. 107, no. 1, p. 012004, 2008.

[131] C. Ringhofer and C. Heitzinger, "Multi - scale modeling and simulation of field-effect biosensors," *ECS Transactions*, vol. 14, no. 1, pp. 11–19, 2008.

[132] J. N. Israelachvili, *Intermolecular and Surface Forces*, 2nd ed. Academic Press, London, 1992.

[133] S. O. Kasap, *Principles of Electronic Materials and Devices*, 3rd ed. McGraw-Hill, 2005.

[134] P. Y. Yu and M. Cardona, *Fundamentals of Semiconductors*. Springer, 1996.

[135] J. C. Phillips, "Energy-band interpolation scheme based on a pseudopotential," *Phys. Rev.*, vol. 112, pp. 685–695, Nov 1958.

[136] J. C. Phillips and L. Kleinman, "New method for calculating wave functions in crystals and molecules," *Phys. Rev.*, vol. 116, pp. 287–294, Oct 1959.

[137] M. L. Cohen and T. K. Bergstresser, "Band structures and pseudopotential form factors for fourteen semiconductors of the diamond and zinc-blende structures," *Phys. Rev.*, vol. 141, pp. 789–796, Jan 1966.

[138] J. R. Chelikowsky and M. L. Cohen, "Nonlocal pseudopotential calculations for the electronic structure of eleven diamond and zinc-blende semiconductors," *Phys. Rev. B*, vol. 14, pp. 556–582, Jul 1976.

[139] E. O. Kane, "Band structure of indium antimonide," *Journal of Physics and Chemistry of Solids*, vol. 1, no. 4, pp. 249 – 261, 1957.

[140] Y. P. Varshni, "Temperature dependence of the energy gap in semiconductors," *Physica*, vol. 34, pp. 149–154, 1967.

[141] I. Vurgaftman, J. R. Meyer, and L. R. Ram-Mohan, "Band parameters for III-V compound semiconductors and their alloys," *Journal of Applied Physics*, vol. 89, no. 11, pp. 5815–5875, 2001.

[142] S. M. Sze, *Physics of Semiconductor Devices.* New York: John Wiley & Sons, 2nd ed., 1981.

[143] E. O. Kane, "The $k \cdot p$ method. *Semiconductors and Semimetals*," *Academic, New York*, vol. 1, pp. 75 – 100, 1966.

[144] J. M. Luttinger and W. Kohn, "Motion of electrons and holes in perturbed periodic fields," *Phys. Rev.*, vol. 97, pp. 869–883, Feb 1955.

[145] B. K. Aggarwal and M. Eisner, *Statistical Mechanics.* John Wiley & Sons Inc, 1988.

[146] K. W. Boer, *Survey of Semiconductor Physics.* Van Nostrand Reinhold, New York, 1992, vol. 2.

[147] C. M. Snowden, "Semiconductor device modelling," *Reports on Progress in Physics*, vol. 48, no. 2, p. 223, 1985.

[148] D. Vasileska, D. Mamaluy, H. Khan, K. Raleva, and S. Goodnick, "Semiconductor device modeling," *Journal of Computational and Theoretical Nanoscience*, vol. 5, no. 6, pp. 999–1030, 2008.

[149] T. Zibold, "Semiconductor based quantum information devices: Theory and simulations," Ph.D. dissertation, Verein zur Frderung des Walter Schottky Instituts der Technischen Universitt Mnchen e.V., Mnchen, 2007.

[150] D. Caughey and R. Thomas, "Carrier mobilities in silicon empirically related to doping and field," *Proceedings of the IEEE*, vol. 55, no. 12, pp. 2192 – 2193, dec. 1967.

[151] C. Maziar and M. Lundstrom, "Caughey-thomas parameters for electron mobility calculations in GaAs," *Electronics Letters*, vol. 22, no. 11, pp. 565 –566, 22 1986.

[152] W. Walukiewicz, L. Lagowski, L. Jastrzebski, M. Lichtensteiger, and H. C. Gatos, "Electron mobility and free-carrier absorption in GaAs: Determination of the compensation ratio," *Journal of Applied Physics*, vol. 50, no. 2, pp. 899 –908, feb 1979.

[153] S. Selberherr, *Analysis and Simulation of Semiconductor Devices.* Springer-Verlag, 1984.

[154] W. Engl and H. Dicks, *Models of Physical Parameters. An Introduction to the numerical analysis of semiconductor devices and integrated circuits.* Dublin: Book Press, 1981.

[155] S. Mohammad, A. Bemis, R. Carter, and R. Renbeck, "Temperature, electric field, and doping dependent mobilities of electrons and holes in semiconductors," *Solid-State Electronics*, vol. 36, no. 12, pp. 1677 – 1683, 1993.

[156] J. Pozela and A. Peklaitis, "Temperature, electric field, and doping dependent mobilities of electrons and holes in semiconductors," *Solid-State Electronics*, vol. 23, 1980.

[157] W. G. Spitzer and C. A. Mead, "Barrier height studies on metal-semiconductor systems," *Journal of Applied Physics*, vol. 34, no. 10, pp. 3061–3069, 1963.

[158] J. Bardeen, "Surface states and rectification at a metal semi-conductor contact," *Phys. Rev.*, vol. 71, pp. 717–727, May 1947.

[159] Y. P. Varshni, "Band-to-band radiative recombination in groups IV, VI, and III-V semiconductors (i)," *physica status solidi (b)*, vol. 19, no. 2, pp. 459–514, 1967.

[160] W. Shockley and W. T. Read, "Statistics of the recombinations of holes and electrons," *Phys. Rev.*, vol. 87, pp. 835–842, Sep 1952.

[161] S. Birner, T. Zibold, T. Andlauer, T. Kubis, M. Sabathil, A. Trellakis, and P. Vogl, "nextnano: General purpose 3-d simulations," *Electron Devices, IEEE Transactions on*, vol. 54, no. 9, pp. 2137 –2142, sept. 2007.

[162] A. Trellakis, T. Zibold, T. Andlauer, S. Birner, R. Smith, R. Morschl, and P. Vogl, "The 3D nanometer device project nextnano: Concepts, methods, results," *Journal of Computational Electronics*, vol. 5, no. 4, pp. 285–289, 2006.

[163] G. Bastard, "Superlattice band structure in the envelope-function approximation," *Phys. Rev. B*, vol. 24, pp. 5693–5697, Nov 1981.

[164] G. A. Bastard, "Theoretical investigations of superlattice band structure in the envelope-function approximation," *Phys. Rev. B*, vol. 25, pp. 7584–7597, Jun 1982.

[165] L. N. Trefethen and D. B. III, *Numerical Linear Algebra.* SIAM: Society for Industrial and Applied Mathematics, 1997.

[166] "ARPACK libraries and related publications," http://www.caam.rice.edu/software/ARPACK/.

[167] A. Franz, G. Franz, S. Selberherr, C. Ringhofer, and P. Markowich, "Finite boxes-a generalization of the finite-difference method suitable for semiconductor device simulation," *Electron Devices, IEEE Transactions on*, vol. 30, no. 9, pp. 1070 – 1082, sep 1983.

[168] T. Andlauer, "Optoelectronic and spin-related properties of semiconductor nanostructures in magnetic fields," Ph.D. dissertation, Verein zur Frderung des Walter Schottky Instituts der Technischen Universitt Mnchen e.V., Mnchen, 2009.

[169] C. F. Gerald and P. O. Wheatley, *Applied Numerical Analysis*, 4th ed. Addison Wesley, 1989.

[170] A. Trellakis, A. T. Galick, A. Pacelli, and U. Ravaioli, "Iteration scheme for the solution of the two-dimensional schr[o-umlaut]dinger-poisson equations in quantum structures," *Journal of Applied Physics*, vol. 81, no. 12, pp. 7880–7884, 1997.

[171] J. Golio, M. Miller, G. Maracas, and D. Johnson, "Frequency-dependent electrical characteristics of gaas mesfets," *Electron Devices, IEEE Transactions on*, vol. 37, no. 5, pp. 1217 –1227, may 1990.

[172] K.-A. Son, B. Yang, N. Prokopuk, J. S. Moon, A. Liao, M. Gallegos, J. Yang, and M. A. Khan, "GaN-based micro chemical sensor nodes for early warning chemical agents," pp. 655 616–655 616–6, 2007.

[173] I. Cimalla, F. Will, K. Tonisch, and M. Niebelsch "AlGaN/GaN biosensor-effect of device processing steps on the surface properties and biocompatibility," *Sensors and Actuators B: Chemical*, vol. 123, no. 2, pp. 740 – 748, 2007.

[174] G. Steinhoff, O. Purrucker, M. Tanaka, M. Stutzmann, and M. Eickhoff, "Al$_x$Ga$_{1-x}$N-A new material system for biosensors," *Advanced Functional Materials*, vol. 13, no. 11, pp. 841–846, 2003.

[175] B. Baur, G. Steinhoff, J. Hernando, O. Purrucker, M. Tanaka, B. Nickel, M. Stutzmann, and M. Eickhoff, "Chemical functionalization of GaN and AlN surfaces," *Applied Physics Letters*, vol. 87, no. 26, pp. 263 901 –263 901–3, dec 2005.

[176] X. Wen, M. Schuette, S. Gupta, T. Nicholson, S. Lee, and W. Lu, "Improved sensitivity of AlGaN/GaN field effect transistor biosensors by optimized surface functionalization," *Sensors Journal, IEEE*, vol. 11, no. 8, pp. 1726 –1735, aug. 2011.

[177] N. Yoshizawa, T. Sato, and A. Mizohata, "Liquid-phase chemical sensors using InP-based open-gate FETs," in *Sensors, 2008 IEEE*, oct. 2008, pp. 1305 –1308.

[178] K. Wierzbowska, L. Bideux, B. Adamowicz, and A. Pauly, "A novel III-V semiconductor material for NO_2 detection and monitoring," *Sensors and Actuators A: Physical*, vol. 142, no. 1, pp. 237 – 241, 2008.

Appendix A Some Important Physical Constants

Quantity	Symbol	Value
Avogadro's number	N_{AV}	6.0221367×10^{23} 1/mol
Bohr energy	E_B	13.606 eV
Bohr magneton	μ_B	5.78832×10^{-5} eV/T
Bohr radius	a_B	0.52917 Å
Boltzmann constant	k_B	1.38066×10^{-23} J/K
Electronic charge	q	1.60218×10^{-19} C
Electron volt	eV	1.60218×10^{-19} J
Mass of electron at rest	m_e	$9.1093897 \times 10^{-31}$ kg
Mass of proton at rest	m_p	$1.6726231 \times 10^{-27}$ kg
Permeability in vacuum	μ_0	1.2623×10^{-8} H/cm($4\pi \times 10^{-9}$)
Permittivity in vacuum	ϵ_0	8.85418×10^{-12} F m^{-1}
Planck's constant	h	6.62607×10^{-34} J^{-s}
Reduced Planck's constant	$\hbar = h/2\pi$	1.05457×10^{-34} J^{-s}
Speed of light in vacuum	c	2.9979×10^{8} m sec^{-1}
Thermal voltage at $300K$	$k_B T/q$	0.02586 V

Appendix B Properties of Gallium Arsenide (GaAs)

Crystal structure	zinc blende
Breakdown field (V/cm)	$\sim 4.0 \times 10^5$
Density	(g/cm^3) 5.3176 (at 298 K)
Dielectric constant (κ_s)	12.93 (at 300 K)
(κ_0)	10.89 (at 300 K)
Diffusion constant (cm^2/s)	207 (electrons, at 300 K)
	10 (holes, at 300 K)
Effective density of states in the conduction band (cm^{-3})	4.7×10^{17} (at 300 K)
Effective density of states in the valence band (cm^{-3})	7.0×10^{18} (at 300 K)
Effective electron mass (in units of m_e)	0.067 (at 0 K)
	0.063 (at 300 K)
Effective hole mass (in units of me) heavy hole	0.51 (at < 100 K)
	0.50 (at 300 K)
light hole	0.084 (at < 100 K)
	0.076 (at 300 K)
density of states	0.53
Electron affinity (V)	4.07
Energy gap (eV)	1.424 (at 300 K)
	1.507 (at 77 K)
	1.519 (at 0 K)
Index of refraction	3.3
Intrinsic carrier concentration (cm^{-3})	2.1×10^6 (at 300 K)
Intrinsic Debye length (μm)	2250 (at 300 K)
Intrinsic resistivity (Ω-cm)	10^8 (at 300 K)
Lattice constant ($\mathring{A}$)	5.6533 (at 300 K)
Melting point (°C)	1240
Mobility (cm^2/V-s)	8500 (electrons, at 300 K)
	400 (holes, at 300 K)
Optical phonon energy (eV)	0.035
Specific heat (J/g$-°C$)	0.35
Thermal conductivity (W/cm$-°C$)	0.46
Thermal diffusivity (cm^2/s)	0.44
Thermal expansion, linear (°C^{-1})	6.86×10^{-6} (at 300 K)

Curriculum Vitae

John K. Kimani

Place of Birth: Kiambu, Kenya

Education
B.S., Miami University-Oxford, OH, May 2007
Major: Computer Engineering

M.S., University of Wisconsin-Milwaukee, May 2009
Major: Electrical Engineering
Thesis Title: DC and Microwave characterization of GaAs HEMT on-wafer devices

Ph.D., University of Wisconsin-Milwaukee, December 2012
Major: Electrical Engineering
Dissertation Title: DC and Microwave analysis of GaAs field-effect transistor-based nucleic acid biosensors

Experience
Contract Engineer
ABL Technologies, Milwaukee, WI. July 2012 - present
Designed systems for monitoring and controlling cardiac ablation procedures

Graduate Research and Project Assistant
University of Wisconsin-Milwaukee, Milwaukee, WI. August 2007 - December 2012
Developed GaAs field effect transistor models for biosensing applications
Performed simulation of semiconductor device physical models with TCAD
Fabricated on-wafer GaAs devices and performed DC analysis and high frequency (S-parameter) calibration and measurements
Characterized and modeled GaAs MESFET and HEMT transistor devices

Teaching Assistant
UW-Milwaukee Electrical Engineering Department, March 2008 - December 2012
Served as a lab instructor for Electronics I, Electronics II, Microprocessors, and Senior Capstone Design classes for over 8 semesters
Taught Electronics II as the main instructor, and led discussion sessions for Digital Logic class

Publications and Presentations

D. P. Klemer, J. K. Kimani, B. C. Pietz, "Biomolecular Immobilization onto Microwave GaAs Field-Effect Transistor Gate Metal," *Biomedical Sciences Instrumentation*, April 2009.

J. K. Kimani, F. Li, D. P. Klemer, S. Mao, J. Chen, and D. A. Steeber, "Microwave Modeling of Interdigitated Polymer Semiconductor Biosensors," *32nd Annual Great Lakes Biomedical Conference, Racine, WI,* April 2008.

F. Li, D. P. Klemer, J. K. Kimani, S. Mao, J. Chen, D. A. Steeber, "Fabrication and characterization of microwave immunosensors based on organic semiconductors with nanogold-labeled antibody," *IEEE Engineering in Medicine and Biology Society (EMBC),* August, 2008.

S. Mao, F. Li, J. K. Kimani, J. H. Chen, and D. P. Klemer, "A hybrid Nanostructure System Defined by Electrospray Deposition for Microwave Application," *Presented at the Argonne National Laboratory 2008 Users Meetings, Argonne, IL,* May 4-8, 2008.

A. D. Mueller, S. Golembiewski, D. P. Klemer, J. K. Kimani, J. A. Fendt, C. S. Mosey, K. M. Oaks, B. R. Forman, DVM and the UWM Fall 2007 EE330 Electronics I Class, "A Self-Contained Micropower Pulse Monitor for Rodent Anesthesia: Design and Implementation," *32nd Annual Great Lakes Biomedical Conference, Racine, WI,* April 2008.

D. Garmatyuk, J. Schuerger, J. Morton, K. Binns, M. Durbin, J. Kimani, "Feasibility Study of a Multi-Carrier Dual-Use Imaging Radar and Communication System," *IEEE European Microwave Conference (EuMC),* October 8 - 12, 2007.

J. Kimani, J. Woo, D. Herbert, Y. Lu, "CO_2 Sensing for Indoor Air Quality Detection Using Sensor Networks," *2006 National Conference for the Society for Advancement of Chicanos and Native Americans in Science (SACNAS), Tampa, FL.* October 26-29, 2006.

Activities and Awards

Member, Institute of Electrical and Electronics Engineers - IEEE
Member, IEEE Microwave Theory and Techniques Society
Member, IEEE Engineering in Medicine and Biology Society
Member, National Society of Black Engineers - NSBE
CPR/AED Certification by the American Heart Association - Expires 2014
Volunteered with the American Red Cross Society's First Aid team (2009 to 2010)
Recipient, Chancellor's Graduate Student Award - UW-Milwaukee 2007/2008 to 2011/2012